X91-36054

X91-36054 *

NASA Contractor Report 4355

Large Deformation Behavior of Long Shallow Cylindrical Composite Panels

Douglas M. Carper, Michael W. Hyer,
and Eric R. Johnson

COOPERATIVE AGREEMENT NCC1-15
APRIL 1991

NASA

NASA Contractor Report 4355

Large Deformation Behavior of Long Shallow Cylindrical Composite Panels

Douglas M. Carper, Michael W. Hyer,
and Eric R. Johnson
Virginia Polytechnic Institute and State University
Blacksburg, Virginia

Prepared for
Langley Research Center
under Cooperative Agreement NCC1-15

National Aeronautics and
Space Administration
Office of Management
Scientific and Technical
Information Division

1991

Page intentionally left blank

ACKNOWLEDGEMENTS

The research effort which led to the results in this report was financially supported by the NASA-Langley Research Center's Impact Dynamics Branch through the NASA-Virginia Tech Composites Program, Cooperative Agreement NCC1-15. This support is gratefully acknowledged. The technical assistance of Robert G. Tompson, Huey D. Carden, and Richard L. Boitnott of the Impact Dynamics Branch is appreciated. Also the machine shop support of Robert L. Davis at Virginia Tech is appreciated. This report is the thesis prepared by the first author to obtain a Master of Science in Engineering Mechanics at Virginia Tech.

Table of Contents

	Page
Acknowledgements	iii
List of Tables	vi
List of Figures	vii
List of Appendices	xi
List of Symbols	xii
Chapter	
1 Introduction	1
Previous Work	3
Objective of Present Work	7
2 Derivation of Governing Equations	9
Nomenclature	9
Kinematics of Deformation	11
Total Potential Energy	21
3 Solution to Governing Equation and Numerical Results	32
Midspan Loading: $q \neq 0$ and $q \neq \frac{n\pi}{2}$, $n = 1, 3, 5,$	33
Midspan Loading: $q = 0$	35
Midspan Loading: $q = \frac{n\pi}{2}$, $n = 1, 3, 5,$	36
Eccentric Loading: $q \neq 0$ and $q \neq \frac{n\pi}{2}$, $n = 1, 2, 3,$	37
Eccentric Loading: $q = 0$	38
Eccentric Loading: $q = \frac{n\pi}{2}$, $n = 1, 2, 3,$	38
Typical Numerical Results-Midspan Loading	40
Typical Numerical Results-Eccentric Loading	50
4 Experimental Set-up and Procedure	66
Curved Panel Specimens	66
Test Fixture	68
Instrumentation	84
Initial Measurements	89
Test Procedure	89

5 Correlation of Experimental and Theoretical Results..... 92

6 Conclusions and Recommendations..... 124

References..... 127

Appendices

A Coefficients of Load-Thrust Relationships..... 128

Midspan Loading: $q \neq 0$ and $q \neq \frac{n\pi}{2}$, $n = 1, 3, 5,$..... 128

Midspan Loading: $q = \frac{n\pi}{2}$, $n = 1, 3, 5,$ 129

Eccentric Loading: $q \neq 0$ and $q \neq \frac{n\pi}{2}$, $n = 1, 2, 3,$ 130

Eccentric Loading: $q = \frac{n\pi}{2}$, $n = 1, 2, 3,$ 131

B Effect of Orthotropy on Panel Behavior..... 133

C Determination of Extensional Stiffnesses and Bending Stiffnesses..... 138

Extensional Stiffness..... 138

Bending Stiffness..... 139

D Effect of Geometric Imperfections on Panel Behavior..... 143

E Effect of Initial Stiffness on Panel Behavior..... 151

List of Tables

Table		Page
1	Intended Test Specimen Geometry	67
2	Measured Test Specimen Geometry	90
3	Test Cases Presented	94
B1	Panel Geometries and Material Properties	136
C1	Measured Panel Stiffnesses	140
E1	Effect of Panel Parameters on Initial Stiffness	154

List of Figures

Figure		Page
1.	Model of Fuselage Skin	2
2.	Symmetric and Asymmetric Response	4
3.	Cylinder Geometry and Nomenclature	10
4.	Kinematics of Middle Surface Deformations	12
5.	Load-Thrust and Load-Displacement Relations, $\lambda = 1.75$, $\overline{\Gamma} = 0.0$	41
6.	Equilibrium Configurations, $\lambda = 1.75$, $\overline{\Gamma} = 0.0$	42
7.	Surface Strains vs. Applied Load, $\lambda = 1.75$, $\overline{\Gamma} = 0.0$	43
8.	Load-Thrust and Load-Displacement Relations, $\lambda = 2.5$, $\overline{\Gamma} = 0.0$	45
9.	Equilibrium Configurations, $\lambda = 2.5$, $\overline{\Gamma} = 0.0$	46
10.	Surface Strains vs. Applied Load, $\lambda = 2.5$, $\overline{\Gamma} = 0.0$	47
11.	Load-Thrust and Load-Displacement Relations, $\lambda = 4.0$, $\overline{\Gamma} = 0.0$	49
12.	Equilibrium Configurations, $\lambda = 4.0$, $\overline{\Gamma} = 0.0$	51
13.	Surface Strains vs. Applied Load, $\lambda = 4.0$, $\overline{\Gamma} = 0.0$	52
14.	Load-Thrust and Load-Displacement Relations, $\lambda = 1.75$, $\overline{\Gamma} = 0.1$	53
15.	Equilibrium Configurations, $\lambda = 1.75$, $\overline{\Gamma} = 0.1$	54
16.	Surface Strains vs. Applied Load, $\lambda = 1.75$, $\overline{\Gamma} = 0.1$	55
17.	Load-Thrust and Load-Displacement Relations, $\lambda = 2.5$, $\overline{\Gamma} = 0.1$	57
18.	Equilibrium Configurations, $\lambda = 2.5$, $\overline{\Gamma} = 0.1$	58
19.	Surface Strains vs. Applied Load, $\lambda = 2.5$, $\overline{\Gamma} = 0.1$	59
20.	Load-Thrust and Load-Displacement Relations, $\lambda = 4.0$, $\overline{\Gamma} = 0.1$	60

21. Equilibrium Configurations, $\lambda = 4.0$, $\overline{\Gamma} = 0.1$..... 62

22. Surface Strains vs. Applied Load, $\lambda = 4.0$, $\overline{\Gamma} = 0.1$..... 63

23. Sensitivity of Buckling Load to Load Eccentricity..... 64

24. Photograph of Machined Specimens..... 69

25. Schematic of Test Fixture..... 70

26. Photograph of Test Fixture..... 71

27. Schematic of End Dowels..... 73

28. Schematic of Support Blocks..... 75

29. Photograph of Support Blocks..... 76

30. Schematic of Base Plate..... 77

31. Schematic of Loading Head and Pivot..... 80

32. Illustration of Pivoting Action..... 81

33. Photograph of Loading Head and Pivot..... 82

34. Schematic of Tongue and Connector..... 83

35. Photograph of Test Fixture..... 85

36. Photograph of Experimental Set-up, Side View..... 87

37. Photograph of Experimental Set-up, End View..... 88

38. Comparison of Theory and Experiment: Load-Thrust and Load-Displacement Relations; $R = 56.34$, $S = 12.0$, $\overline{\Gamma} = 0.0$, $[(90/0)_4]_s$..... 95

39. Comparison of Theory and Experiment: Equilibrium Configurations; $R = 56.34$, $S = 12.0$, $\overline{\Gamma} = 0.0$, $[(90/0)_4]_s$..... 96

40. Comparison of Theory and Experiment: Surface Strains vs. Applied Load; $R = 56.34$, $S = 12.0$, $\overline{\Gamma} = 0.0$, $[(90/0)_4]_s$..... 97

41. Comparison of Theory and Experiment: Load-Thrust and Load-Displacement Relations; $R = 52.04$, $S = 12.0$, $\overline{\Gamma} = 0.15$, $[(90/0)_4]_s$..... 100

42. Comparison of Theory and Experiment: Equilibrium Configurations; R = 52.04, S = 12.0, $\overline{\Gamma}$ = 0.15, $[(90/0)_4]_s$.. 101

43. Comparison of Theory and Experiment: Surface Strains vs. Applied Load; R = 52.04, S = 12.0, $\overline{\Gamma}$ = 0.15, $[(90/0)_4]_s$.... 102

44. Comparison of Theory and Experiment: Load-Thrust and Load-Displacement Relations; R = 54.72, S = 12.0, $\overline{\Gamma}$ = 0.3, $[(90/0)_4]_s$..... 104

45. Comparison of Theory and Experiment: Equilibrium Configurations; R = 54.72, S = 12.0, $\overline{\Gamma}$ = 0.3, $[(90/0)_4]_s$... 105

46. Comparison of Theory and Experiment: Surface Strains vs. Applied Load; R = 54.72, S = 12.0, $\overline{\Gamma}$ = 0.3, $[(90/0)_4]_s$..... 106

47. Comparison of Theory and Experiment: Load-Thrust and Load-Displacement Relations; R = 55.42, S = 12.0, $\overline{\Gamma}$ = 0.0, $[(90/0)_3]_s$..... 108

48. Comparison of Theory and Experiment: Equilibrium Configurations; R = 55.42, S = 12.0, $\overline{\Gamma}$ = 0.0, $[(90/0)_3]_s$... 109

49. Comparison of Theory and Experiment: Surface Strains vs. Applied Load; R = 55.42, S = 12.0, $\overline{\Gamma}$ = 0.0, $[(90/0)_3]_s$..... 110

50. Comparison of Theory and Experiment: Load-Thrust and Load-Displacement Relations; R = 55.34, S = 12.0, $\overline{\Gamma}$ = 0.15, $[(90/0)_3]_s$..... 111

51. Comparison of Theory and Experiment: Equilibrium Configurations; R = 55.34, S = 12.0, $\overline{\Gamma}$ = 0.15, $[(90/0)_3]_s$.. 112

52. Comparison of Theory and Experiment: Surface Strains vs. Applied Load; R = 55.34, S = 12.0, $\overline{\Gamma}$ = 0.15, $[(90/0)_3]_s$.... 113

53. Comparison of Theory and Experiment: Load-Thrust and Load-Displacement Relations; R = 52.56, S = 12.0, $\overline{\Gamma}$ = 0.15, $[90/45/0/-45]_s$..... 114

54. Comparison of Theory and Experiment: Equilibrium Configurations; R = 52.56, S = 12.0, $\overline{\Gamma}$ = 0.15, $[90/45/0/-45]_s$..... 115

55. Comparison of Theory and Experiment: Surface Strains vs. Applied Load; R = 52.56, S = 12.0, $\overline{\Gamma}$ = 0.15, $[90/45/0/-45]_s$..... 116

56. Comparison of Theory and Experiment: Load-Thrust and Load-Displacement Relations; R = 64.7, S = 6.0, $\overline{\Gamma}$ 0.0, $[(90/0)_4]_s$ 118

57. Comparison of Theory and Experiment: Surface Strains vs. Applied Load; R = 64.7, S = 6.0, $\overline{\Gamma}$ = 0.0, $[(90/0)_4]_s$ ... 119

58. Comparison of Theory and Experimental: Sensitivity of Buckling Load to Load Eccentricity, $[(90/0)_4]_s$ Specimen Group 121

59. Comparison of Theory and Experiment: Sensitivity of Buckling Load to Load Eccentricity, $[(90/0)_3]_s$ Specimen Group 122

60. Comparison of Theory and Experiment: Sensitivity of Buckling Load to Load Eccentricity, $[90/45/0/-45]_s$ Specimen Group 123

B1. Effect of Orthotropy and Lay-up Panel Response 137

C1. Three-Point Bend Test Fixture 141

D1. Measured Initial Geometric Imperfections 144

D2. Comparison of Theory and Experiment: Load-Thrust and Load-Displacement Relations; R = 56.34, S = 12.0, $\overline{\Gamma}$ = 0.0, and 0.05, $[(90/0)_4]_s$ 146

D3. Comparison of Theory and Experiment: Equilibrium Configurations; R=56.34, S=12.0, $\overline{\Gamma}$=0.0, $[(90,0)_4]_s$ 147

E1. Comparison of Theory and Experiment with Matched Initial Stiffness; R = 56.34, S = 12.0, $\overline{\Gamma}$ = 0.0, $[(90/0)_4]_s$ 155

List of Appendices

Appendix		Page
A	Coefficients of Load-Thrust Relationships	128
B	Effect of Orthotropy on Panel Behavior	133
C	Determination of Extensional Stiffnesses and Bending Stiffnesses	138
D	Effect of Geometric Imperfections on Panel Behavior	143
E	Effect of Initial Stiffness on Panel Behavior	151

List of Symbols

$A_1, A_2, \ldots$	- constants of integration
A_{22}	- extensional stiffness, θ direction
B_{22}	- bending-stretching coupling, θ direction
b	- magnitude of asymmetric deformation
D_{22}	- bending stiffness, θ direction
E_{11}, E_{22}	- Young's moduli
$\hat{e}_r, \hat{e}_t$	- deformed radial and tangential unit vectors
H	- panel rise
h	- panel thickness
$\hat{i}_r, \hat{i}_t$	- undeformed radial and tangential unit vectors
K	- change of middle surface curvature
L_s	- panel span
L_x	- panel length in x direction
M_θ	- moment resultant, θ direction
N_θ	- force resultant, θ direction (thrust)
P	- line load intensity
p	- nondimensional line load intensity
$\bar{Q}_{11}, \bar{Q}_{22}$	- reduced, transformed stiffnesses
q	- thrust parameter
R	- undeformed radius
r	- deformed radius
S	- undeformed arc length
S^*	- deformed arc length
$\bar{S}$	- arc-wise position of line load

U	- strain energy
U_d	- strain energy density
u	- tangential displacement
$\bar{u}$	- nondimensional tangential displacement
u_x	- displacement in generator direction
V	- potential of external forces
w	- radial displacement
x	- independent variable in generator direction
z	- independent variable through panel thickness
β	- semi-opening angle
Γ	- nondimensional independent variable
$\bar{\Gamma}$	- nondimensional position of line load
Γ_n	- radial displacement gradient
Γ_t	- tangential displacement gradient
$\vec{\Delta}$	- displacement
σ_{ij}	- stress tensor
ε_{ij}	- strain tensor
ε_{ij}^{o}	- middle surface strain tensor
η	- nondimensional thrust
θ	- independent variable
$\bar{\theta}$	- angular position of line load
κ	- deformed curvature
κ_o	- undeformed curvature
λ	- geometric and material parameter
ν_{12}, ν_{21}	- Poissons' ratios

ξ	- load parameter
Π	- total potential energy
ϕ	- nondimensional radial displacement
$\bar{\phi}$	- nondimensional radial displacement at line load
Ω	- rotation of cross section

Chapter 1

INTRODUCTION

Although the elastic finite-displacement response of shallow cylindrically curved panels has been subjected to extensive consideration in the past fifty years, very little work has been done on the behavior of such panels fabricated from orthotropic materials. The utilization of composite materials in primary structural components in aircraft applications is steadily increasing. The current trend is the implementation of composite materials into the fuselage structure. Figure 1 shows how the fuselage skin may be represented by a shallow cylindrically curved panel.

One concern that must be addressed involves the crashworthiness of a composite fuselage. Crashworthiness studies imply high speed, large deflection behavior of structural components. It is the intent of this study to lay the groundwork for understanding the dynamic, elastic, finite-displacement behavior of shallow cylindrically curved panels fabricated from a fibrous composite material. This will be accomplished by presenting a complete examination, both theoretical and experimental, of the static behavior of such a structure subjected to a line load acting along a cylinder generator. The line load acts toward the center of curvature of the panel. This examination of static behavior is a necessary step before any attempts at determining dynamic behavior are made.

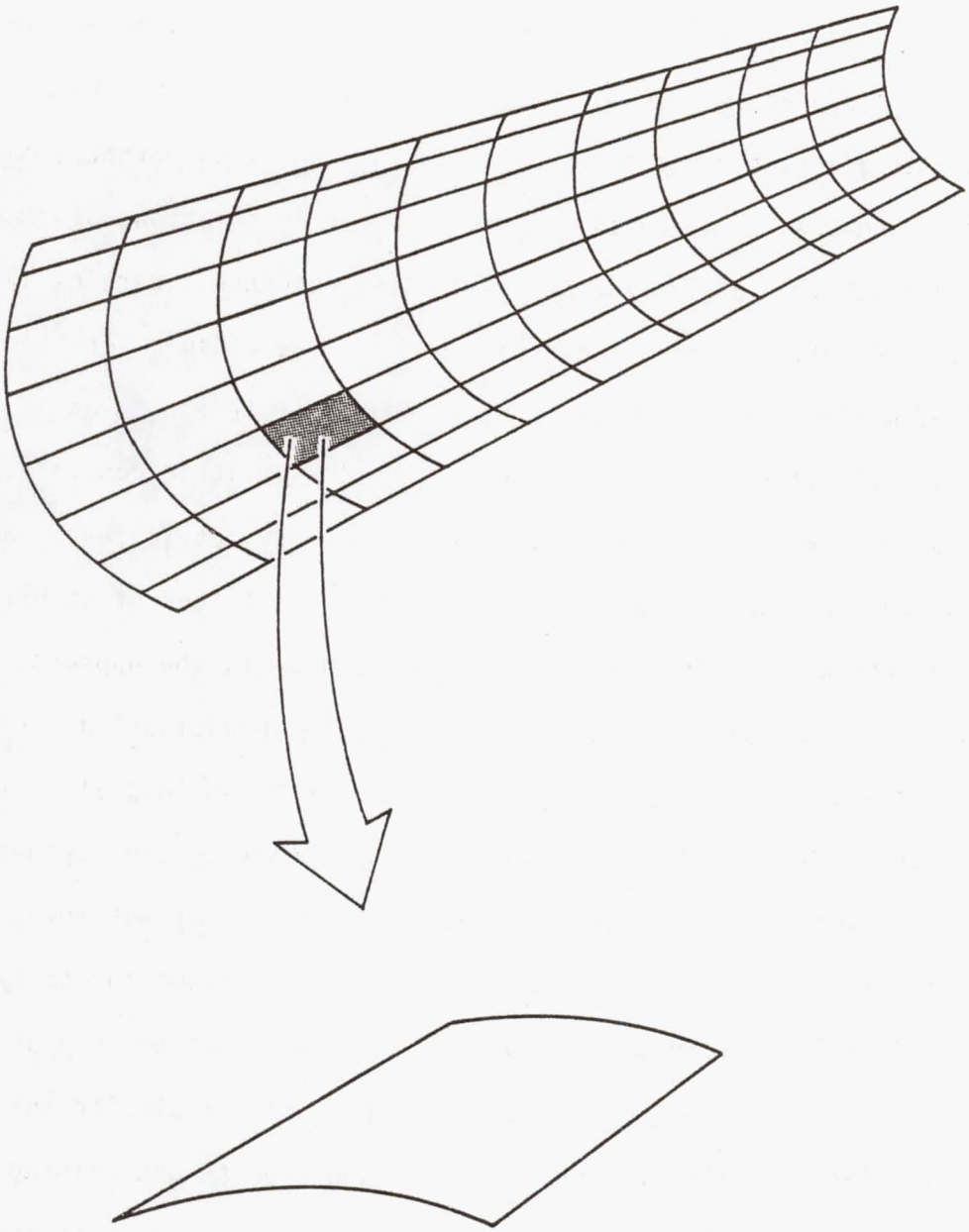

FIG. 1 MODEL OF FUSELAGE SKIN

Previous Work

In 1929, Biezeno [1] investigated the response of a shallow circular arch with pinned ends at a fixed distance apart subjected to a concentrated load acting at midspan. Using two solution methods, one a shallow curved-beam solution and the other a series solution, Biezeno presented a detailed analysis of the symmetric response. Herein, symmetry is defined with respect to displacement and the midspan location on the curved member. Figure 2a illustrates what is referred to as a symmetric response while Fig. 2b illustrates an asymmetric response. No results were presented by Biezeno concerning the asymmetric response except to mention its existence and its importance to loss of stability of the symmetric equilibrium configuration. Following the approach of Biezeno, Fung and Kaplan [2] conducted a complete investigation into the behavior of shallow arches, specifically the case of an initially sinusoidal arch, using a series solution. They investigated the asymmetric displacement mode in greater detail than did Biezeno. It was found that on the primary load-deflection equilibrium path, corresponding to symmetric deformations, asymmetric equilibrium states occurred at unstable bifurcation points. Schreyer and Masur [3] performed a similar analysis on the circular arch with clamped ends. In addition to determining the equilibrium behavior of the structure, they also performed an in-depth analysis of the stability of these equilibrium states. In their study the initial rise-to-span ratio determined whether the buckling of the arch occurred at a limit point on the primary path or whether it occurred at the bifurcation point on the primary path. These first

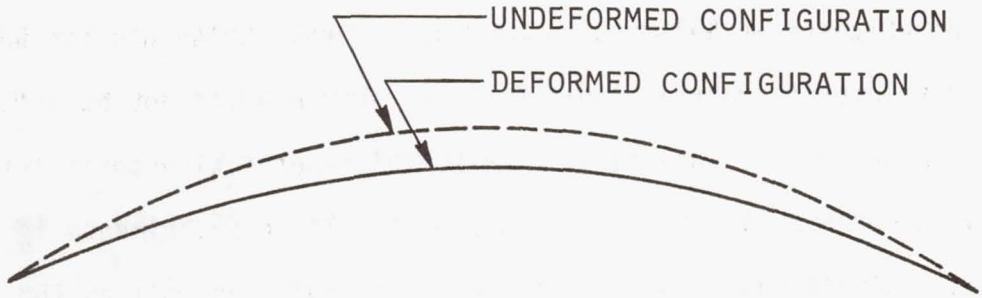

(A) SYMMETRIC

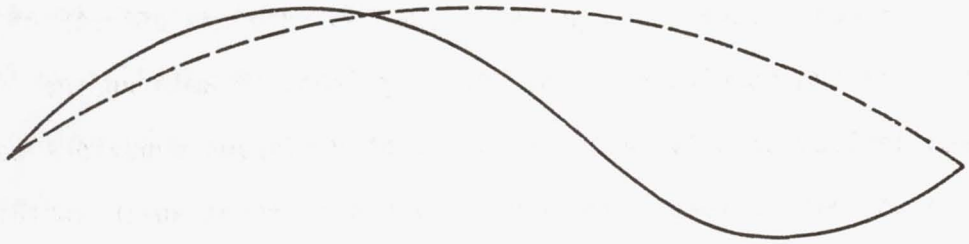

(B) ASYMMETRIC

FIG. 2 SYMMETRIC AND ASYMMETRIC RESPONSE

studies into the finite-deformation behavior of the shallow arch were restricted to isotropic and homogeneous materials with linear elastic behavior and did not consider load eccentricity or geometric imperfections.

In recent years it became obvious that a theory which did not take into account initial imperfections of the structure would not be able to accurately model a real structure. Due to the imperfection sensitivity of some arch structures, it was at times difficult to experimentally verify the analyses put forward. The buckling loads, as well as the entire character of the response, are affected by the imperfections present. Schreyer [4] presented an analysis of the effects of initial imperfections on the response of shallow circular arches with clamped ends. In the study, imperfections in the geometry of the arch, which had the same form as the buckling mode, and eccentricities in the load position were both examined. Both types of imperfections were seen to cause a decrease in the buckling load for certain ranges in geometry. This implied that the arch is an imperfection-sensitive structure. Plaut [5] performed a more thorough investigation into the effects of load position on the magnitude of the buckling load. Examining the pinned-ended shallow circular arch, a number of different behaviors were observed due to load offsets. However, only those arches which exhibited loss of stability at bifurcation points when the load was exactly at midspan were seen to be sensitive to load offset. In such an arch a small perturbation in the load position could cause significant reductions in the predicted buckling loads. Cheung and Babcock [6] performed

an experimental investigation into the effects of load offset on the static buckling load of shallow circular arches. Using aluminum arches with clamped ends, buckling loads were measured for load offsets of up to 6% of the arc length. The results of the experiment show significant reductions in the magnitude of the buckling load with increasing load offset. Taking into account such load-position effects considerably improved the understanding of the response of the shallow arch. However, the vast majority of the work has concentrated on metallic arches. With composite materials playing an increasingly important role in the aerospace industry, the effects of orthotropic materials on the response of the shallow arch was still needed.

Some work on the behavior of orthotropic shallow arches has been done. Nash and Hsu [7] analyzed the structural behavior of a shallow circular arch fabricated from a composite material with the fiber direction normal to the middle surface. In their theory, Nash and Hsu included the effects of transverse shear stresses and transverse normal stresses. The qualitative behavior of their orthotropic arch was essentially the same as for an isotropic arch. As is the case with an isotropic arch, they found the behavior of the arch was controlled by a geometric parameter. In addition to the analytic considerations, they also conducted experiments into the load-displacement relationship up to the buckling load. In the results obtained, a fair agreement between theory and experiment was seen. Marshall, Rhodes, and Banks [8] conducted experiments into the behavior of shallow curved composite panels, also finding good agreement between theory and experiment. These exper-

iments were performed on spherically curved glass-epoxy panels under load control.

Objective of Present Work

The study discussed in this report is intended to extend the present knowledge of the static, large deflection, behavior of orthotropic shallow curved panels. To accomplish this, an exact solution is presented for a simply supported cylindrical panel with a circular cross section and subjected to a line loading along a cylinder generator. The orthotropic axes are parallel to the generator and circumferential directions. Derivation of the equations is presented in Chapter 2. The governing equations are derived using laminated plate theory, nonlinear strain-displacement relations, and applying variational principles. Eccentricities, or offsets, in load position relative to midspan are taken into account. Due to the geometry of the problem under consideration, only a one-dimensional analysis is developed. The one independent variable is related to the circumferential arc length along the panel. Because of the one-dimensional nature of the problem, ordinary differential equations govern the behavior of the panel. These equations are solved in closed form. The aim of this work is to investigate the effects of orthotropic material properties on the behavior of a shallow curved panel. In past work, as has been discussed, the behavior of the structure is assumed to be controlled solely by the geometry. For an orthotropic curved panel, the material properties may also affect the response. This idea is investigated here. In addition, a

load-position sensitivity analysis is presented along with predictions of load vs. displacement, load vs. thrust, and load vs. surface strains. These predictions are presented in Chapter 3. In order to verify the analysis, experimental results of displacement-controlled tests performed on graphite-epoxy curved panels are presented. Chapter 4 describes the experimental set-up while Chapter 5 presents experimental results. Since the tests are run under displacement control, a greater portion of the equilibrium path is stable and predictions of the buckling load under load control may be made with greater confidence. Also, experimental observation of the post-buckling mode, unstable under load control, may be made using displacement control. By comparing analytic and experimental results, the effectiveness of laminated plate theory, in combination with an analysis accounting for large elastic deformations, in predicting the structural response will be shown. In addition, the influence of panel geometry and panel material properties on the response will be illustrated. Finally, Chapter 6 presents conclusions and recommendations for future work.

Chapter 2

DERIVATION OF GOVERNING EQUATIONS

Nomenclature

The coordinate system and notation used for defining the cylindrically curved panel is given in fig. 3. The panel has a radius of curvature R. The radius is measured from the center of curvature, denoted by O, to the geometric middle surface. The semi-opening angle is denoted by β. The independent spatial variables are represented by θ and x. The angle θ is measured positive clockwise from the midspan vertical and the generator coordinate x is measured positive from front to back on the panel. In addition x = 0 at the front. Position through the thickness is given by z, with z being measured positive away from the center of curvature. Furthermore, z = 0 at the middle surface. The total panel thickness is denoted by h. The panel is assumed to be simply supported with a fixed distance L_s between supports. The length of the panel in the x direction is L_x. The panel rise, H, is the vertical distance, measured at midspan, from the line of supports to the middle surface.

The radial displacement of the middle surface is given by w. The radial displacement is positive toward the center of curvature. The tangential displacement, represented by u, is positive toward the right. The line load intensity, assumed to be independent of the x coordinate, is denoted by P and is assumed to act on the middle surface at an arbitrary spatial position denoted by $\overline{\theta}$.

Due to the one-dimensional character of the geometry and loading, the displacements are assumed to be functions only of the spatial vari-

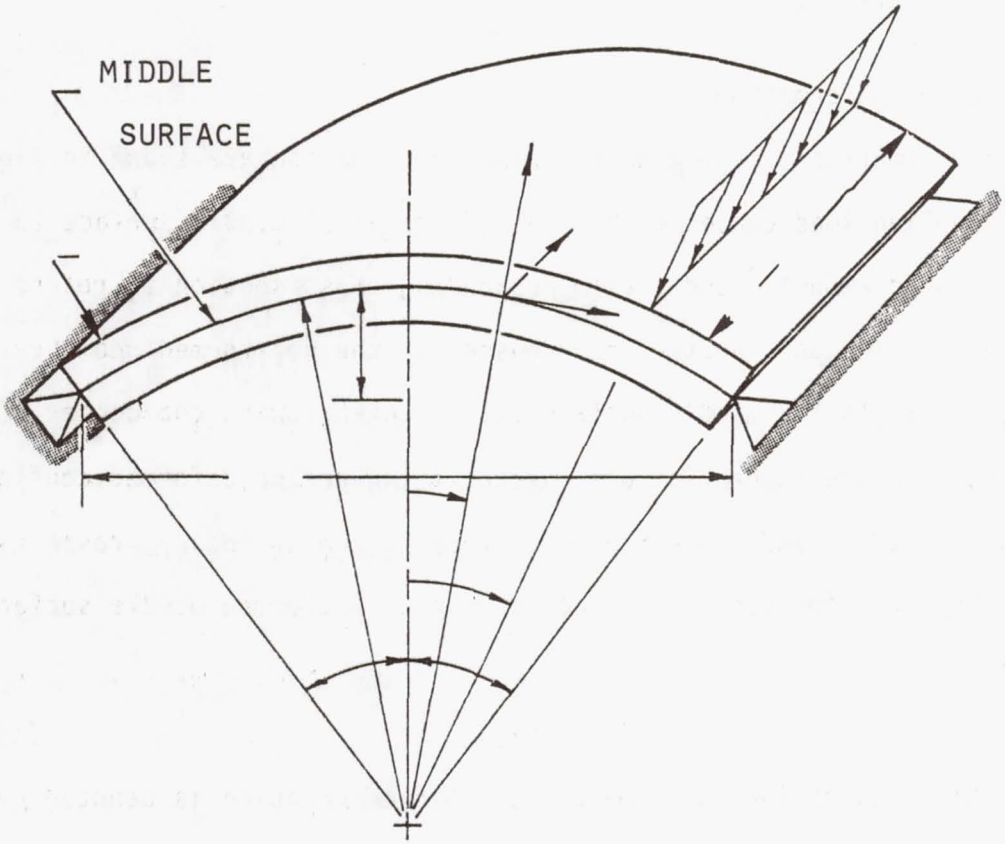

FIG. 3 CYLINDER GEOMETRY AND NOMENCLATURE

able θ. Thus in the analysis, $w = w(\theta)$ and $u = u(\theta)$. Other assumptions to be used in the analysis include the assumptions of a linear elastic material behavior and linear strain variation through the thickness. Also, the panel is assumed to be thin with the transverse normal stress negligible in comparison with the inplane stresses. Transverse shear deformations are neglected.

Kinematics of Deformation

The kinematics of the middle surface deformation are shown in fig. 4. The applied load causes each point of the panel middle surface to displace by an amount $\vec{\Delta}$ and the corresponding cross section to rotate by an amount Ω. The unit vectors to be used for the undeformed geometry are $\hat{i}_r$, normal to the middle surface and directed toward the center of curvature, and the tangential unit vector $\hat{i}_t$. For the deformed configuration the radial and tangential unit vectors are $\hat{e}_r$ and $\hat{e}_t$, respectively. The position vector of a point on the undeformed middle surface is given by,

$$\vec{R} = - R\hat{i}_r. \tag{1}$$

The position vector for the same point after deformation is denoted by,

$$\vec{r} = \vec{R} + \vec{\Delta}. \tag{2}$$

The displacement vector is

$$\vec{\Delta} = w(S)\hat{i}_r + u(S)\hat{i}_t, \tag{3}$$

where the undeformed arc-length is

$$S = R\theta. \tag{4}$$

The length of a differential element of the undeformed arc length is denoted by dS. The length of this differential element of arc length

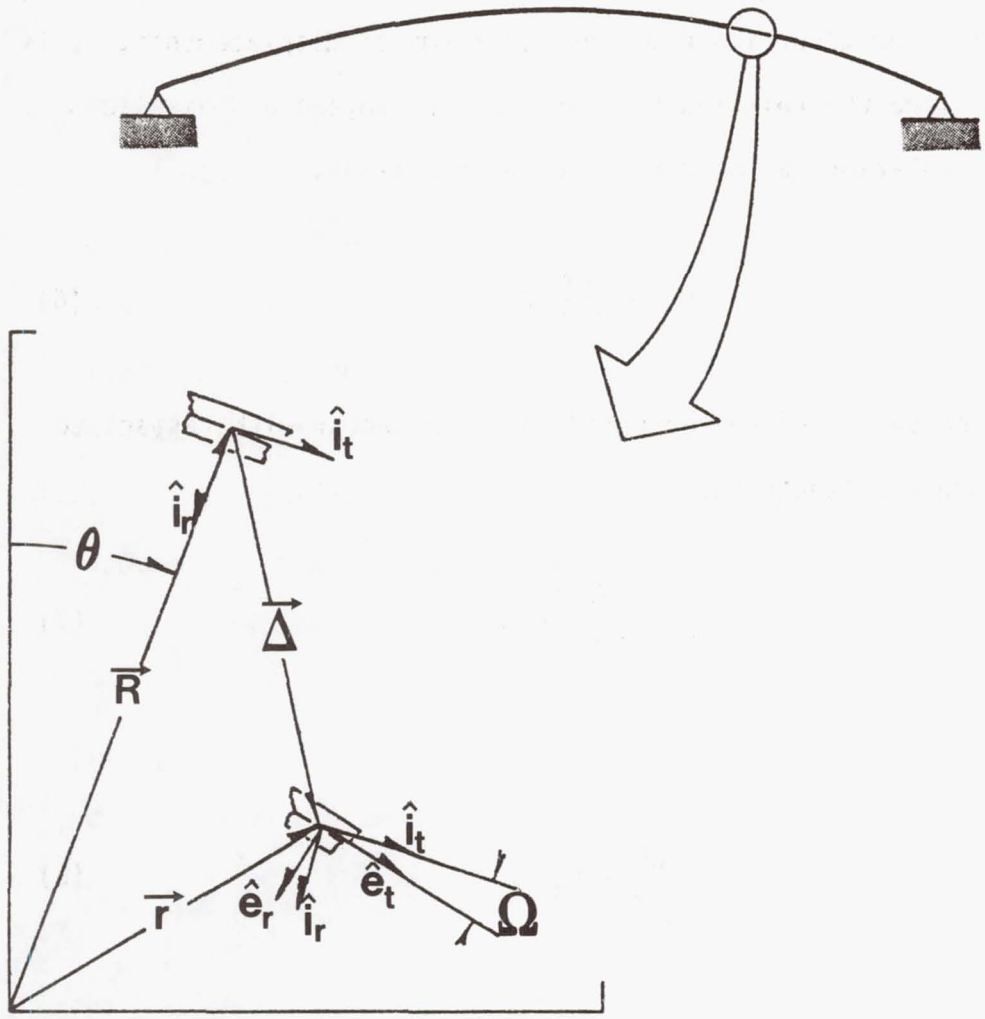

FIG. 4 KINEMATICS OF MIDDLE SURFACE DEFORMATIONS

in the deformed configuration is represented by dS*. By definition the extensional strain of the middle surface is,

$$\varepsilon_\theta^o = \frac{dS^*-dS}{dS}. \tag{5}$$

To derive the governing equations in terms of displacements, it is necessary to find the relation between the arc lengths and displacements. This relation can be determined by realizing,

$$dS^* \equiv \left|\frac{d\vec{r}}{dS}\right| dS. \tag{6}$$

From eq. 2 the change of the deformed position vector with respect to the undeformed arc length is,

$$\frac{d\vec{r}}{dS} = \frac{d\vec{R}}{dS} + \frac{d\vec{\Delta}}{dS}, \tag{7}$$

where,

$$\frac{d\vec{R}}{dS} = \hat{i}_t, \tag{8}$$

and,

$$\frac{d\vec{\Delta}}{dS} = \left(\frac{dw}{dS} + \frac{u}{R}\right)\hat{i}_r + \left(\frac{du}{dS} - \frac{w}{R}\right)\hat{i}_t. \tag{9}$$

To obtain eqs. 8 and 9 use was made of the relations,

$$\frac{d\hat{i}_r}{dS} = -\frac{1}{R}\,\hat{i}_t \text{ and } \frac{d\hat{i}_t}{dS} = +\frac{1}{R}\,\hat{i}_r. \qquad (10),\ (11)$$

Realizing that $+\frac{1}{R}$ represents the initial curvature, κ_o, the displacement gradients, Γ_n and Γ_t, are defined as,

$$\Gamma_n = \frac{dw}{dS} + \kappa_o u \text{ and } \Gamma_t = \frac{du}{dS} - \kappa_o w \qquad (12),\ (13)$$

so that eq. 7 becomes,

$$\frac{d\vec{r}}{dS} = \Gamma_n \hat{i}_r + (1 + \Gamma_t)\hat{i}_t. \qquad (14)$$

From eqs. 6 and 14 the deformed arc length is related to the undeformed arc length by the relation,

$$dS^* = \left[(1 + \Gamma_t)^2 + \Gamma_n^2\right]^{1/2} dS. \qquad (15)$$

The extensional strain, ε_θ^o, is now calculated to be,

$$\varepsilon_\theta^o = \left[(1 + \Gamma_t)^2 + \Gamma_n^2\right]^{1/2} - 1 \quad . \qquad (16)$$

Squaring the first term in the radical and applying the binomial expansion leads to,

$$\varepsilon_\theta^o = \Gamma_t + 1/2\ \Gamma_n^2 + O(\Gamma^3). \qquad (17)$$

By assuming the displacement gradients remain small, i.e.,

$$0 < |\Gamma_t| << 1 \text{ and } 0 < |\Gamma_n| << 1, \qquad (18), (19)$$

terms of third order and higher are dropped from the strain expression. This results in the approximate strain-displacement relationship,

$$\varepsilon_\theta^o = \frac{du}{dS} - \kappa_o w + \frac{1}{2}\left(\frac{dw}{dS} + \kappa_o u\right)^2. \qquad (20)$$

The configuration of the deformed middle surface is specified by the position vector $\vec{r}(S^*)$. Let $\kappa(S^*)$ represent the curvature of the normal section of this surface perpendicular to the x axis. Then the differential geometry of this normal section requires

$$\frac{d\vec{r}}{dS^*} = \hat{e}_t \qquad (21)$$

$$\frac{d\hat{e}_r}{dS^*} = -\kappa\hat{e}_t \qquad (22)$$

$$\frac{d\hat{e}_t}{dS^*} = \kappa\hat{e}_r \qquad (23)$$

These expressions are analogous to eqs. 8, 10, and 11 for the undeformed normal section of the middle surface. The unit tangent vector, eq. 21, is related to the displacement gradients, eqs. 12 and 13, by using the chain rule to relate S* to S, and then using eqs. 5 and 14. The result is

$$\hat{e}_t = [\Gamma_n \hat{i}_r + (1+\Gamma_t)\hat{i}_t]/(1+\varepsilon_\theta^o) \ . \tag{24}$$

Now define the clockwise angle of rotation of the normal section due to deformation as Ω; see fig. 4. Thus

$$\hat{e}_t = \sin(\Omega)\hat{i}_r + \cos(\Omega)\hat{i}_t \ , \tag{25}$$

and

$$\hat{e}_r = \cos(\Omega)\hat{i}_r - \sin(\Omega)\hat{i}_t \ . \tag{26}$$

Comparing eqs. 24 and 25, the trignometric functions of the rotation angle are

$$\sin(\Omega) = \frac{\Gamma_n}{1+\varepsilon_\theta^o} \tag{27}$$

$$\cos(\Omega) = \frac{1+\Gamma_t}{1+\varepsilon_\theta^o} \tag{28}$$

$$\tan(\Omega) = \frac{\Gamma_n}{1+\Gamma_t} \tag{29}$$

Consider the deformation of a surface parallel to the middle surface specified by a nonzero constant value of z. Let dS_z and $dS_z{*}$ designate the undeformed and deformed differential arc-lengths, respectively, of the normal section to the parallel surface. Consistent with the definition of the middle surface strain, eq. 5, the circumferential strain of the parallel surface is defined as,

$$\varepsilon_\theta = \frac{dS_z^* - dS_z}{dS_z} . \tag{30}$$

A material point located by the position vector $\vec{R}_z$ on the undeformed parallel surface is located by position vector $\vec{r}_z$ on the deformed parallel surface. It is assumed that normals to the undeformed middle surface remain normal and undeformed with respect to the middle surface during deformation (Love-Kirchhoff hypothesis). Thus these position vectors are

$$\vec{R}_z = -(R+z)\hat{i}_r, \quad \text{and } \vec{r}_z = \vec{r} - z\hat{e}_r . \qquad (31),(32)$$

Using eqs. 8, 10, 21, and 22, the differentials of these vectors with z held constant are

$$d\overline{R}_z = -(1+z\kappa_o)dS\ \hat{i}_t, \text{ and } d\overline{r}_z = -(1+z\kappa)dS^*\ \hat{e}_t. \qquad (33),(34)$$

The magnitudes of these differential vectors are

$$dS_z = (1+z\kappa_o)dS, \text{ and } dS_z^* = (1+z\kappa)dS^* . \qquad (35),(36)$$

Substitute these into eq. 30, and use eq. 5, to get

$$\varepsilon_\theta = \frac{1+z\kappa}{1+z\kappa_o} \cdot (1+\varepsilon_\theta^o) - 1 . \tag{37}$$

For thin shells,

$$0 < |z\kappa_0| \leq |h\kappa_0| << 1 \ . \tag{38}$$

Assume the shell is thin, and expand the denominator of eq. 37 in a power series in z using the binomial series to get

$$\varepsilon_\theta = \varepsilon_\theta^0 + (1+\varepsilon_\theta^0)[z(\kappa-\kappa_0) + O(z^2)] \ . \tag{39}$$

Consequently, for thin shells and small strains the parallel surface strain is approximated by,

$$\varepsilon_\theta = \varepsilon_\theta^0 + z(\kappa-\kappa_0) \ . \tag{40}$$

This result shows the parallel surface strain is determined by the middle surface strain and its change in curvature.

To complete the kinematics, the change in curvature of the middle surface is needed. According to eq. 23 the curvature of the normal section of the deformed middle surface is

$$\kappa = \hat{e}_r \cdot \frac{d\hat{e}_t}{dS^*} \ . \tag{41}$$

Using the chain rule and eq. 5 this becomes

$$\kappa = \hat{e}_r \cdot \frac{1}{1+\varepsilon_\theta^0} \frac{d\hat{e}_t}{dS} \ . \tag{42}$$

From eqs. 10, 11, 25, and 26, the derivative of the deformed tangent unit vector with respect to the undeformed arc length is,

$$\frac{d\hat{e}_t}{dS} = \left(\kappa_o + \frac{d\Omega}{dS}\right) \hat{e}_r \ . \tag{43}$$

Substitute this into eq. 41 to get

$$\kappa = \frac{1}{(1+\varepsilon_\theta^o)} \left(\kappa_o + \frac{d\Omega}{dS}\right) \ . \tag{44}$$

Using eqs. 27 and 28, the derivative of the rotation with respect to the undeformed arc length is,

$$\frac{d\Omega}{dS} = \frac{1}{1+\varepsilon_\theta^o} \left[\cos \Omega \frac{d\Gamma_n}{dS} - \sin \Omega \frac{d\Gamma_t}{dS}\right] \tag{45}$$

For small strains and rotations this is approximated by

$$\frac{d\Omega}{dS} = \frac{d\Gamma_n}{dS} \ . \tag{46}$$

The implication of the approximation in eq. 46 is important. If the rotations are assumed to be small, and if the load-deformation behavior of a curved panel from no-load to complete snap-through is to be investigated, then the initial curvature of the panel must be small. This implies the work here is limited to shallow shell theory. The curvature, eq. 44, can now be expressed as

$$\kappa = \kappa_o + \frac{d\Gamma_n}{dS} , \tag{47}$$

noting that the small strain assumption leads to the approximation,

$$1 + \varepsilon_\theta^o \approx 1. \tag{48}$$

Substituting for the displacement gradient, the curvature-displacement relationship can be determined from eq. 47 as

$$\kappa = \kappa_o + \frac{d^2w}{dS^2} + \kappa_o \frac{du}{dS} . \tag{49}$$

From shallow shell theory the tangential displacement u is assumed to be small relative to $\frac{dw}{dS}$ so that the normal displacement gradient becomes,

$$\Gamma_n = \frac{dw}{dS}. \tag{50}$$

Thus for shallow panels, the strain-displacement and curvature-displacement relations are,

$$\varepsilon_\theta^o = \frac{du}{dS} - \kappa_o w + \frac{1}{2} \left(\frac{dw}{dS}\right)^2 \tag{51}$$

$$\kappa = \kappa_o + \frac{d^2w}{dS^2} . \tag{52}$$

The change in middle surface curvature, K, is defined to be

$$K = \kappa - \kappa_o = d^2w/dS^2 \tag{53}$$

Total Potential Energy

As previously stated, the governing equations will be derived using variational principles. To do so it is necessary to form the total potential energy of the system. By definition the total potential energy is,

$$\pi = U + V \tag{54}$$

where U is the strain energy stored in the structure and V is the potential of the loading. The strain energy density, U_d, is defined as,

$$U_d = \frac{1}{2}\,\sigma_{ij}\varepsilon_{ij}. \tag{55}$$

Since transverse shear strains and the transverse normal stress are assumed to be negligible in comparison to the inplane stresses and strains, the strain energy density reduces to,

$$U_d = \frac{1}{2}\,\{\sigma_x\varepsilon_x + \sigma_{x\theta}\gamma_{x\theta} + \sigma_\theta\varepsilon_\theta\} \tag{56}$$

The previously mentioned one-dimensional nature of the geometry suggests that,

$$\frac{\partial}{\partial x} = 0 \text{ and } u_x = 0, \tag{57}$$

where u_x is the displacement in the x direction. Using these assumptions the strain energy density is reduced further to,

$$U_d = \frac{1}{2}\,\sigma_\theta \varepsilon_\theta . \tag{58}$$

Since the variables are independent of x, the total strain energy, using eq. 58, is,

$$U = \frac{L_x}{2} \int_S \int_z \sigma_\theta \varepsilon_\theta dSdz \ , \tag{59}$$

where L_x is the length of the panel in the x direction.

The constitutive law for an orthotropic material in the state of plane stress described here is,

$$\begin{Bmatrix} \sigma_x \\ \sigma_\theta \\ \sigma_{x\theta} \end{Bmatrix} = [\overline{Q}] \begin{Bmatrix} 0 \\ \varepsilon_\theta \\ 0 \end{Bmatrix} \ , \tag{60}$$

where the $\overline{Q}$ matrix is the transformed reduced stiffness matrix. Equation 60 is written in structural coordinates. For a more complete treatment of orthotropic constitutive relations see [9]. The stress in the θ direction is,

$$\sigma_\theta = \overline{Q}_{22} \varepsilon_\theta . \tag{61}$$

Substituting this relation into eq. 59 yields,

$$U = \frac{L_x}{2} \int_S \int_z \overline{Q}_{22} \varepsilon_\theta^2 dSdz \ . \tag{62}$$

Strain away from the middle surface, from eq. 40, is written in terms of the middle surface strain and curvature change as,

$$\varepsilon_\theta = \varepsilon_\theta^o + zK \ . \tag{63}$$

With this expression the constitutive law is,

$$\sigma_\theta = \overline{Q}_{22}(\varepsilon_\theta^o + zK). \tag{64}$$

Integrating this expression with respect to z yields,

$$N_\theta = A_{22}\varepsilon_\theta^o + B_{22}K \ , \tag{65}$$

the force resultant, N_θ, being defined as,

$$N_\theta = \int_z \sigma_\theta dz \ . \tag{66}$$

The extensional stiffness, A_{22}, and bending-stretching coupling stiffness, B_{22}, are defined by,

$$A_{22} = \sum_{k=1}^{N} (\overline{Q}_{22})_k (z_k - z_{k-1}) \tag{67}$$

$$B_{22} = \frac{1}{2} \sum_{k=1}^{N} (\overline{Q}_{22})_k \ (z_k^2 - z_{k-1}^2) \ , \tag{68}$$

where k is the lamina number and z_k and z_{k-1} ($z_k > z_{k-1}$) define the location of the kth lamina in the laminate. Multiplying the constitutive law of eq. 64 by z and integrating over z yield the expression for the moment resultant, M_θ,

$$M_\theta = B_{22}\varepsilon_\theta^o + D_{22}K, \tag{69}$$

where

$$M_\theta = \int_z \sigma_\theta z dz. \tag{70}$$

The bending stiffness, D_{22}, is defined as,

$$D_{22} = \frac{1}{3} \sum_{k=1}^{N} (\overline{Q}_{22})_k (z_k^3 - z_{k-1}^3) \ . \tag{71}$$

Since only symmetric lay-ups are to be examined, the stiffness B_{22} is set equal to zero in the analysis.

Substituting the strain expression of eq. 63 into eq. 62 and integrating over z yields,

$$U = \frac{L_x}{2} \int_S \{A_{22}(\varepsilon_\theta^o)^2 + D_{22}(K)^2\} dS \ . \tag{72}$$

Taking the first variation of the strain energy and substituting the constitutive relations of eqs. 65 and 69 into eq. 72 leads to,

$$\delta U = L_x \int_S \{N_\theta \delta\varepsilon_\theta^o + M_\theta \delta K\} dS \ . \tag{73}$$

From eqs. 51 and 53 the variations of strain and curvature change are written in terms of the displacement functions as,

$$\delta\varepsilon_\theta^o = \delta\left(\frac{du}{dS}\right) - \kappa_o\delta w + \frac{dw}{dS}\,\delta\left(\frac{dw}{dS}\right) \tag{74}$$

$$\delta K = \delta\left(\frac{d^2w}{dS^2}\right) \tag{75}$$

Upon substitution of these relationships into eq. 73 and adding the variation of the load potential, the first variation of the total potential energy is,

$$\begin{aligned}\delta\pi = L_x \int_S \{&N_\theta\delta\left(\frac{du}{dS}\right) - N_\theta\kappa_o\delta w + N_\theta\,\frac{dw}{dS}\,\delta\left(\frac{dw}{dS}\right)\\ &+ M_\theta\delta\left(\frac{d^2w}{dS^2}\right)\}dS - PL_x\delta w(\overline{S})\ .\end{aligned} \tag{76}$$

The arc-wise location where the line load acts, $\overline{S}$, is given by

$$\overline{S} = R\overline{\theta}\ . \tag{77}$$

Furthermore, one-half the arc length of the undeformed panel, S_o, is given by

$$S_o = R\beta\ . \tag{78}$$

The theorem of stationary total potential energy states that the first variation of the potential energy is zero for equilibrium configurations. By setting $\delta\pi$ to zero in eq. 76 and integrating the first, third and fourth terms by parts, with the integration taking place over the intervals $-S_o < S < \overline{S}$ and $\overline{S} < S < S_o$, the following relationship results:

$$\int_{-S_o}^{\overline{S}} \int_{\overline{S}}^{S_o} [\{-\kappa_o N_\theta - \frac{dN_\theta}{dS}\frac{dw}{dS} - N_\theta \frac{d^2w}{dS^2} + \frac{d^2M}{dS^2}\}\delta w - \frac{dN_\theta}{dS}\delta u]dS$$

$$+ N_\theta \delta u|_{-S_o}^{\overline{S}} + N_\theta \delta u|_{\overline{S}}^{S_o} + N_\theta \frac{dw}{dS}\delta w|_{-S_o}^{\overline{S}} + N_\theta \frac{dw}{dS}\delta w|_{\overline{S}}^{S_o}$$

$$+ M_\theta \delta(\frac{dw}{dS})|_{-S_o}^{\overline{S}} + M_\theta \delta(\frac{dw}{dS})|_{\overline{S}}^{S_o} - \frac{dM_\theta}{dS}\delta w|_{-S_o}^{\overline{S}} - \frac{dM_\theta}{dS}\delta w|_{\overline{S}}^{S_o} \qquad (79)$$

$$- P\delta w(\overline{S}) = 0 \ .$$

It was necessary to break the integration into the intervals due to the discontinuous nature of the loading. Since the variations on the displacement are assumed to be arbitrary, the following governing equations and boundary conditions are obtained:

$$\frac{dN_\theta}{dS} = 0 \qquad (80)$$

$$- \kappa_o N_\theta - \frac{dN_\theta}{dS}\frac{dw}{dS} - N_\theta \frac{d^2w}{dS^2} + \frac{d^2M_\theta}{dS^2} = 0 \qquad (81)$$

over the intervals $- S_o < S < \overline{S}$ and $\overline{S} < S < S_o$. At $S = -S_o$ and $S = S_o$;

$$\text{either } N_\theta = 0 \text{ or } u \text{ is known,} \tag{82}$$

$$\text{either } N_\theta \frac{dw}{dS} - \frac{dM_\theta}{dS} = 0 \text{ or } w \text{ is known,} \tag{83}$$

$$\text{either } M_\theta = 0 \text{ or } \frac{dw}{dS} \text{ is known.} \tag{84}$$

The transition conditions at $S = \overline{S}$,

$$u \text{ is continuous,} \tag{85}$$

$$w \text{ is continuous,} \tag{86}$$

$$\frac{dw}{dS} \text{ is continuous,} \tag{87}$$

$$M_\theta \text{ is continuous,} \tag{88}$$

$$N_\theta \text{ is continuous,} \tag{89}$$

and

$$\frac{dM_\theta(\overline{S^+})}{dS} - \frac{dM_\theta(\overline{S^-})}{dS} - P = 0 \ . \tag{90}$$

Equation 90 indicates that the shear force experiences a jump at $S = \overline{S}$.

An additional equation can be obtained by integrating both sides of eq. 51 over the arc length $S_o < S < S_o$. Using eq. 65, recalling $B_{22} = 0$, eq. 51 assumes the form

$$\frac{N_\theta}{A_{22}} = \frac{du}{dS} - \kappa_o w + \frac{1}{2}\left(\frac{dw}{dS}\right)^2. \tag{91}$$

From eq. 80, N_θ is constant with S. Therefore integration of eq. 91 results in

$$N_\theta = \frac{A_{22}}{2S_o} \int_{-S_o}^{S_o} \{-\kappa_o w + \frac{1}{2} (\frac{dw}{dS})^2\} dS \ , \tag{92}$$

where u vanishes at the fixed ends. Using eq. 80 in eq. 81, results in

$$- \kappa_o N_\theta - N_\theta \frac{d^2 w}{dS^2} + \frac{d^2 M_\theta}{dS^2} = 0 \ . \tag{93}$$

Equations 92 and 93 are the equations governing the deformation of the panel. For the panel configuration in question (see fig. 3) the boundary conditions are,

$$u = 0 \tag{94}$$

$$w = 0 \tag{95}$$

$$M_\theta = 0 \tag{96}$$

at $S = \pm S_o$. Transition conditions, applied at $S = \overline{S}$, are,

$$u(\overline{S}^-) = u(\overline{S}^+) \tag{97}$$

$$w(\overline{S}^-) = w(\overline{S}^+) \tag{98}$$

$$\frac{dw}{dS}(\overline{S}^-) = \frac{dw}{dS}(\overline{S}^+) \tag{99}$$

$$M_\theta(\overline{S}^-) = M_\theta(\overline{S}^+) \tag{100}$$

$$N_\theta(\overline{S}^-) = N_\theta(\overline{S}^+) \tag{101}$$

$$\frac{dM_\theta(\overline{S}^-)}{dS} - \frac{dM_\theta(\overline{S}^+)}{dS} - P = 0 \ . \tag{102}$$

In order to facilitate the analysis, the governing equations are nondimensionalized. Since

$$dS = Rd\theta \ , \tag{103}$$

then

$$\frac{d^n}{dS^n} = \frac{1}{R^n}\frac{d^n}{d\theta^n} \ . \tag{104}$$

The nondimensional quantities are defined as follows

$$\eta = \frac{N_\theta}{A_{22}\beta^2} \tag{105}$$

$$\phi = \frac{w}{R\beta^2} \tag{106}$$

$$\overline{u} = \frac{u}{R\beta^3} \tag{107}$$

$$\Gamma = \frac{\theta}{\beta} \tag{108}$$

$$p = \frac{P}{A_{22}\beta^3} \tag{109}$$

Using this nondimensional scheme along with the constitutive relations of eqs. 65 and 69, the governing equations can be rewritten as,

$$\frac{1}{\lambda^4}\frac{d^4\phi}{d\Gamma^4} - \eta\left(\frac{d^2\phi}{d\Gamma^2} + 1\right) = 0 \tag{110}$$

and

$$\eta = -\frac{1}{2}\int_{-1}^{1}\left\{\phi - \frac{1}{2}\left(\frac{d\phi}{d\Gamma}\right)^2\right\} \ , \tag{111}$$

where λ is a nondimensional parameter defined as,

$$\lambda^4 = \frac{A_{22}R^2\beta^4}{D_{22}} . \tag{112}$$

Equation 110 corresponds to eq. 93 while eq. 111 corresponds to eq. 92.

By using the definitions of the bending and extensional stiffnesses for an isotropic material, the parameter λ is,

$$\lambda^4 = 48\left(\frac{H}{h}\right)^2 . \tag{113}$$

It is seen that the material dependence is eliminated and λ is a function of geometry only. In contrast, with an orthotropic material λ is also a function of the material properties. It should be emphasized that the solution to eqs. 110 and 111 depend only on the parameter λ. Since, for an orthotropic material, λ incorporates both material and geometric properties of the panel, all panel characteristics influence this single parameter.

The nondimensional boundary conditions and transition conditions, using eqs. 105-109, are,

$$\bar{u} = 0 \text{ at } \Gamma = \pm 1 \tag{114}$$

$$\phi = 0 \text{ at } \Gamma = \pm 1 \tag{115}$$

$$\frac{d^2\phi}{d\Gamma^2} = 0 \text{ at } \Gamma = \pm 1 \tag{116}$$

$$\bar{u}(\bar{\Gamma}^-) = \bar{u}(\bar{\Gamma}^+) \tag{117}$$

$$\phi(\bar{\Gamma}^-) = \bar{\phi}(\bar{\Gamma}^+) \tag{118}$$

$$\frac{d\phi}{d\Gamma}(\bar{\Gamma}^-) = \frac{d\phi}{d\Gamma}(\bar{\Gamma}^+) \tag{119}$$

$$\frac{d^2\phi(\bar{\Gamma}^-)}{d\Gamma^2} = \frac{d^2\phi(\bar{\Gamma}^+)}{d\Gamma^2} \tag{120}$$

$$\eta(\bar{\Gamma}^-) = \eta(\bar{\Gamma}^+) \tag{121}$$

$$\frac{d^3\phi(\bar{\Gamma}^-)}{d\Gamma^3} = \frac{d^3\phi(\bar{\Gamma}^+)}{d\Gamma^3} + p\lambda^4. \tag{122}$$

Chapter 3

SOLUTION TO GOVERNING EQUATION AND NUMERICAL RESULTS

The governing differential equation developed in the previous section, eq. 110, appears to be a linear ordinary differential equation with η being an unknown constant. This is not the case since η is actually a nonlinear function of the displacement. However, linear analysis may be used to find the functional form of the radial displacement, $\phi(\Gamma)$. The nonlinearity of the problem manifests itself through the second governing equation, eq. 111. Since the functional form of $\phi(\Gamma)$ is established by eq. 110, eq. 111 results in a transcendental equation for η. Since only compressive middle surface strains (i.e., $N_\theta < 0$) are of interest, the thrust parameter q is defined such that,

$$q^2 = -\eta\lambda^4 \tag{123}$$

Substituting this expression into the governing equations yields,

$$\frac{d^4\phi}{d\Gamma^4} + q^2\left(\frac{d^2\phi}{d\Gamma^2} + 1\right) = 0 \tag{124}$$

$$q^2 = \frac{\lambda^4}{2} \int_{-1}^{+1} \left\{\phi - \frac{1}{2}\left(\frac{d\phi}{d\Gamma}\right)^2\right\} d\Gamma \ . \tag{125}$$

Equation 124 can be solved in closed form. However, the form of the solution depends on the value of q. The solutions for various values of q are discussed below.

Midspan loading: $q \neq 0$ and $q \neq \frac{n\pi}{2}$, $n = 1, 3, 5, \ldots$

With the load acting radially at midspan, $\overline{\Gamma} = 0$, and with $q \neq 0$ and $q \neq \frac{n\pi}{2}$, where $n = 1, 3, 5, \ldots$, the general solution to eq. 124 for the radial displacement is

$$\phi(\Gamma) = A_1 + A_2\Gamma - \frac{1}{2}\Gamma^2 + A_3 \cos(q\Gamma) + A_4 \sin(q\Gamma) \tag{126}$$

in each of the intervals $-1 < \Gamma < 0$ and $0 < \Gamma < 1$. Applying the boundary conditions, eqs. 114-116, on each interval, and the transition conditions, eqs. 117-122, at $\overline{\Gamma} = 0$ yields,

$$\begin{aligned}\phi(\Gamma) = {} & b \sin(q\Gamma) + \frac{1}{q^2}\left(1 - \frac{\cos(q\Gamma)}{\cos(q)}\right) + \frac{1}{2}(1 - \Gamma^2) \\ & - \frac{p\lambda^4}{2q^2}\left\{1 - |\Gamma| - \frac{1}{q}\tan(q)\cos(q\Gamma) + \frac{1}{q}\sin(q|\Gamma|)\right\} .\end{aligned} \tag{127}$$

This solution is valid over both intervals. In this expression b represents the magnitude of the asymmetric displacement response. The following conditions on b are determined from the boundary condition requiring the moment to vanish at the edges:

$$\text{if } q \neq n\pi \text{ then } b = 0$$

$$\text{if } q = n\pi \text{ then } b \neq 0,$$

where $n = 1, 2, 3, \ldots$. To complete the solution process the functional form of $\phi(\Gamma)$, eq. 127, is substituted into eq. 125. This relates the thrust parameter q to the nondimensional applied load, p. After some algebra this relationship is written as,

$$A\xi^2 + B\xi + C = 0 \ , \tag{128}$$

where A, B, and C are functions of q and λ, and

$$\xi = p\lambda^4. \tag{129}$$

Appendix A contains the functional form of A, B, and C for all cases considered here. For a given panel, λ is specified. In eq. 128, by specifying the thrust parameter q, a quadratic equation can be solved to obtain the corresponding load, p. This is in opposition to solving eq. 128 as a transcendental equation for the thrust parameter if loads are first specified. In this solution procedure it is important to recognize that eq. 128 may have two real roots, one real root, or no real roots, depending on the values of λ and q. Each real root corresponds to a separate equilibrium configuration. Having found the relationship between load and thrust, the load-displacement relationship follows from eq. 127.

For $q = n\pi$, $b \neq 0$, there is an equation similar to eq. 128 which relates the applied load to the magnitude of the asymmetric deformation, b. It also originates from eq. 125. This relationship is given by the expression,

$$Db^2 = A\xi^2 + B\xi + C. \tag{130}$$

Here A, B, and D are constants depending only on the value of n. Constant C depends on n and λ. Again these constants are expressed in Appendix A. Real solutions for the asymmetric amplitude b require the right-hand-side of eq. 130 to be nonnegative. Consequently, not all

integer values of n are permissible for a specific value of λ. Notice that two asymmetric configurations are determined from eq. 130 at given load if the right-hand-side is positive.

Midspan Loading: q = 0

When the thrust is equal to zero eq. 127 is not the correct functional form of $\phi(\Gamma)$. Setting q = 0 in the governing equation, eq. 110, a new functional form of $\phi(\Gamma)$ is obtained. Applying the boundary conditions (eqs. 114-116) and the transition conditions (eqs. 117-122) the functional form of the radial displacement is,

$$\phi(\Gamma) = \xi \left\{\frac{|\Gamma^3|}{12} - \frac{\Gamma^2}{4} + \frac{1}{6}\right\} . \tag{131}$$

By substituting eq. 131 into eq. 125 the relationship,

$$\xi^2 - \frac{25}{4}\xi = 0 , \tag{132}$$

is obtained for determining the loads at which the thrust parameter, and thus the middle surface thrust, N_θ, vanishes. This occurs at either $\xi = 0$ or $\xi = \frac{25}{4}$. The $\xi = 0$ solution states, as expected, that there is no thrust in the panel if there is no load. However, the nonzero solution to eq. 132 indicates that there is a loaded and deformed state of the panel for which there is no thrust in the panel. In this special situation the load is resisted by bending only.

Midspan Loading: $q = \frac{n\pi}{2}$, $n = 1, 3, 5, \ldots$

The functional form for $\phi(\Gamma)$ in eq. 127 is incorrect when $q = \frac{n\pi}{2}$, $n = 1, 3, 5, \ldots$. In this case the linear inhomogeneous mathematical problem for $\phi(\Gamma)$, given by eq. 124, the boundary conditions, and the transition conditions, does not have a unique solution. The mathematical reason for this is found in Fredholm's alternative theorem [10, pg. 547]. The associated adjoint homogeneous problem for $\phi(\Gamma)$ has nontrivial solutions (eigenfunctions) associated with these values of q (eigenvalues). Consequently the conditions for a solution to $\phi(\Gamma)$ require,

$$\xi\ \phi_m(0) = \int_{-1}^{+1} q^2\ \phi_m(\Gamma)d\Gamma\ , \tag{133}$$

where $\phi_m(\Gamma) = A_m \cos(\frac{m\pi\Gamma}{2})$, $m = 1, 3, 5, \ldots$ are the eigenfunctions of the associated homogeneous problem. (Equation 133 is equivalent to the "inhomogeneity" being orthogonal to the eigenfunctions.) Equation 133 determines the load for the given values of the thrust. The displacement functions which result from this are,

$$\begin{aligned}\phi_n(\Gamma) = \frac{1}{2}\ (1 - \Gamma^2) + A_n^*\ \cos(q\Gamma) + \frac{2\sin(\frac{n\pi}{2})}{n\pi}\ (|\Gamma| - 1) \\ + (\frac{2}{n\pi})^2\ \{1 - \sin(\frac{n\pi}{2})\ \sin(q|\Gamma|)\}\ ,\end{aligned} \tag{134}$$

$n = 1, 3, 5, \ldots, n_{max}$. The values of A_n^* are found by substituting eq. 134 into eq. 125. This yields

$$A(A_n^*)^2 + BA_n^* + C = 0 \ , \tag{135}$$

where A, B, and C are constants depending on the values of n and λ. Appendix A presents the coefficients A, B, C. The solution for ϕ is not unique in this case. The finite number of these solutions, n_{max}, follows from the requirement of real solutions to eq. 135.

Eccentric Loading: $q \neq 0$ and $q \neq \frac{n\pi}{2}$, $n = 1, 2, 3, \ldots$

For loads acting radially at the location $\Gamma = \overline{\Gamma}$, $\overline{\Gamma} \neq 0$, the general solution for the radial displacement, with $q \neq 0$, $q \neq \frac{n\pi}{2}$, is

$$\begin{aligned}\phi(\Gamma) = {} & \frac{1}{q^2}\left(1 - \frac{\cos(q\Gamma)}{\cos(q)}\right) + \frac{1}{2}\left(1 - \Gamma^2\right) - \frac{p\lambda^4}{2q^2}\{1 + \overline{\Gamma}\,\mathrm{sgn}(\Gamma) \\ & - \overline{\Gamma}\,\Gamma - |\Gamma| - \frac{1}{q}\tan(q)\cos(q\overline{\Gamma})\cos(q\Gamma) \\ & + \frac{1}{q}\,\mathrm{sgn}(\Gamma)\sin(q\overline{\Gamma})\cos(q\Gamma) - \frac{1}{q\tan(q)}\sin(q\overline{\Gamma})\sin(q\Gamma) \\ & + \frac{1}{q}\cos(q\overline{\Gamma})\sin(q|\Gamma|) \ ,\end{aligned} \tag{136}$$

where

$$\mathrm{sgn}(\Gamma) = \begin{cases} -1, & \Gamma < 0 \\ 0, & \Gamma = 0 \\ 1, & \Gamma > 0 \ . \end{cases} \tag{137}$$

Equation 136 satisfies the boundary conditions and the transition conditions. Substitution of eq. 136 into eq. 125 yields the load-thrust

relationship,

$$A\xi^2 + B\xi + C = 0 \tag{138}$$

where A, B, and C are functions of the thrust, λ, and $\overline{\Gamma}$. (See Appendix A). The solution procedure for the offset loading follows that of the midspan loading case.

Eccentric Loading: q = 0

For the thrust parameter equal to zero, the governing equation is again altered. The resulting displacement solution is,

$$\phi(\Gamma) = \xi\{\frac{\Gamma^2}{4}(\overline{\Gamma} + \mathrm{sgn}(\Gamma)) - \frac{\Gamma}{2}(1 + \overline{\Gamma}\,\mathrm{sgn}(\Gamma))$$

$$+ \frac{(\overline{\Gamma})^3}{12} + \frac{(\overline{\Gamma})^2}{4}\mathrm{sgn}(\Gamma) + \frac{\overline{\Gamma}}{6}\} \ . \tag{139}$$

The loads for which the thrust is zero are given by the relationship,

$$\xi\{\xi - \frac{15}{4}[\frac{5 + 18(\overline{\Gamma})^2 + (\overline{\Gamma})^4}{3-7(\overline{\Gamma})^2 + 5(\overline{\Gamma})^4 - (\overline{\Gamma})^6}]\} = 0 \ , \tag{140}$$

which is obtained by substituting the functional form of the radial displacement into eq. 125.

Eccentric Loading, $q = \frac{n\pi}{2}$, n = 1, 2, 3, ...

With $q = \frac{n\pi}{2}$, n = 1, 2, 3, ... the adjoint problem outlined for the midspan loading must again be examined. The orthogonality condition

reveals that the applied loads for these values of thrust have the form,

$$p = \frac{n\pi \sin(\frac{n\pi}{2})}{\cos(\frac{n\pi\overline{\Gamma}}{2})\lambda^4} . \tag{141}$$

For odd values of $\frac{n\pi}{2}$ the radial displacement is,

$$\phi_n(\Gamma) = \frac{1}{2}(1 - \Gamma^2) + \frac{1}{q_n^2} - \frac{1}{q_n \sin(q_n)\cos(q_n\overline{\Gamma})}\{1 + \overline{\Gamma}\,\mathrm{sgn}(\Gamma)\}$$

$$+ \frac{\Gamma}{q_n \sin(q_n)\cos(q_n\overline{\Gamma})}\{\overline{\Gamma} + \mathrm{sgn}(\Gamma)\} + A_n^* \cos(q\Gamma) \tag{142}$$

$$- \frac{1}{q_n^2 \sin(q_n)} \sin(q_n|\Gamma|) ,$$

while for even values of $\frac{n\pi}{2}$ the displacement is given by,

$$\phi_n(\Gamma) = \frac{1}{2}(1 - \Gamma^2) + \frac{1}{q_n^2}\left(1 - \frac{\cos(q_n\Gamma)}{\cos(q_n)}\right) + A_n^* \sin(q_n\Gamma) . \tag{143}$$

The magnitude of A_n^* for both displacement functions is found from the expression,

$$A(A_n^*)^2 + BA_n^* + C = 0 , \tag{144}$$

where A, B, and C are constants which depend on the values of the thrust, λ, and $\overline{\Gamma}$ (See Appendix A for the functional forms of A, B, and C).

Typical Numerical Results - Midspan Loading

Shallow cylindrically curved panels exhibit a number of different deformation and buckling behaviors. The particular behavior depends on the parameter λ. Some of the effects of orthotropic material properties on the value of λ, and thus the behavior of curved panels, is explored in Appendix B. Generally, though, curved panels which have no eccentricity in the loading ($\overline{\Gamma} = 0$) exhibit three distinct behaviors. In this section each type of behavior will be discussed in order to familiarize the reader with typical analytic results. These discussions will focus on the behavior under displacement control and load control. However, the condition represented by the experimental setup to be described is displacement control.

If λ is sufficiently small the load-displacement behavior is monotonic and no snap-buckling occurs. In fig. 5 typical load-thrust, p vs. q, and load-midspan displacement, p vs. $\overline{\phi}$, diagrams are shown for a panel which exhibits monotonic behavior. Here $\overline{\phi}$ denotes the nondimensional radial displacement at the location of the applied load. As the load and displacement increase from zero through points 1 and 2, the stiffness ($dp/d\overline{\phi}$) of the panel decreases while the thrust increases. At point 3 the thrust is a maximum and the stiffness is a minimum. A further increase in load or displacement through points 4 and 5, depending on which variable is controlled, causes the thrust to decrease and the stiffness to increase. Finally at point 6, a point close to the fully inverted configuration, the thrust is approaching zero. In fig. 6 the equilibrium configurations corresponding to the

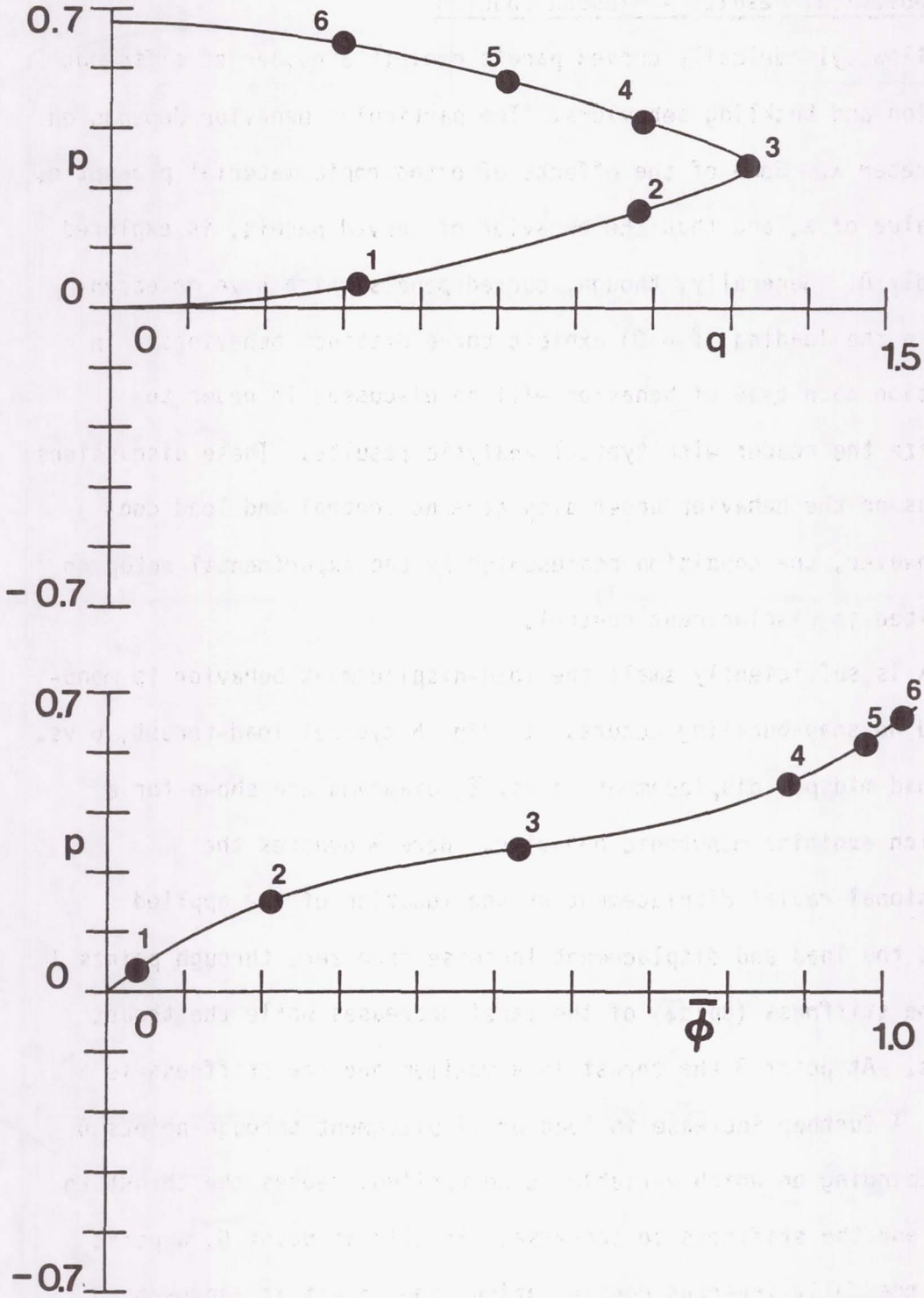

FIG. 5 LOAD-THRUST AND LOAD-DISPLACEMENT RELATIONS, λ =1.75, $\bar{\Gamma}$ =0.0

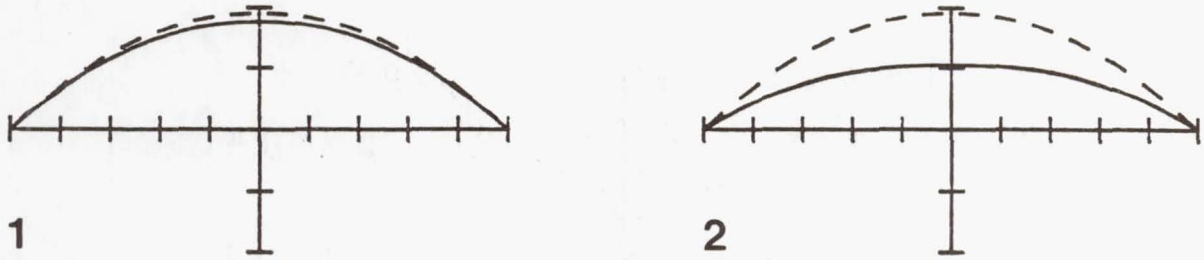

NOTE: NUMBERS CORRESPOND TO POINTS ON FIG. 5

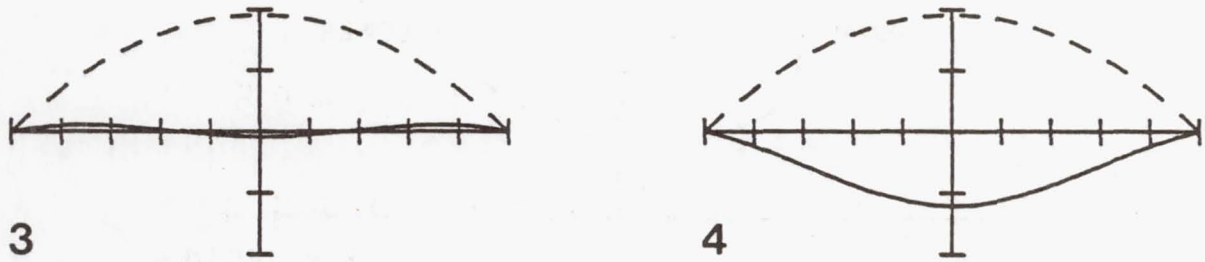

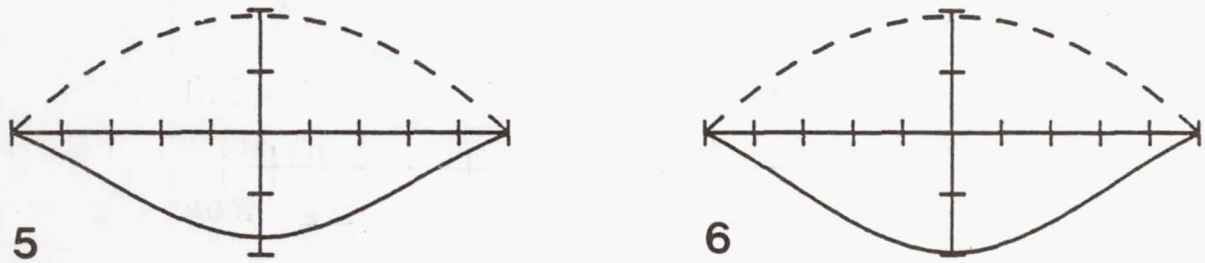

FIG. 6 EQUILIBRIUM CONFIGURATIONS, λ=1.75, $\bar{\Gamma}$=0.0

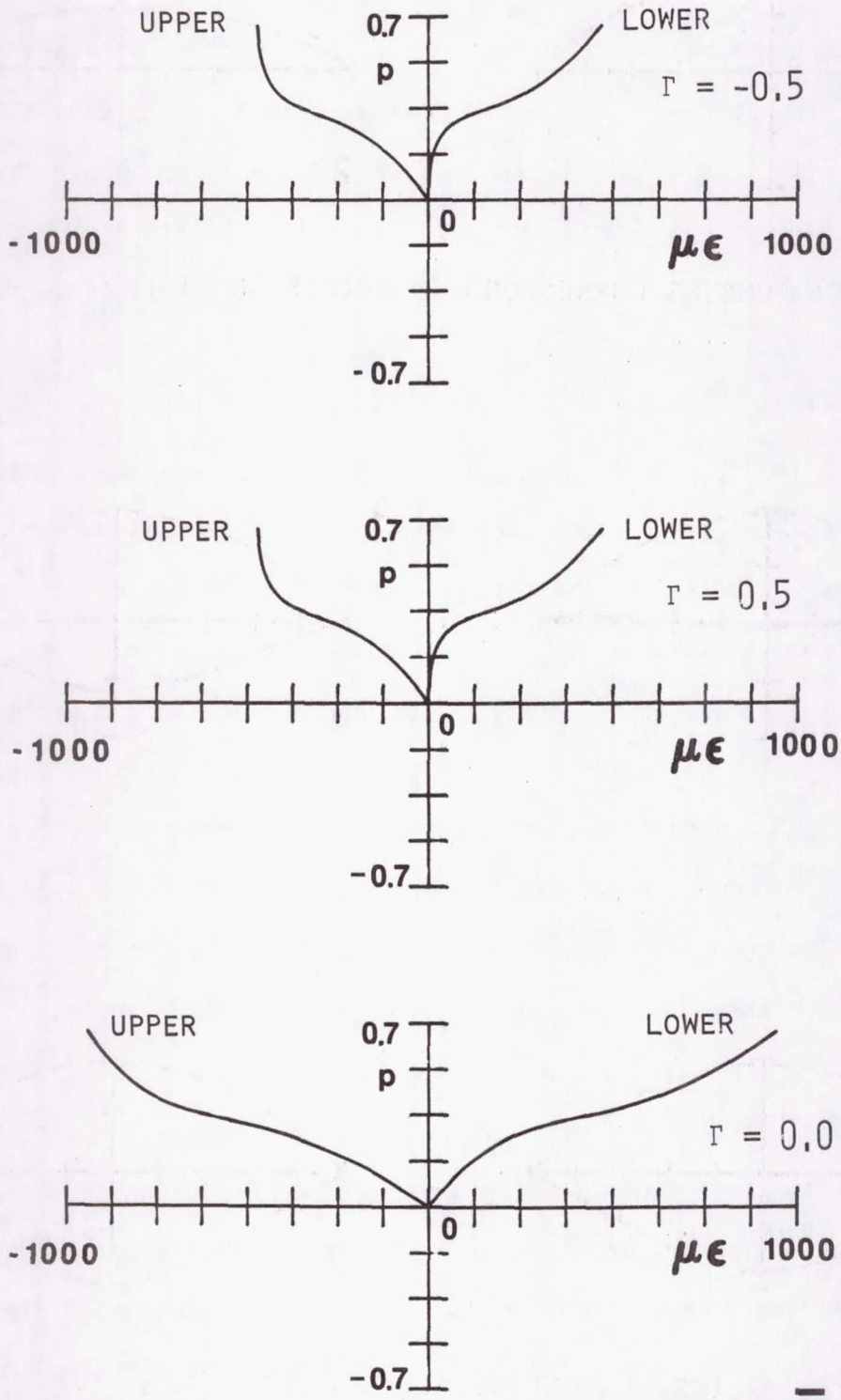

FIG. 7 SURFACE STRAINS VS. APPLIED LOAD, λ=1.75, $\bar{\Gamma}$=0.0

points denoted on the load-thrust and load-displacement are shown. Figure 7 shows the behavior of the upper and lower surface strains, i.e., $z = +\frac{h}{2}$ and $z = -\frac{h}{2}$, at the two quarter points ($\Gamma = \pm 0.5$) and midspan ($\Gamma = 0.0$) , as a function of the applied load. Obviously due to symmetry of the response, the strains at the quarter points are identical. This panel exhibits no instability, a characteristic which is typical of panels with $\lambda < 1.9762$.

A second type of behavior is known as limit point behavior. This is depicted in fig. 8. As the load, or displacement, is increased from zero through point 1, the thrust increases and the stiffness decreases. At point 2 the load-thrust curve has a horizontal tangent and the stiffness of the panel is zero. At point 2 a relative maximum load, or limit point, is reached on the equilibrium path. Under load control this is a critical equilibrium configuration and increasing the load results in a sudden dynamic snap-through to a equilibrium configuration between points 5 and 6. Under displacement control this point is stable. Increasing the displacement past point 2 will cause the load to decrease and the thrust to continue to increase. Point 3 denotes the maximum thrust for the panel. Increasing the displacement from point 3 to point 4 causes both the thrust and the load to decrease. Notice that point 4 is also a load limit point. From point 4 through point 5 the load increases while the thrust decreases to zero with increasing displacement. Figure 9 shows the equilibrium configurations, under displacement control, for various values of load and thrust. Figure 10 illustrates the strain behavior at the two quarter points and at mid-

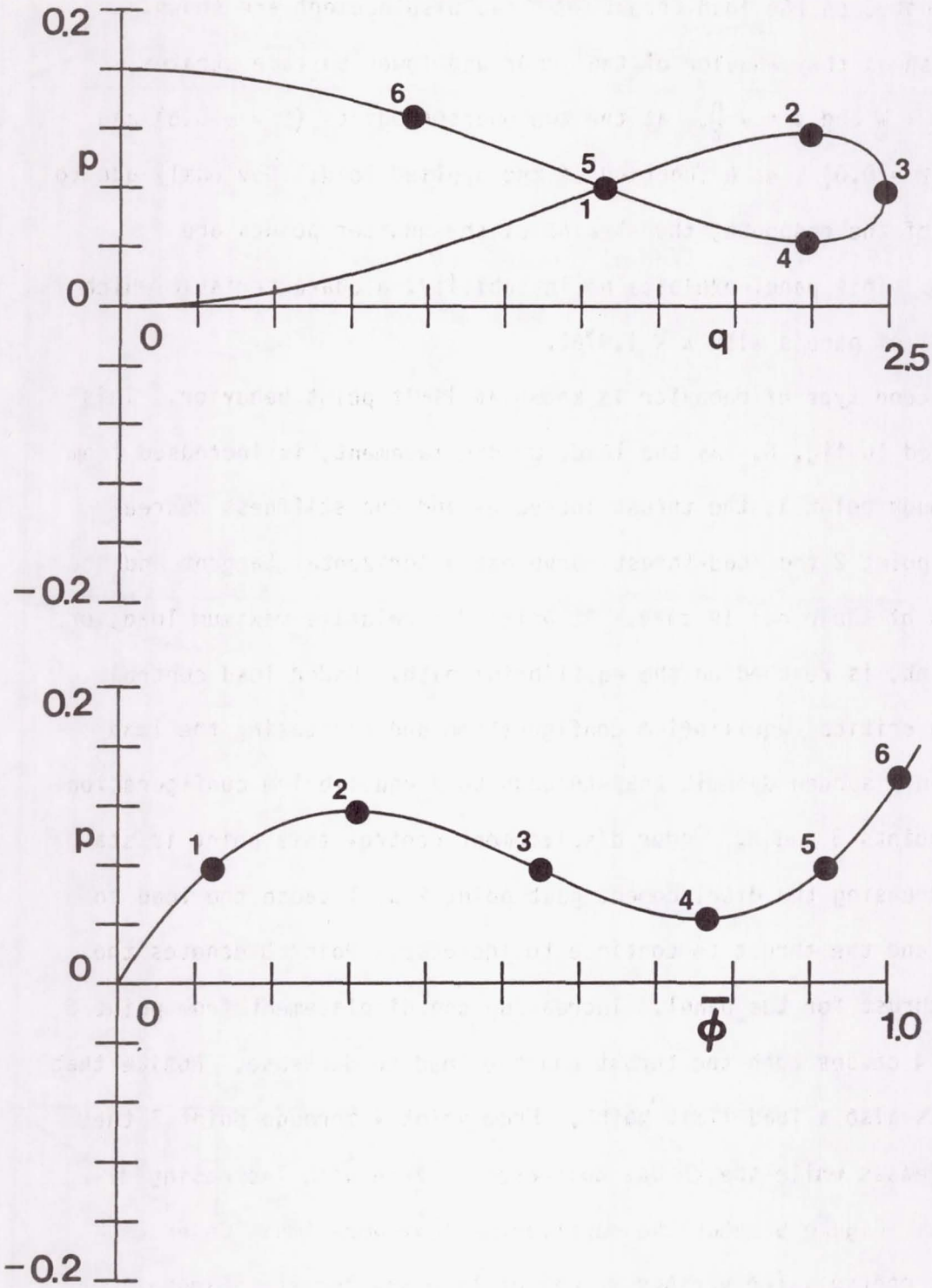

FIG. 8 LOAD-THRUST AND LOAD-DISPLACEMENT RELATIONS, λ =2.5, $\bar{\Gamma}$ =0.0

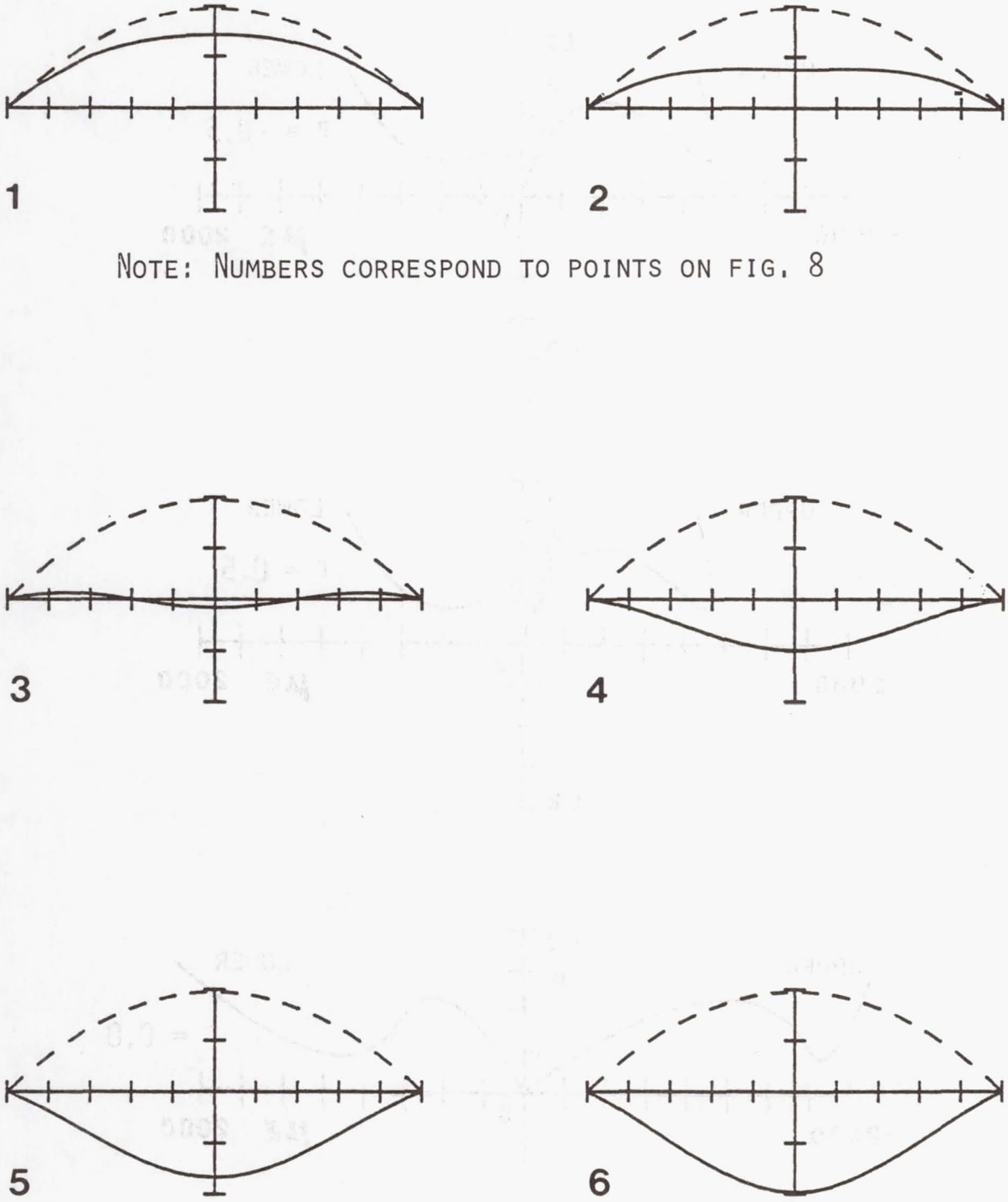

NOTE: NUMBERS CORRESPOND TO POINTS ON FIG. 8

FIG. 9 EQUILIBRIUM CONFIGURATIONS, λ =2.5, $\overline{\Gamma}$ =0.0

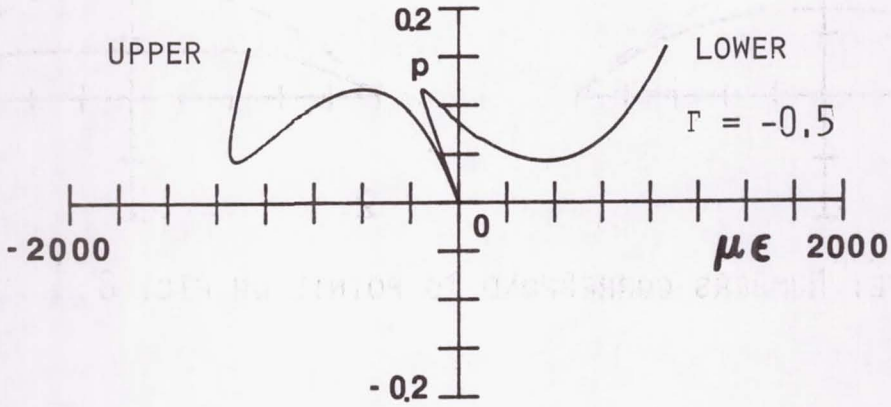

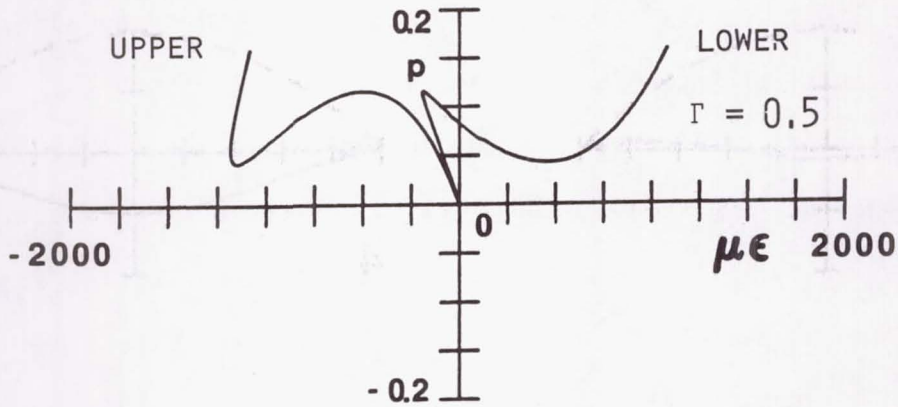

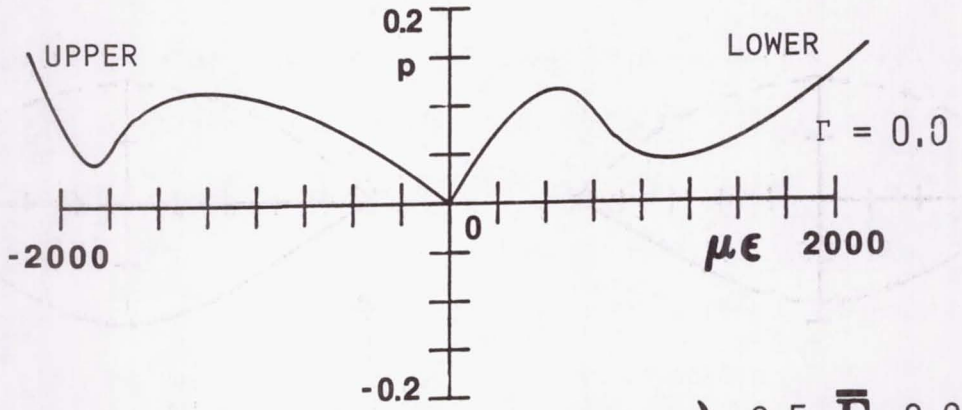

FIG. 10 SURFACE STRAINS VS. APPLIED LOAD, $\lambda = 2.5$, $\bar{\Gamma} = 0.0$

span. Under displacement control this panel exhibits no instability. Under load control there is the snap-through instability at point 2, the limit point, which is considered the buckling load. Limit point behavior is found for $1.9762 < \lambda < 2.825$.

The final type of behavior possible for the panel with no load eccentricity is known as bifurcation behavior. Bifurcation occurs on the initial loading path when the maximum thrust equals π. Figure 11 shows typical load-thrust and load-displacement diagrams for bifurcation behavior. Load, displacement, and thrust all increase from no-load through point 1 to point 2. At point 2 a secondary equilibrium path, the straight line through points 2, 3, and 4, intersects the primary path. This secondary path represents the asymmetric response mentioned in Chapter 2 and included in eq. 127. (Actually there are two equilibrium paths associated with asymmetric configurations intersecting at point 2 since two values of the amplitude b, eq. 130, are determined for each value of the load.) Point 2 is called a bifurcation point. In load control both the primary equilibrium path, beyond point 2, and the secondary equilibrium path configurations are unstable. Thus the panel will dynamically snap-through at the bifurcation point to a configuration on the primary path beyond point 6. Point 2 is considered the buckling load. In displacement control the secondary path is stable while the primary path becomes unstable. Increasing the displacement causes the load to decrease, along the straight line between points 2, 3, and 4, and the thrust to remain constant. Note the load actually drops to zero at point 3. The spatial configuration of the panel

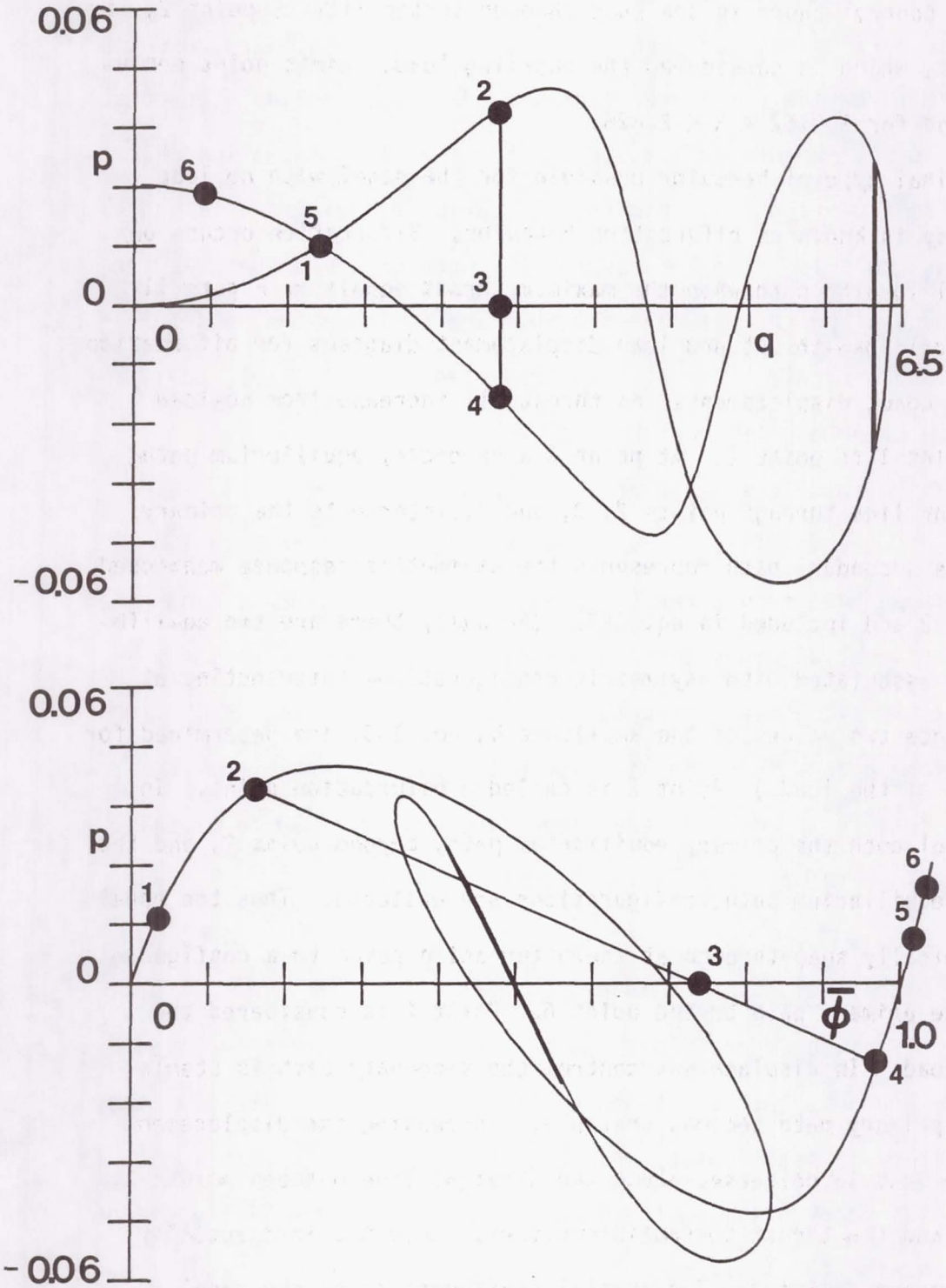

FIG. 11 LOAD-THRUST AND LOAD-DISPLACEMENT RELATIONS, λ =4.0, $\bar{\Gamma}$ =0.0

corresponding to points along the secondary path is asymmetric while the primary path corresponds to symmetric deformation. Point 4 represents the second bifurcation point where the secondary path again intersects the primary path. Figure 12 illustrates the spatial deformation characteristics for a panel which exhibits bifurcation behavior and is under displacement control. Note the asymmetry in the deformed shape as the response moves along the bifurcated path. The surface strains shown in fig. 13 illustrate only those strains predicted for the stable equilibrium path under displacement control.

Bifurcated solutions exist at all values of $q = n\pi$, $n = 1, 2, 3, \ldots n_{max}$, but only the first bifurcated path ($n = 1$) represents the physically important result for the static response. It should be noted here that bifurcation behavior is a mathematical result of an analysis for a perfectly symmetrical structure. Since, in practice, real structures are not perfect this idealization will never be achieved. However, with relatively small initial imperfections it could be closely approximated. Bifurcation behavior occurs for $\lambda > 2.825$.

Typical Numerical Results - Eccentric Loading

When offsets, or eccentricities, in the location of the applied loading are present, only two types of behavior exist. These are monotonic behavior and limit point behavior. Panels which exhibit monotonic or limit point behaviors when the load is at midspan show little change in their behavior for small eccentricities in the loading. Figures 14-16 show the monotonic response of a panel with geometric and material

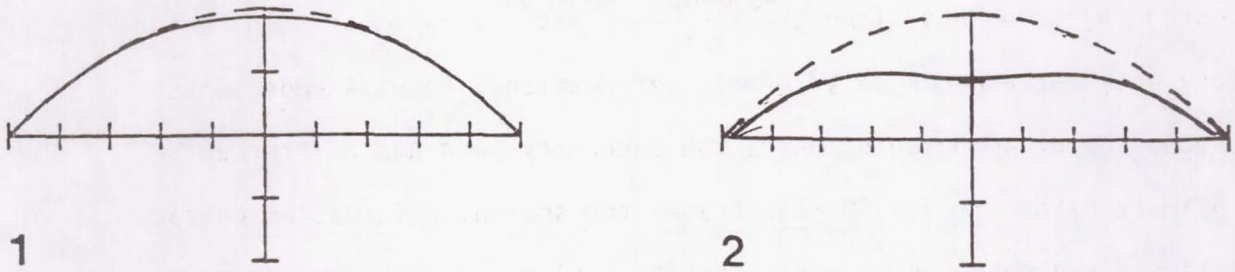

NOTE: NUMBERS CORRESPOND TO POINTS ON FIG. 11

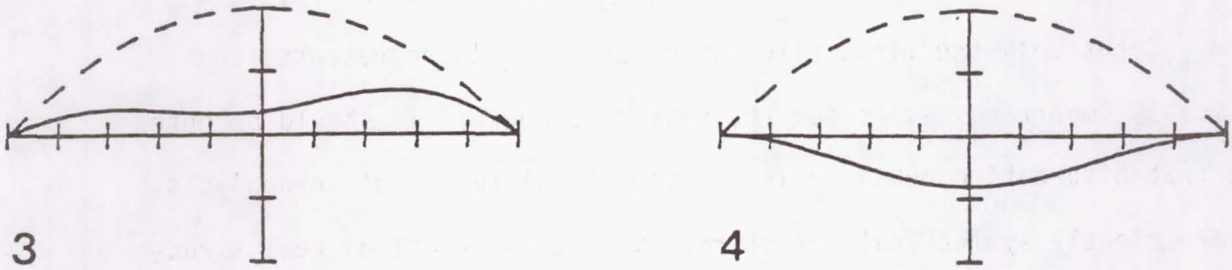

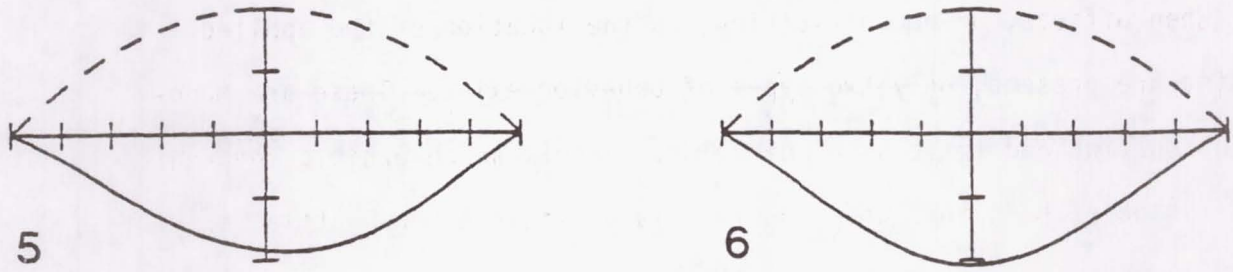

FIG. 12 EQUILIBRIUM CONFIGURATIONS, $\lambda = 4.0$, $\bar{\Gamma} = 0.0$.

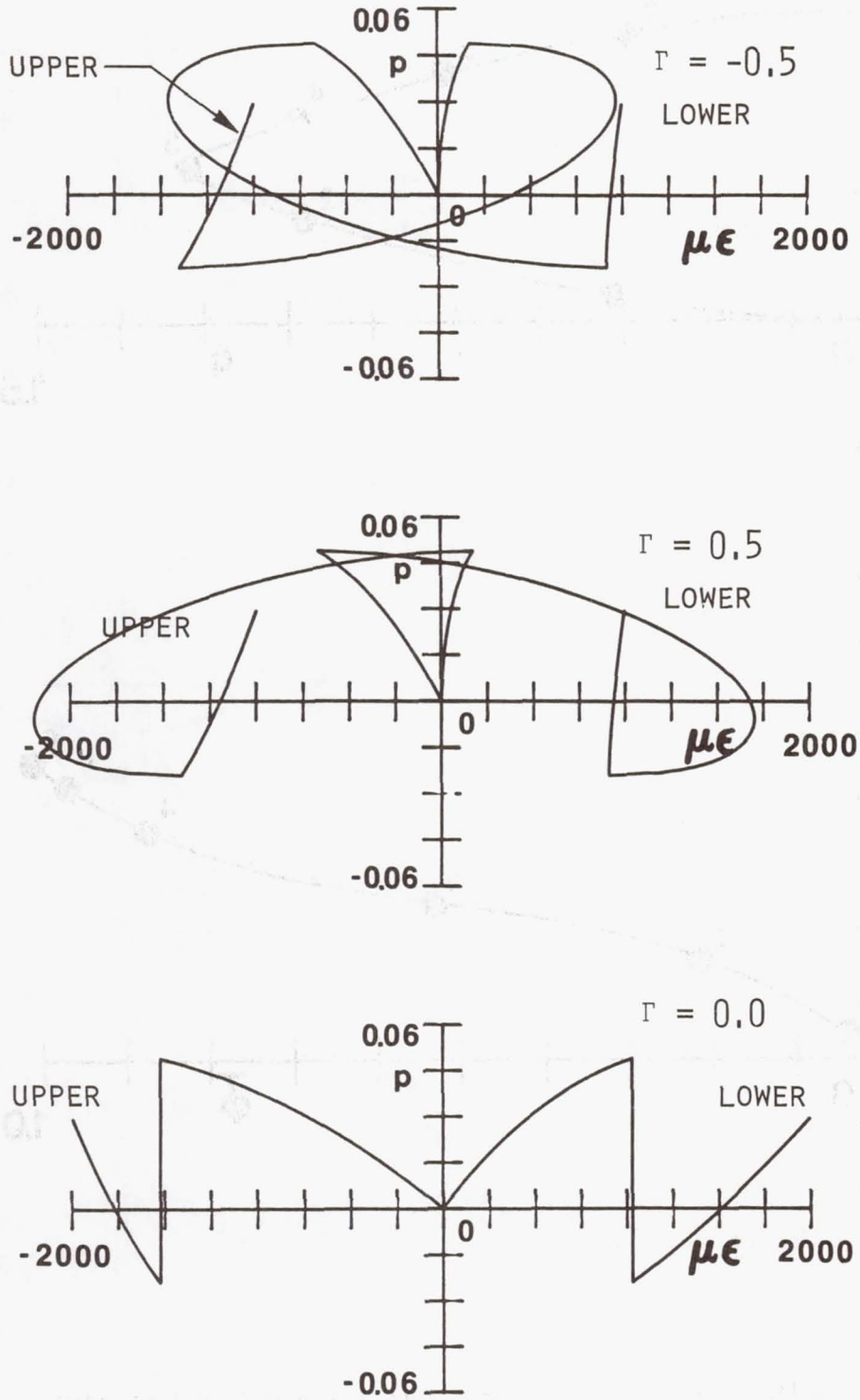

FIG. 13 SURFACE STRAINS VS. APPLIED LOAD, λ =4.0, $\overline{\Gamma}$ =0.0

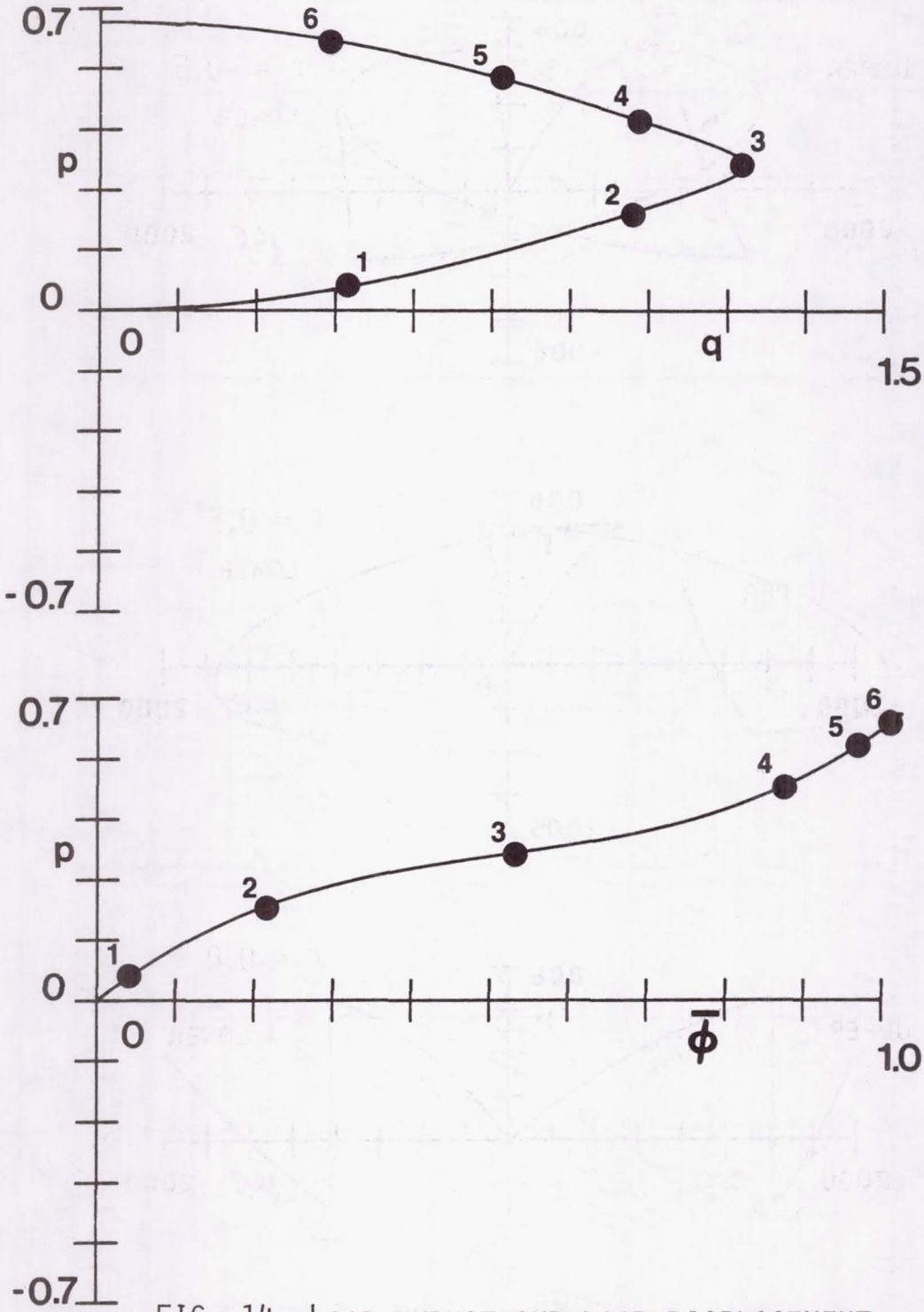

FIG. 14 LOAD-THRUST AND LOAD-DISPLACEMENT RELATIONS, λ=1.75, $\bar{\Gamma}$=0.1

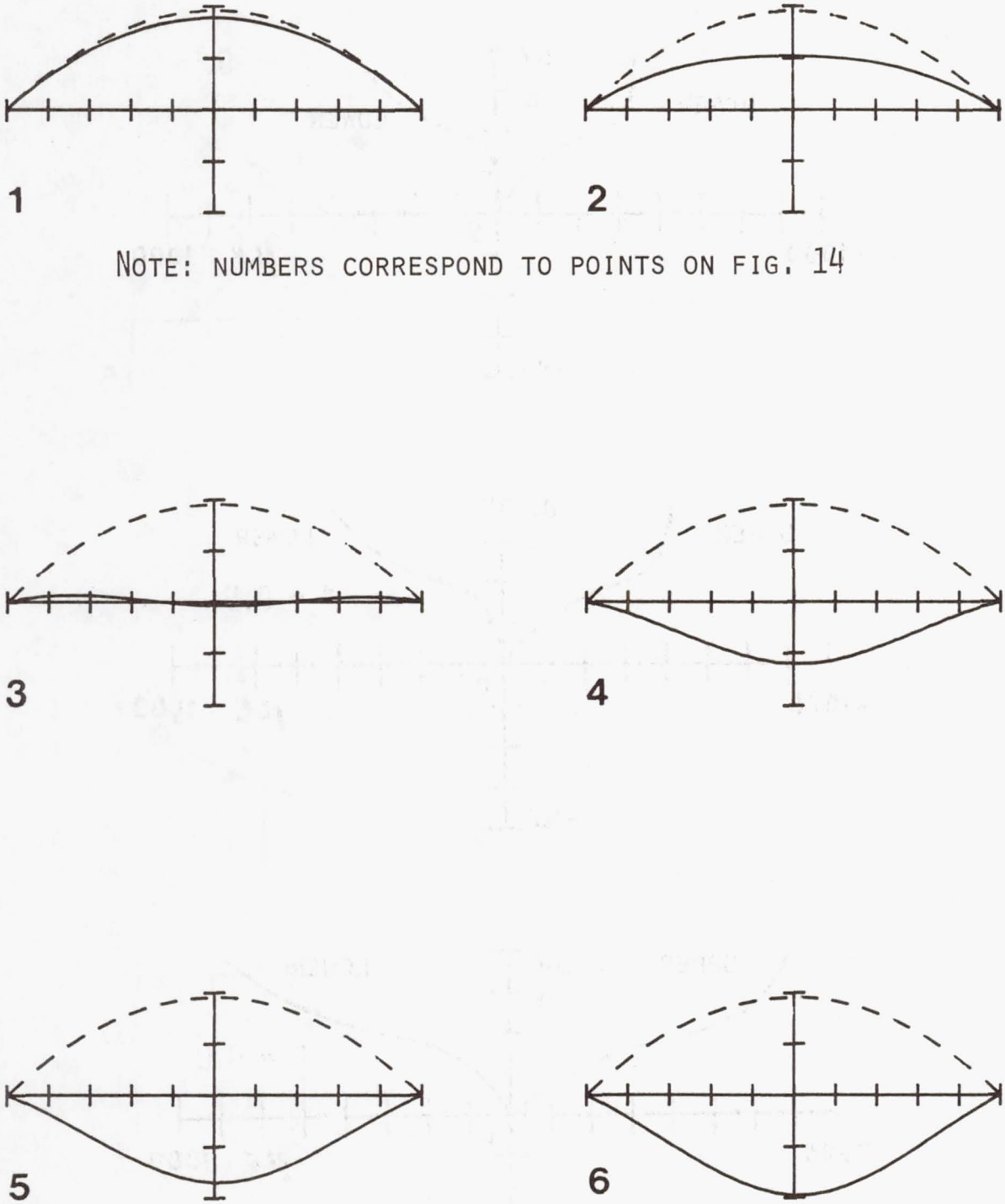

NOTE: NUMBERS CORRESPOND TO POINTS ON FIG. 14

FIG. 15 EQUILIBRIUM CONFIGURATIONS, λ =1.75, $\bar{\Gamma}$ =0.1

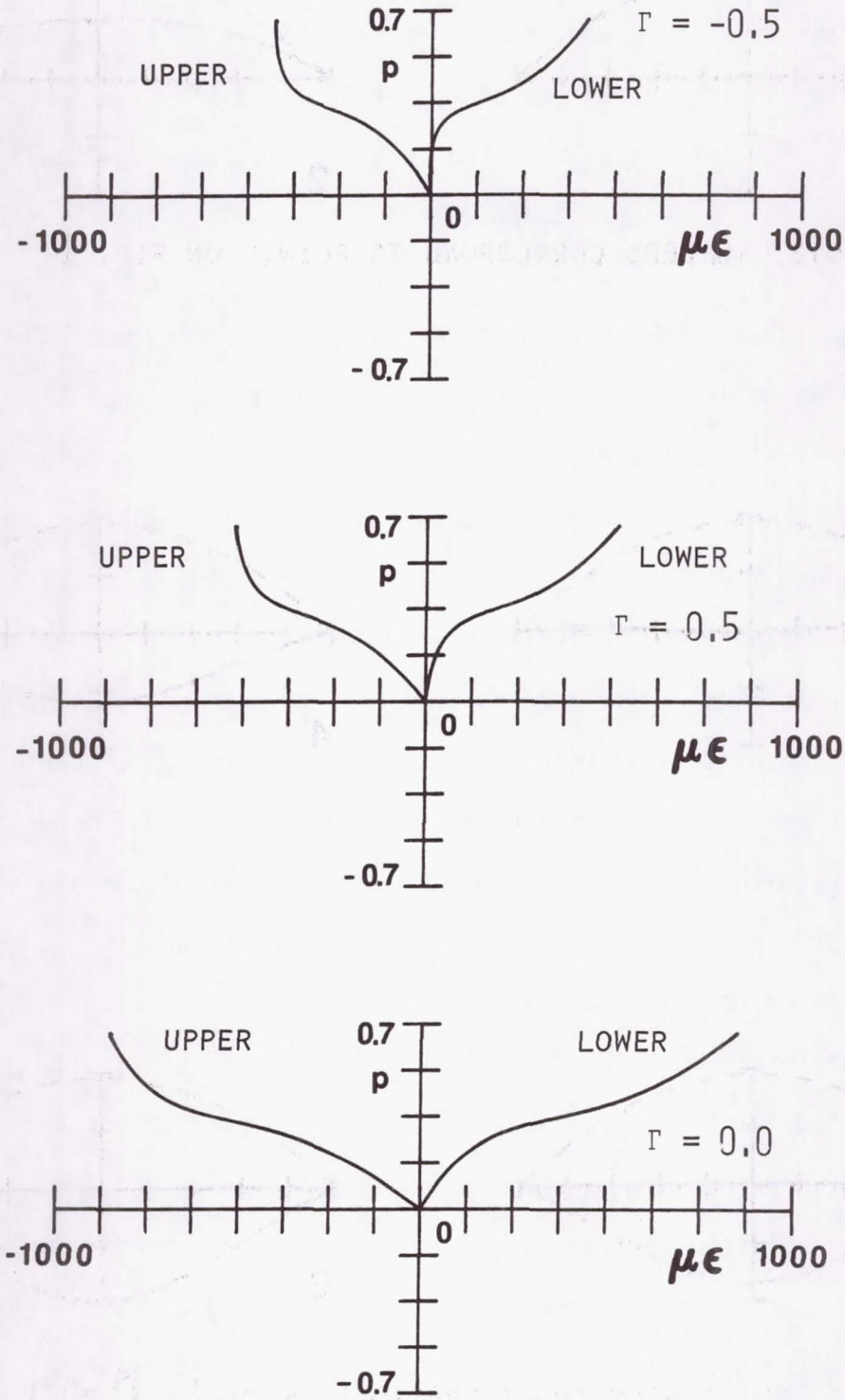

FIG. 16 SURFACE STRAINS VS. APPLIED LOAD, λ =1.75, $\overline{\Gamma}$ =0.1

properties identical to the panel of figs. 5-7, with the exception of a 10% offset in the load being present. Here the load is offset to the right. The only significant effect of the offset is a slight asymmetry in the deformation. This is illustrated by the equilibrium configurations shown in fig. 15. Figure 16 shows the surface strain behavior for this loading case.

Figures 17-19 show the effects of load offset on a panel which exhibits limit point behavior when the load is exactly at midspan. Again the only significant effect is a slight asymmetry in the deformation. A comparison of figs. 8 and 17 shows that the offset leaves the limit load essentially unchanged.

A panel which exhibits instability at bifurcation points when the load is exactly at midspan is affected to a much greater degree by eccentricities in the load position. This is easily seen by comparing the load-thrust and load-displacement diagrams of fig. 11, the case of midspan loading, with those of fig. 20. Following the equilibrium path shown in fig. 20, an increase in the displacement causes the thrust and load to increase up to point 2. Here point 2 represents a load limit point (horizontal tangent). For the midspan loading case, fig. 11, point 2 was not a limit point. It was a bifurcation point. For the offset loading, any increase in the applied load beyond point 2 would cause loss of stability. On the other hand, controlling the displacement from point 2 to point 4 causes the load to decrease and the thrust to continue increasing. At point 4, $q > \pi$. Thus for load offsets $q = \pi$ is no longer the limiting value of thrust for the stable equilibrium

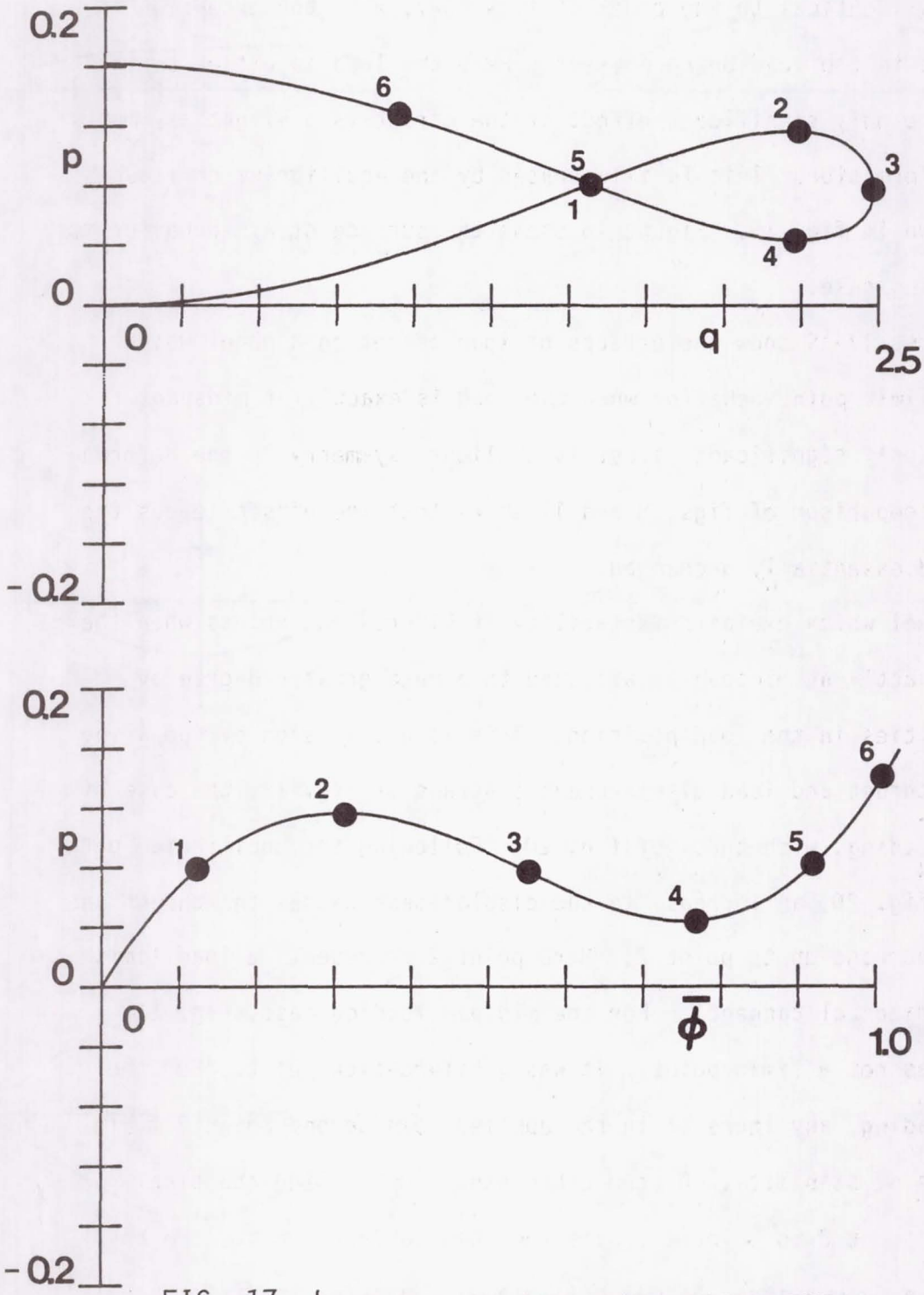

FIG. 17 LOAD-THRUST AND LOAD-DISPLACEMENT RELATIONS, λ =2.5, $\bar{\Gamma}$ =0.1

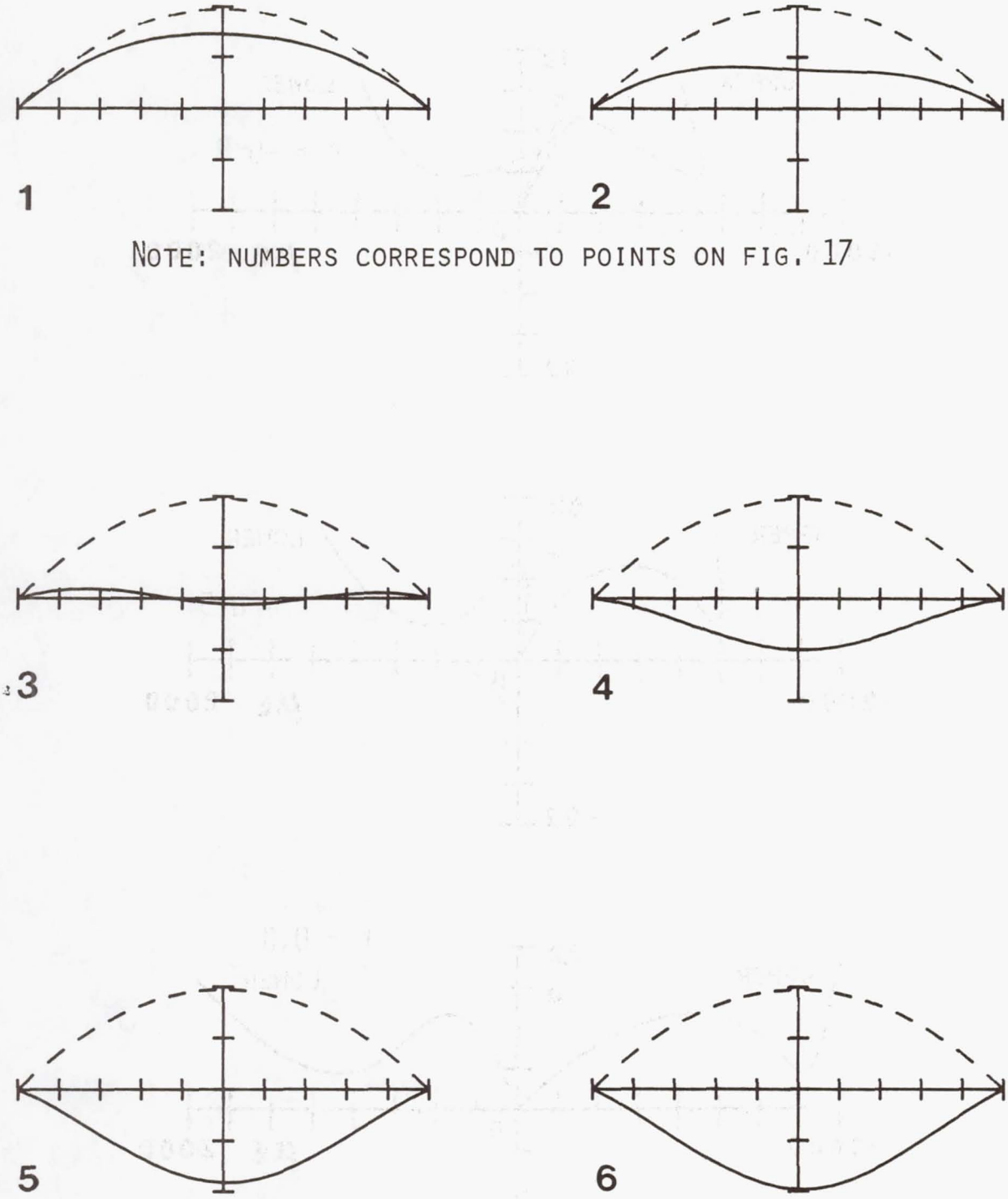

NOTE: NUMBERS CORRESPOND TO POINTS ON FIG. 17

FIG. 18 EQUILIBRIUM CONFIGURATIONS, λ=2.5, $\bar{\Gamma}$=0.1

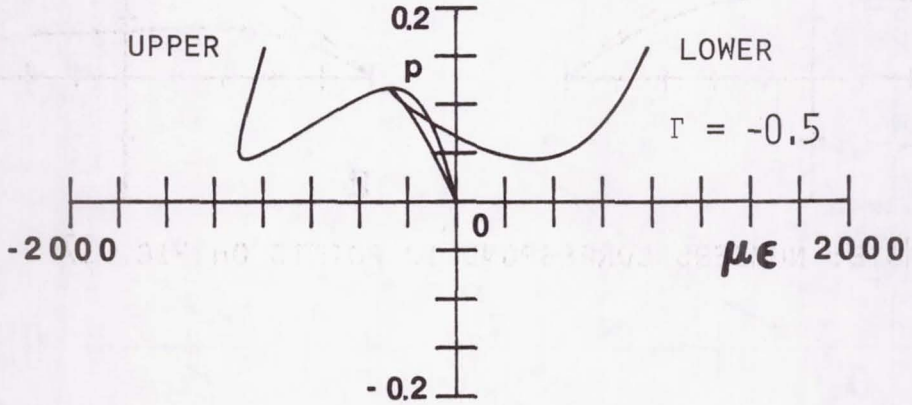

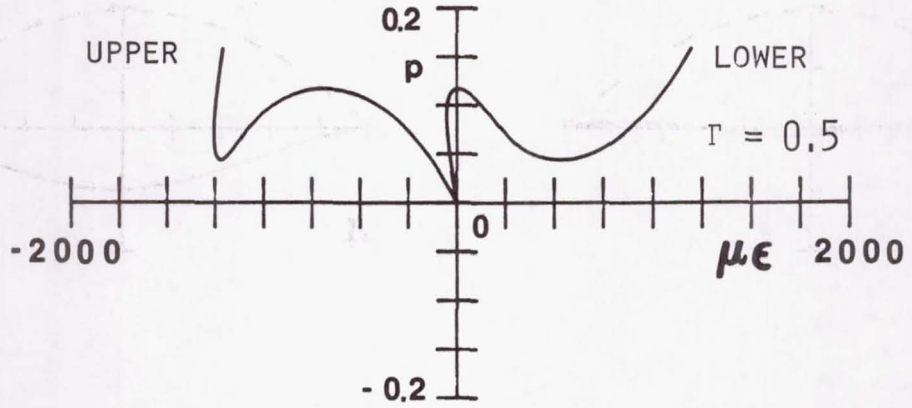

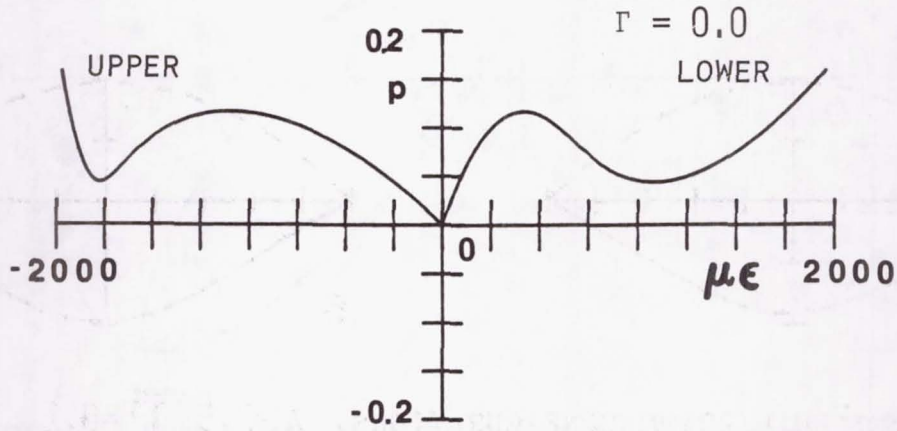

FIG. 19 SURFACE STRAINS VS. APPLIED LOAD, λ =2.5, $\overline{\Gamma}$ =0.1

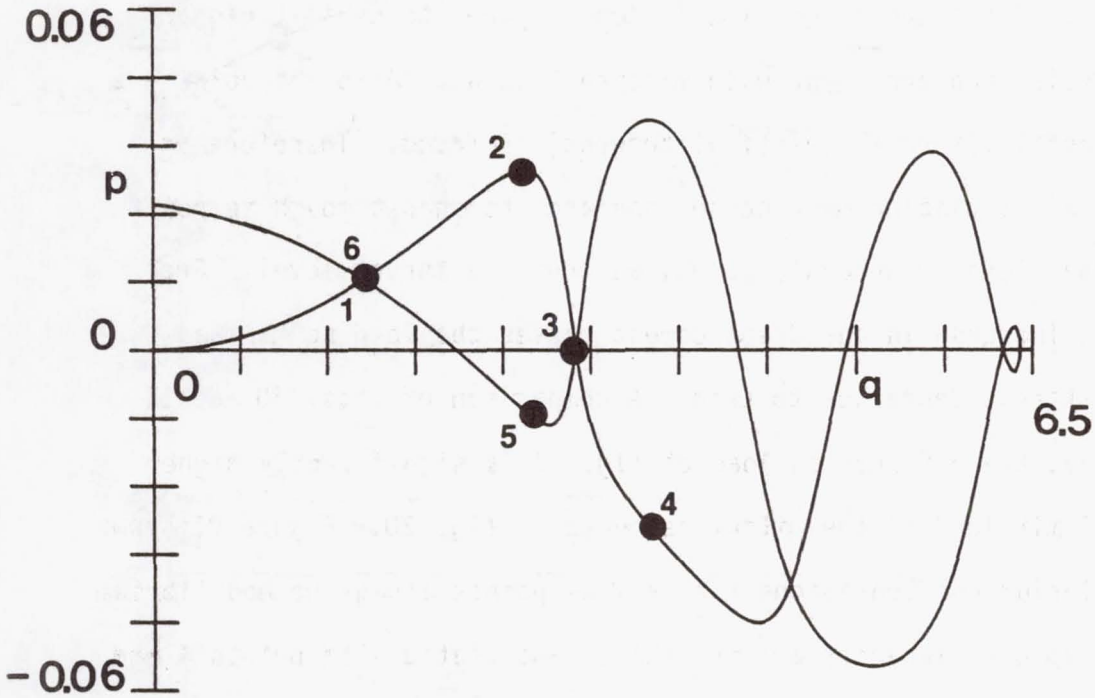

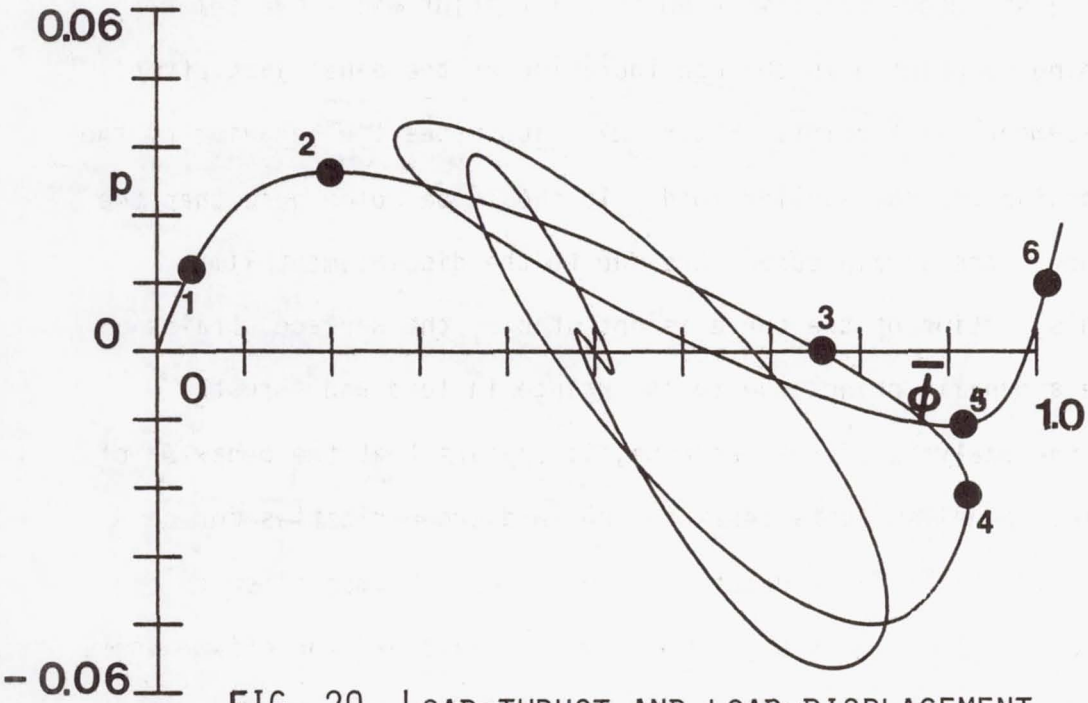

FIG. 20 LOAD-THRUST AND LOAD-DISPLACEMENT RELATIONS, λ =4.0, $\bar{\Gamma}$ =0.1

path. Recall from fig. 11, $q = \pi$ was the limiting value for the midspan case. This allows the eccentrically loaded panel to exhibit higher strain levels than are found with midspan loading. Also, at point 4 a displacement limit point (vertical tangent) is found. Therefore an increase in the displacement causes the arch to snap-through to point 5. The load level p suddenly jumps, as does the thrust level. From point 5 an increase in the displacement causes the load to increase while the thrust decreases to zero. A comparison of figs. 20 and 11 reveals that the bifurcation load of fig. 11 is significantly higher than the limit load of the offset response in fig. 20. Figure 21 shows the equilibrium configurations for various points along the equilibrium path. Of special interest are the shapes associated with points 4 and 5. The shape corresponding to point 4 represents the equilibrium configuration just before the displacement limit point while the shape corresponding to point 5 is the configuration of the panel just after the displacement limit point. Figure 22 illustrates the behavior of the surface strains vs. the applied load. It should be noted here that the sharp jumps in the strain curves are due to the displacement limit point. This portion of the curve is not stable, the surface strains experience a dynamic change due to the change in load and thrust.

From the analysis of the response, it appears that the behavior of a cylindrical panel is quite sensitive to load eccentricities for certain ranges of λ. To fully understand the effect of load offsets, the relation between the magnitude of the buckling load and the offset angle is examined. Since the problem is physically symmetric with respect to

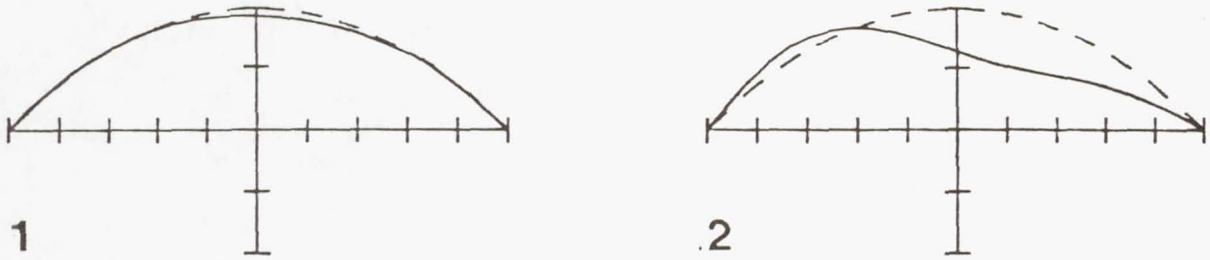

NOTE: NUMBERS CORRESPOND TO POINTS ON FIG. 20

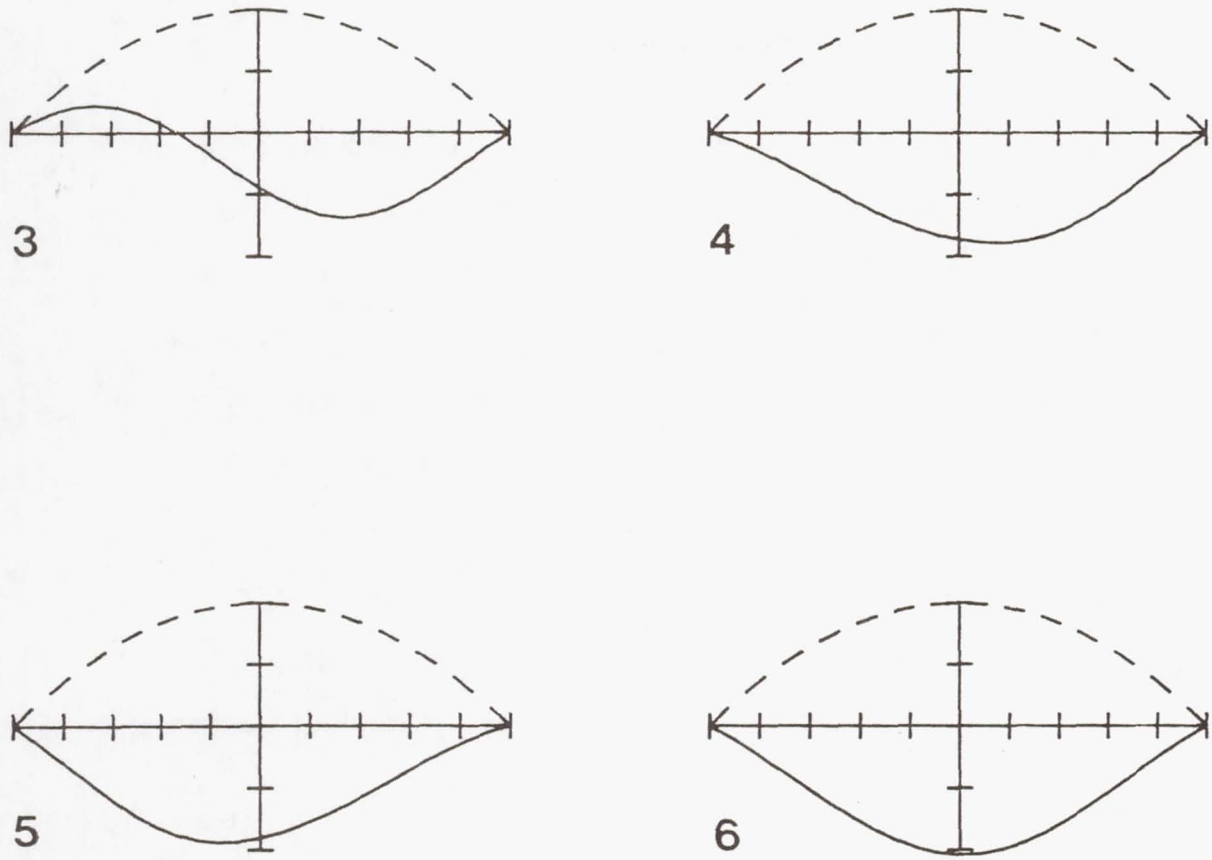

FIG. 21 EQUILIBRIUM CONFIGURATIONS, λ =4.0, $\overline{\Gamma}$ =0.1

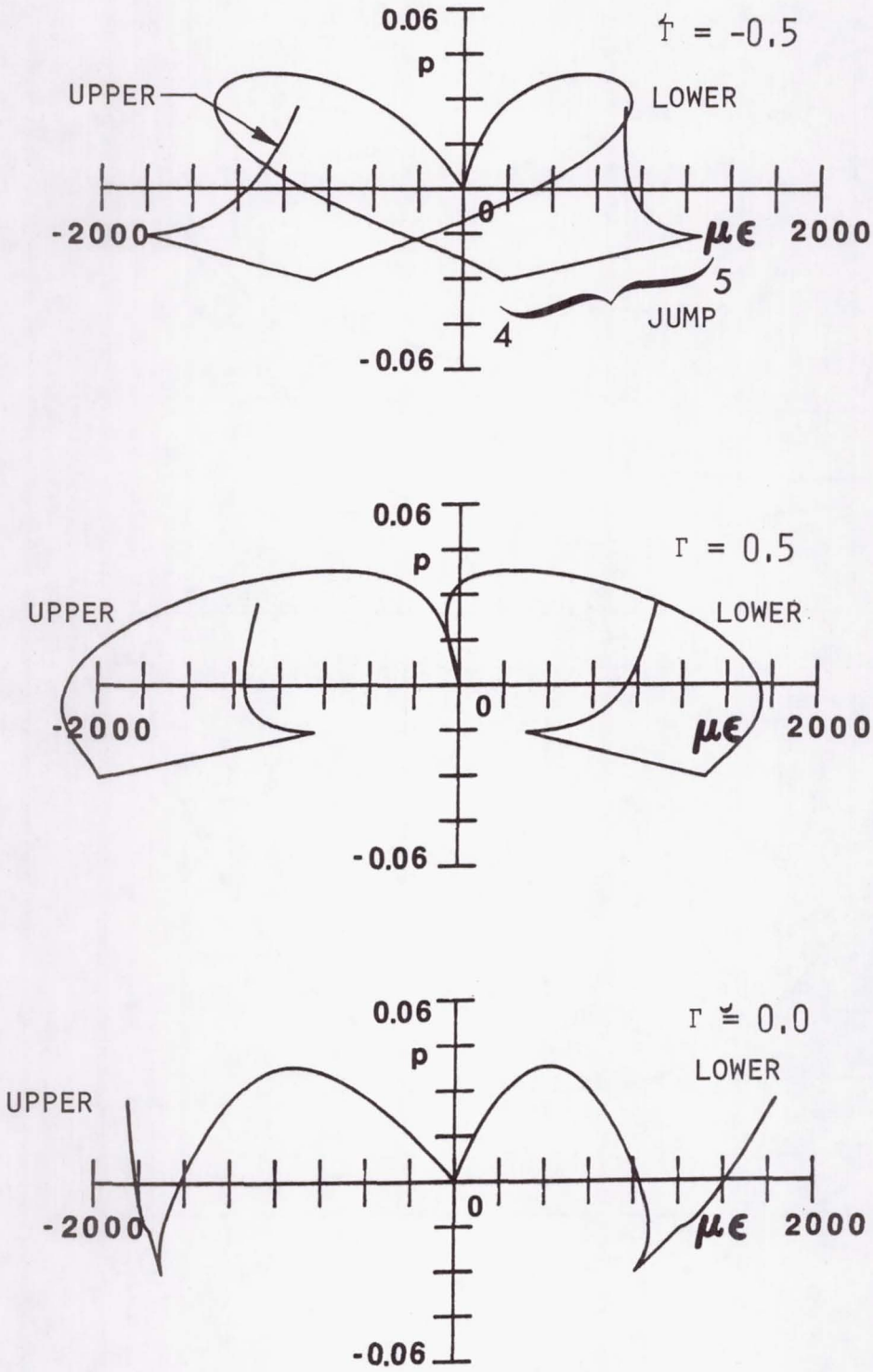

FIG. 22 SURFACE STRAINS VS. APPLIED LOAD, λ =4.0, $\bar{\Gamma}$ =0.1

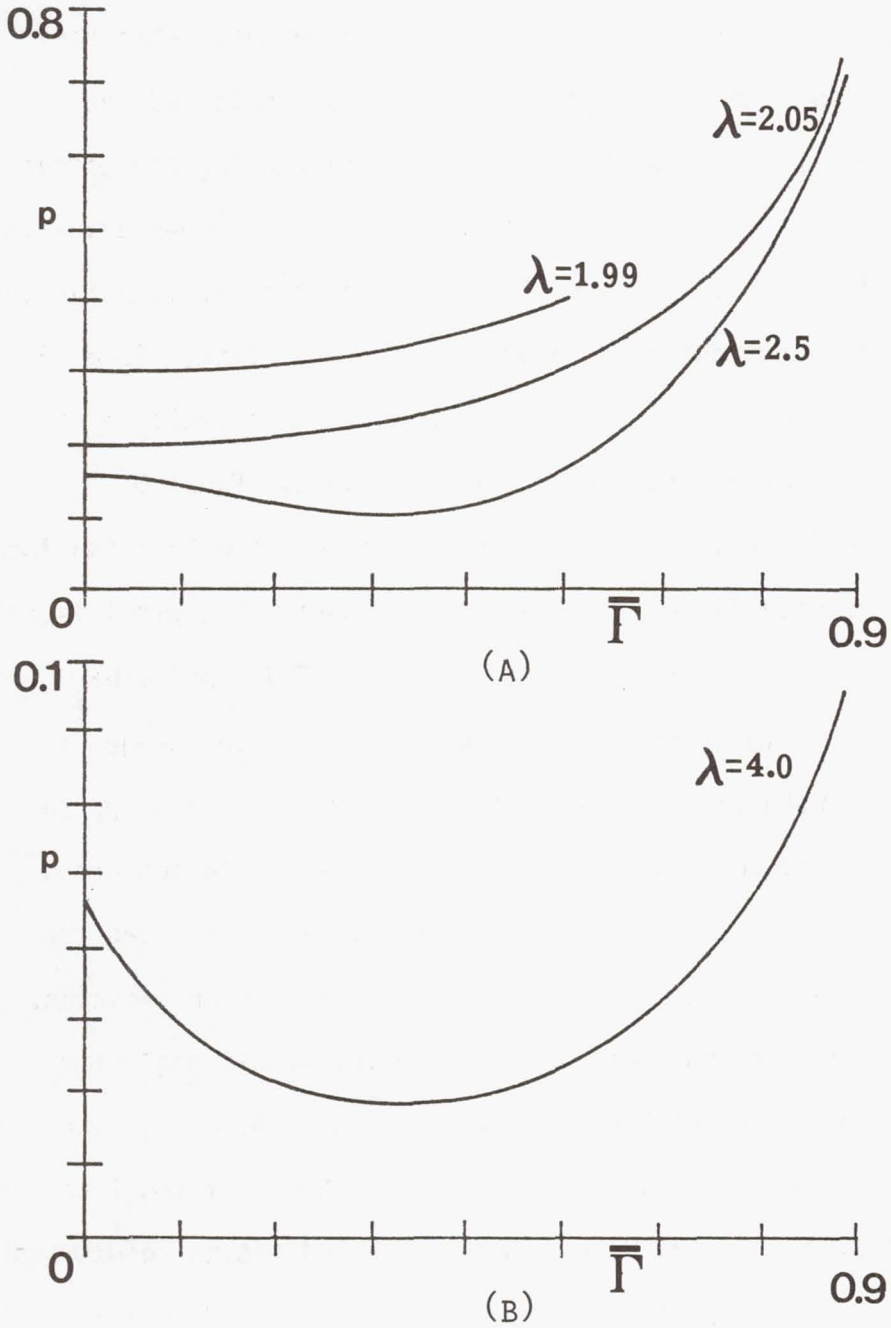

FIG. 23 SENSITIVITY OF BUCKLING LOAD TO LOAD ECCENTRICITY

the midspan vertical, only positive load offsets are shown. Figure 23a shows the effect of load eccentricity on the buckling load for three different panels, all of which exhibit limit point behavior when the load is exactly at midspan. Here the limit load is considered the buckling load. For panel 1, which has $\lambda = 1.99$, increasing the offset angle causes only slight increases in the buckling load. However, with this panel, an offset causes the behavior to switch from limit point to monotonic behavior. Thus there no longer is an instability. Panel 2, with $\lambda = 2.05$, resembles panel 1 with the exception that limit point behavior applies for the entire range of load offsets. Panel 3, where $\lambda = 2.5$, is different than the first two in that the buckling load initially decreases with increasing load offset. Still the panel is not overly sensitive to eccentricities in the loading. Small perturbations ($\overline{\Gamma} \approx 0.1$) in the load position only cause negligible changes in the buckling load. Both panels 2 and 3 exhibit buckling loads approaching infinity as the applied load is moved very close to the supports.

A panel which exhibits bifurcation instability when the load is exactly at midspan tends to be quite sensitive to load eccentricities. Figure 23b shows the buckling load as a function of offset angle for such a panel. The bifurcation load corresponds to the buckling load for $\overline{\Gamma} = 0$, and the limit point load corresponds to the buckling load for all other load offsets. The buckling load shows significant reductions even for small load offsets. This type of behavior leads to the panel being considered imperfection-sensitive.

Chapter 4

EXPERIMENTAL SET-UP AND PROCEDURE

Little experimental work has been performed in the area of the large, out-of-plane deformation behavior of shallow composite cylinders. The work that has been presented tends to be somewhat limited in scope in that the range of geometry is small or the effects of load eccentricities have not been investigated. To check the validity of the analysis just presented, a series of tests on composite specimens of varying geometries and load offsets were performed. These tests were to determine if all the behavioral characteristics predicted by the analysis are observable. Also, the effectiveness of the solution procedure, as well as classical lamination theory, in determining the large deformation response of composite structures was to be verified.

In order to make a comparison of the analytic and experimental results, the conditions of the experiment needed to closely approximate those used for the analysis. This required the test specimen to be supported such that the ends remained free of rotational constraints while the span between supports was kept constant. Also the load needed to act radially at the panel middle surface. To meet these requirements, as well as others, a test fixture and test procedure were designed to facilitate a fair comparison of theory and experiment.

Curved Panel Specimens

The test specimens were fabricated by NASA-Langley using AS4/3502 graphite-epoxy pre-preg. Table 1 shows the specified geometry and

Table 1

Intended Test Specimen Geometry

Specimen Number	Lay up	Thickness (in.)	Load Offset (%)
1	$[(90/0)_4]_s$	0.08	0
2	$[(90/0)_4]_s$	0.08	15
3	$[(90/0)_4]_s$	0.08	30
4	$[(90/0)_4]_s$	0.08	50
5	$[(90/0)_3]_s$	0.06	0
6	$[(90/0)_3]_s$	0.06	15
7	$[(90/0)_3]_s$	0.06	30
8	$[(90/0)_3]_s$	0.06	50
9	$[90/45/0/-45]_s$	0.04	15
10	$[90/45/0/-45]_s$	0.04	30
11	$[90/45/0/-45]_s$	0.04	50
12	$[(90/0)_4]_s$	0.08	0
13	$[(90/0)_4]_s$	0.08	15
14	$[(90/0)_4]_s$	0.08	30
15	$[(90/0)]_s$	0.02	0
16	$[(90/0)]_s$	0.02	15
17	$[(90/0)]_s$	0.02	30
18	$[(90/0)]_s$	0.02	50

Note: For all cases the intended radius was 60 in. with an arc length of 12 in., with the exception of specimens 12-14, where the arc length was 6 in.

stacking sequence for each specimen tested. For each geometry which was to be tested, a large 18 x 24 in. curved panel was fabricated using existing curved forms. After curing, each large panel was ultrasonically C-scanned to determine if any irregularities were present. For each large panel the results of the C-scan showed uniformity in the transmittance of sound waves, suggesting a uniformity of the material. Upon determining the quality of the panels, the specimens were then machined from the larger panels. Each specimen had a set of three holes drilled at the point of load application. This will be discussed shortly. By keeping a tight tolerance on the arc-wise location of the holes, it was possible to control the amount of load eccentricity. After machining, slotted dowels 0.375 in. in diameter, to be further discussed in connection with the test fixture, were attached to each end of the specimens. Figure 24 shows 6 in. arc length and 12 in. arc length panels both with and without the dowels attached. Two dowels are shown in fig. 24, as are two larger dowels which will be discussed. Strain gaging has been attached to the panels in fig. 24 and a 6 in. rule is visible in the photograph.

Test Fixture

Figure 25 shows a schematic of the test fixture while fig. 26 shows a photograph of the fixture. The major components of the fixture are: a) end dowels, b) support blocks, c) a base plate, d) loading head and pivot, and e) tongue and connector. Each component and its function will now be described.

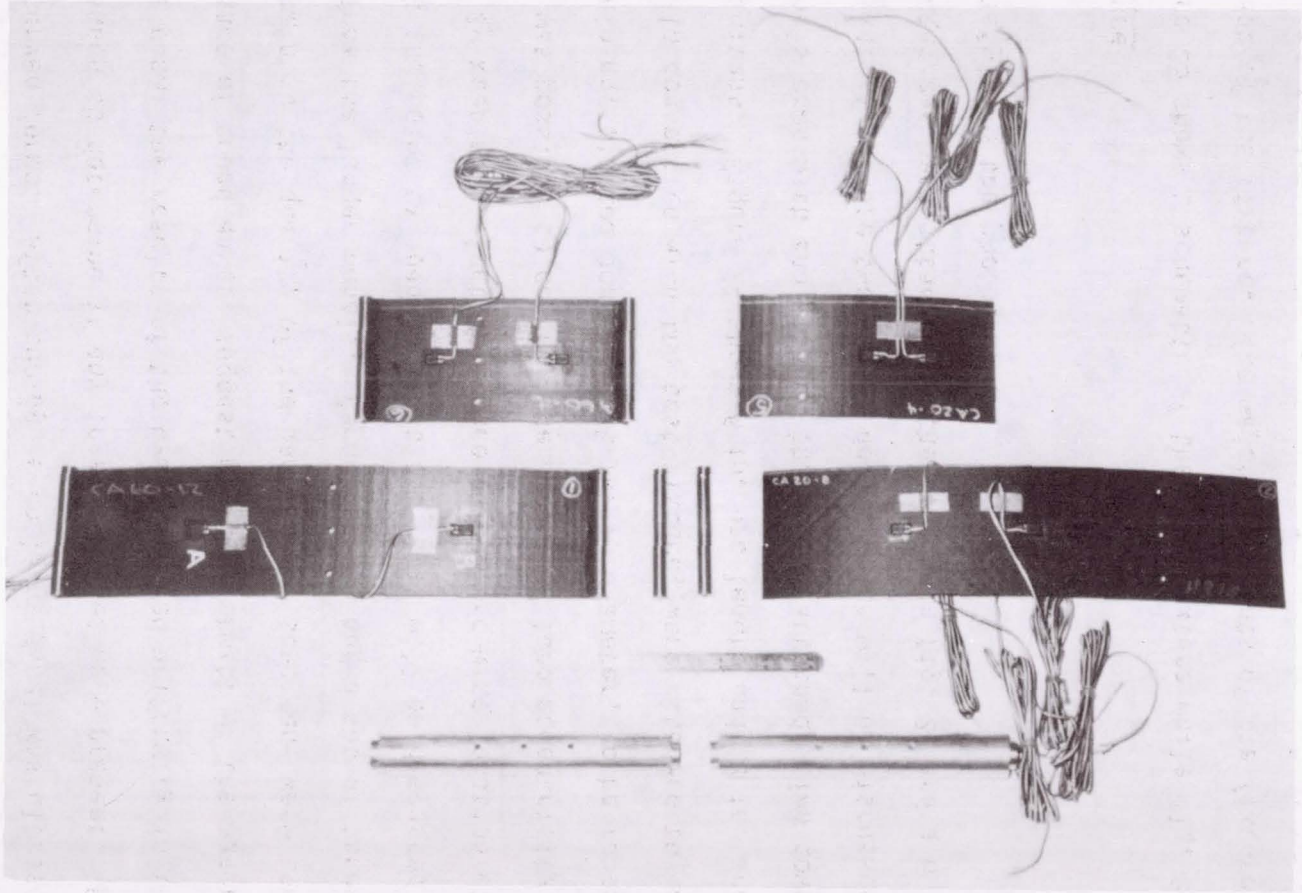

FIG. 24 PHOTOGRAPH OF MACHINED SPECIMENS

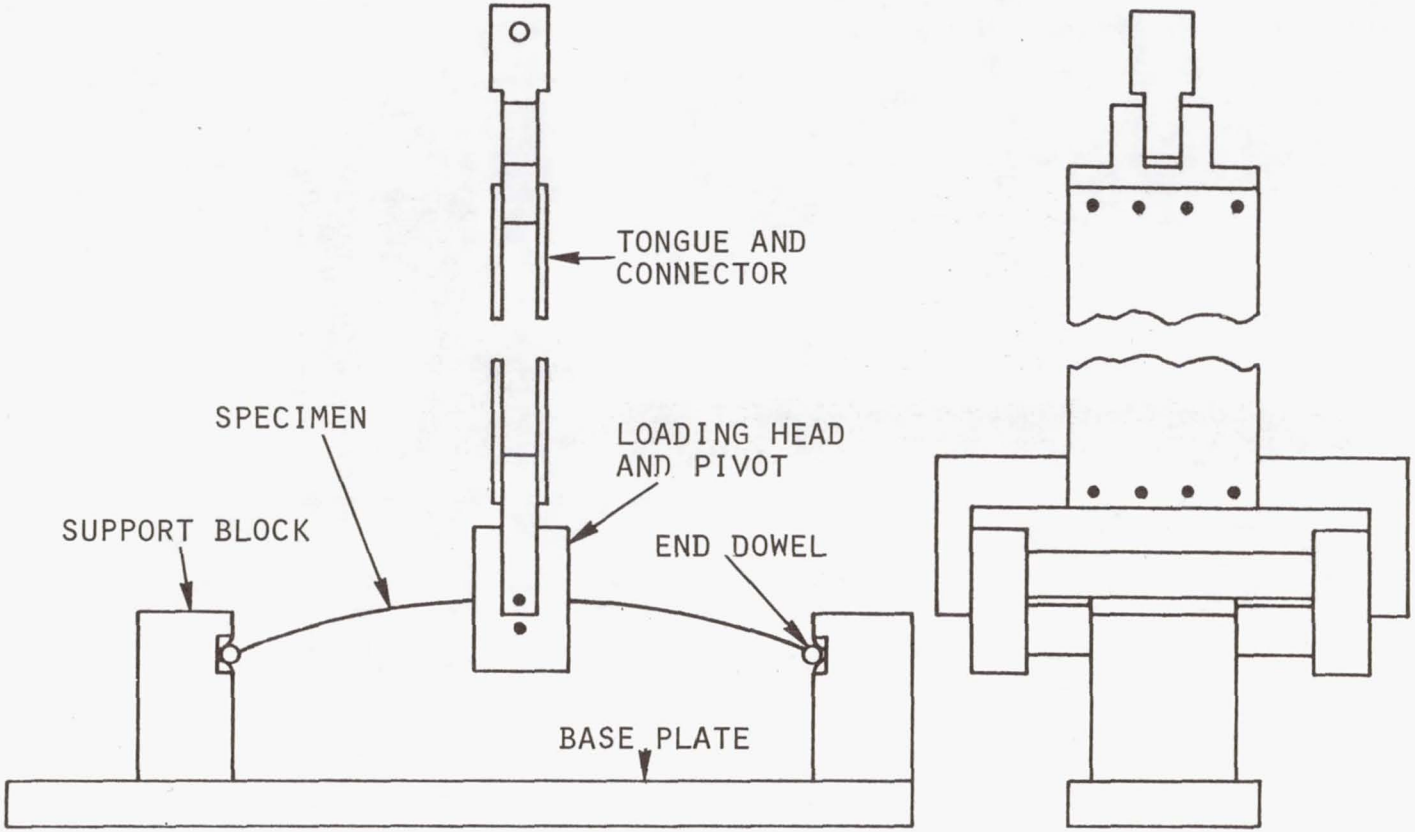

FIG. 25 SCHEMATIC OF TEST FIXTURE

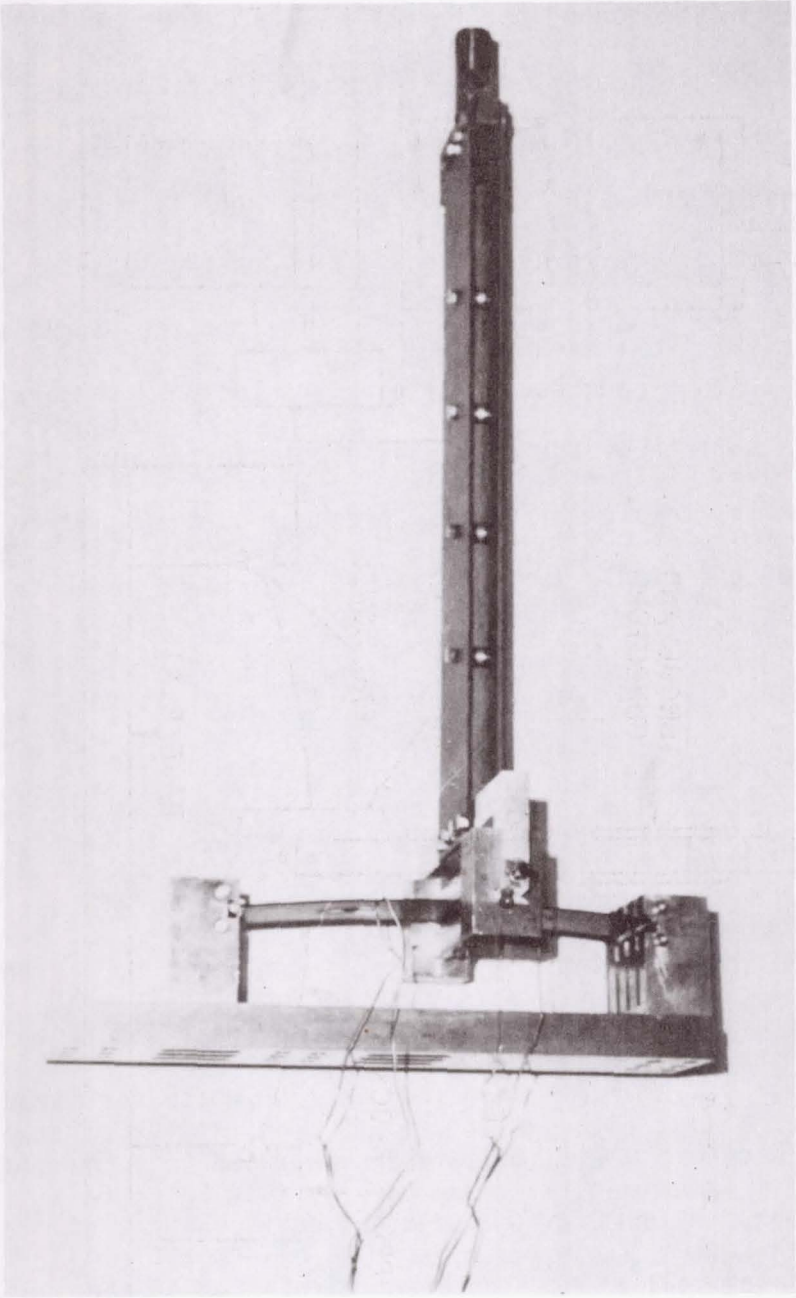

FIG. 26 PHOTOGRAPH OF TEST FIXTURE

a) End Dowels

The end dowels were 0.375 in. diameter steel rods, slotted to accommodate the ends of the curved panels. The dowels were one part of a system designed to accurately represent a simple support condition. The ends of the panel were potted solidly in the dowel slots using epoxy. The epoxy prevented the ends of the panel from brooming under the inplane compressive thrust loads. This potting is shown in fig. 27. The rods were slotted along a rod radius and the panels were centered, using shims if necessary, within the slots. With care, the end of the middle surface of the panel could be made to coincide with the centerline of the dowel. With this arrangement, the boundary conditions at the ends of the middle surface ($S = \pm S_0$) could be accurately enforced.

b) Support Blocks

The support blocks were an important component in the system and two designs were used before the test fixture was satisfactory. The support blocks provided the simple support condition by preventing translational displacements but allowing rotational displacement. The original design called for support blocks into which semicircular grooves were machined. The grooves were designed to accommodate the circular dowels. A lubricant between the dowel and the groove was used to minimize frictional effects related to rotation of the ends of the specimen. Unfortunately, due to the inplane thrust forces induced in the curved panel as it deformed, significant frictional forces developed

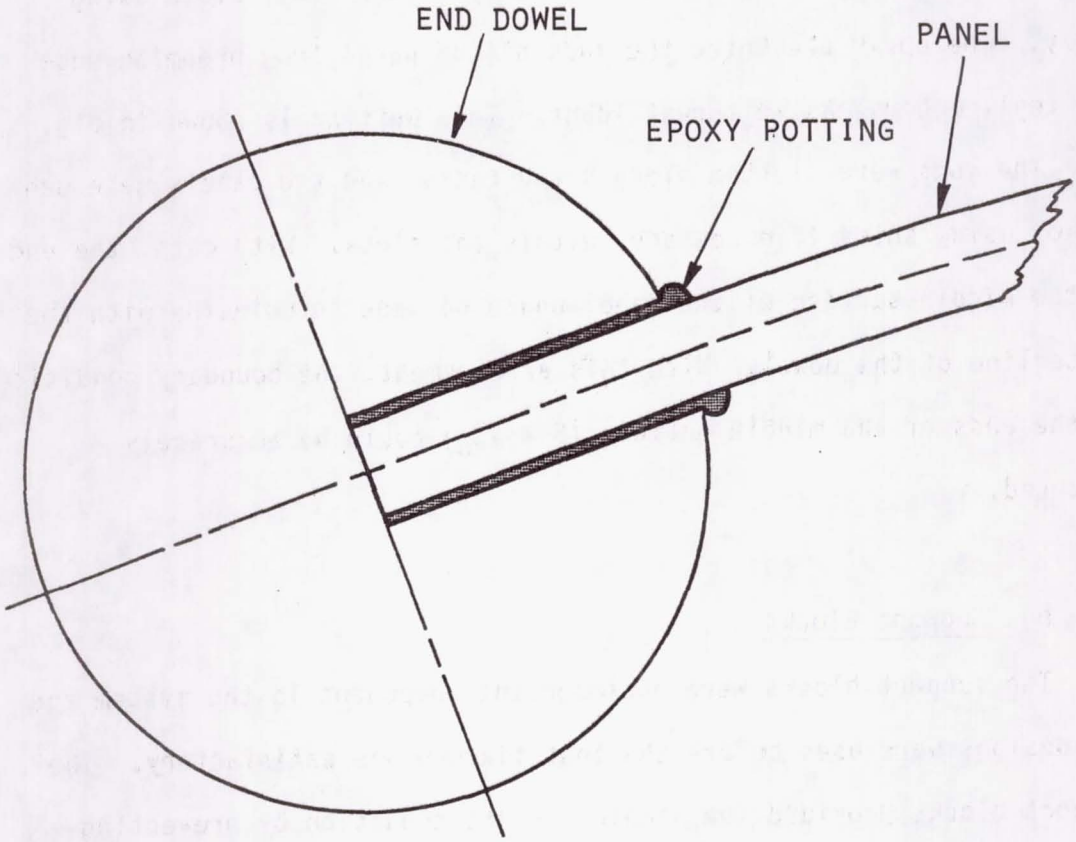

FIG. 27 SCHEMATIC OF END DOWELS

in the end blocks. These frictional forces resulted in end moments on the panel, a violation of the moment-free boundary condition assumed in the analysis. A second design of the end block used six roller bearings in each block. These roller bearings were situated so that the dowels were forced against them. This is shown in fig. 28. There were actually three bearings in a line above the end dowel and three in a line below the end dowel. Figure 29 shows a photograph of the roller bearing end blocks.

c) Base Plate

Figure 30 shows a schematic of the base plate. The base plate is also visible in figs. 25 and 26. The function of the base plate was to provide stiffness to the entire fixture and to provide a solid foundation for locating the support blocks. The base plate was 19 x 4 x 1 in. and was machined from a larger piece of steel stock. Care was taken to insure that the top and bottom surfaces of the plate were flat and parallel with each other. One support block was mounted at the location of the six isolated holes (top of fig. 30) while the other was mounted in either set of slots. Hardened steel pins, 0.250 in. in diameter and protruding from the base plate into the support block, were also used to secure the block mounted at the holes. More will be said of this shortly. The two sets of slots were to accommodate the panels of two different lengths. The slots were machined into the plate so that the position of the support blocks relative to one another could be adjusted. This was necessary since the panels all had slightly differ-

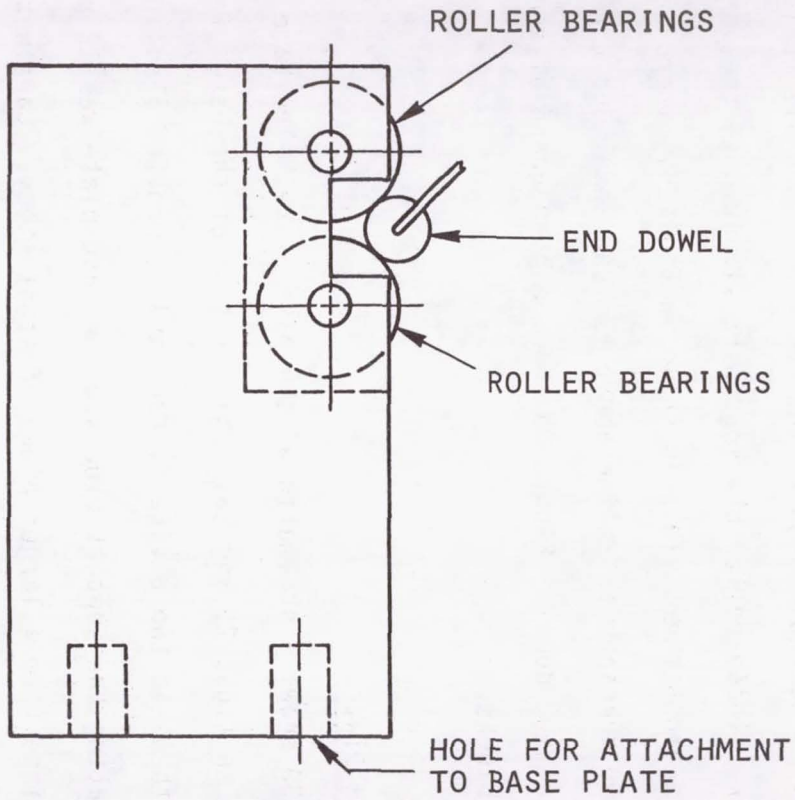

FIG. 28 SCHEMATIC OF SUPPORT BLOCK

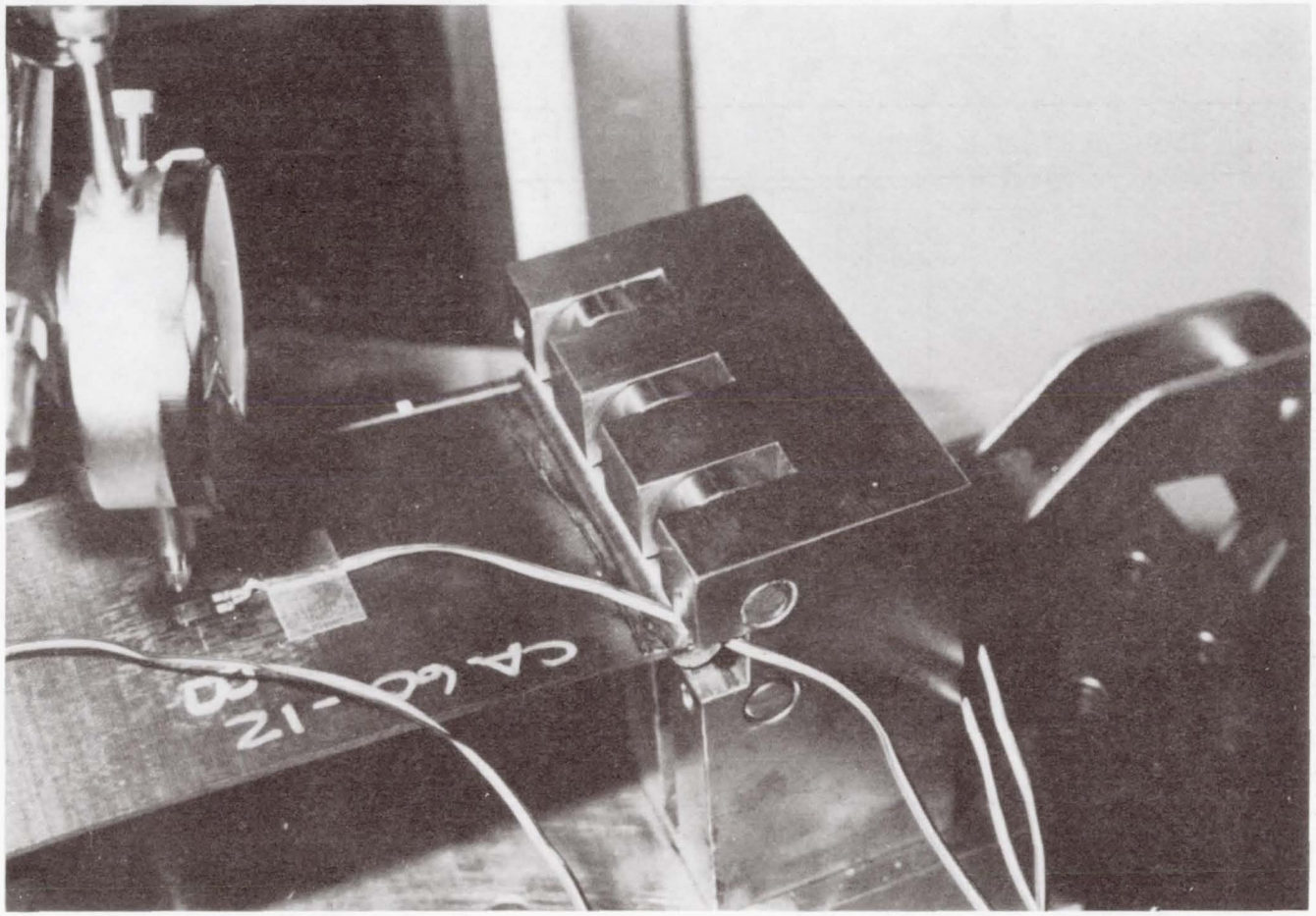

FIG. 29 PHOTOGRAPH OF SUPPORT BLOCK

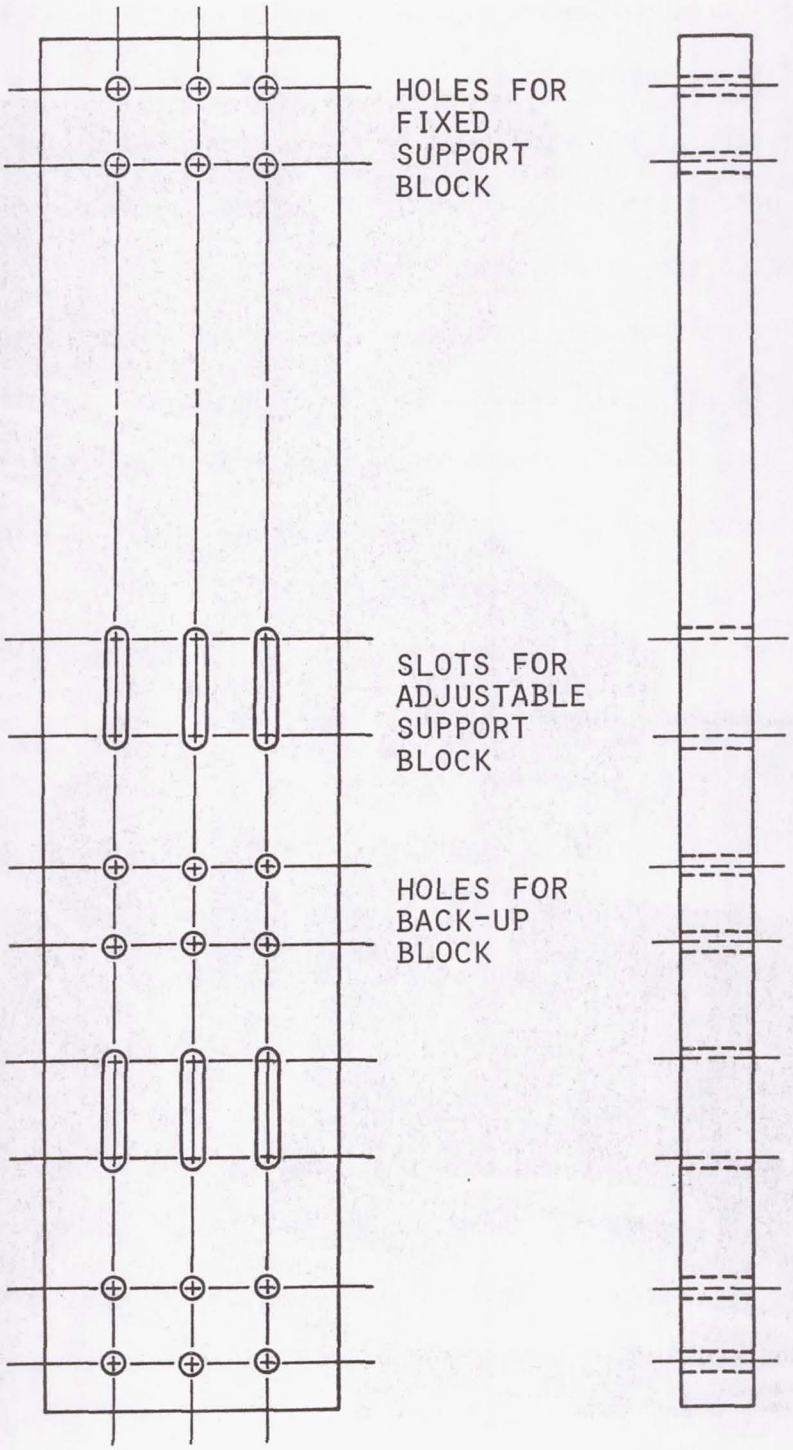

FIG. 30 SCHEMATIC OF BASE PLATE

ent lengths when machined. The block at the slotted end could be adjusted along the length of the base plate so that the panel was tight in the fixture but without the radius of curvature being too different than the natural value, i.e., the value specified in Table 1. This was very important since the response of curved panels can be quite sensitive to the initial radius of curvature.

There was concern that the large inplane forces generated as the panels deformed would cause the blocks to move relative to the base plate. This is the reason hardened steel pins were used with the one support block. For the support block attached at the slots, another design was initially incorporated. A third steel block was bolted into position at the six holes near the slots. This block was designed to be a back-up support for the block at the slots. The load was transferred to the back-up by way of several horizontally oriented bolts jammed between the back-up block and the support block. As it turned out, there was no slipping between the base plate and the support blocks at either end of the panel and so the back-up block was not used.

d) Loading Head and Pivot

The analysis assumed that the panel was subjected to a line load applied at the geometric middle surface. There were two difficulties in achieving this ideal. First, it was physically impossible to contact the geometric middle surface. A line load acting radially from above would contact the outer surface of the panel. This would result in a slight offset between the location the load was assumed to act and where

it actually did. This is not serious until the cross section of the panel at the line load location begins to rotate. Then this effect, coupled with the load, would induce a small moment in the panel, in addition to the line load. This could have been accounted for in the analysis but such a moment was deformation-dependent, making the governing equations more difficult to solve. Thus to have the line load act at the geometric middle surface, a novel loading mechanism was adapted. Incorporated into this mechanism was a scheme to insure against the second problem, namely that no moment be transferred into the panel through the loading fixture. Figure 31 shows the loading head and pivot fork used to transmit a pure line load to the geometric middle surface of the panel. Figure 32 shows the pivoting action of the mechanism. Three small bolts through the panel and the large dowels (shown in fig. 24) secured the arc-wise location of the line load. Centering the panel in the gap between the large dowels guaranteed that the line of pivoting passed through the geometric middle surface. Of course the pivots themselves prevented any moment from being transferred to the panel. Figure 33 shows a photograph of the pivot.

e) Tongue and Connector

The pivot fork was attached to the bottom end of two long steel plates. The long plate assembly, or tongue, is shown in fig. 34. In the analysis it was assumed the line load moved downward radially and deflected the panel, with the simply supported ends of the panel remaining stationary. In the experiment, the vertical displacement of the

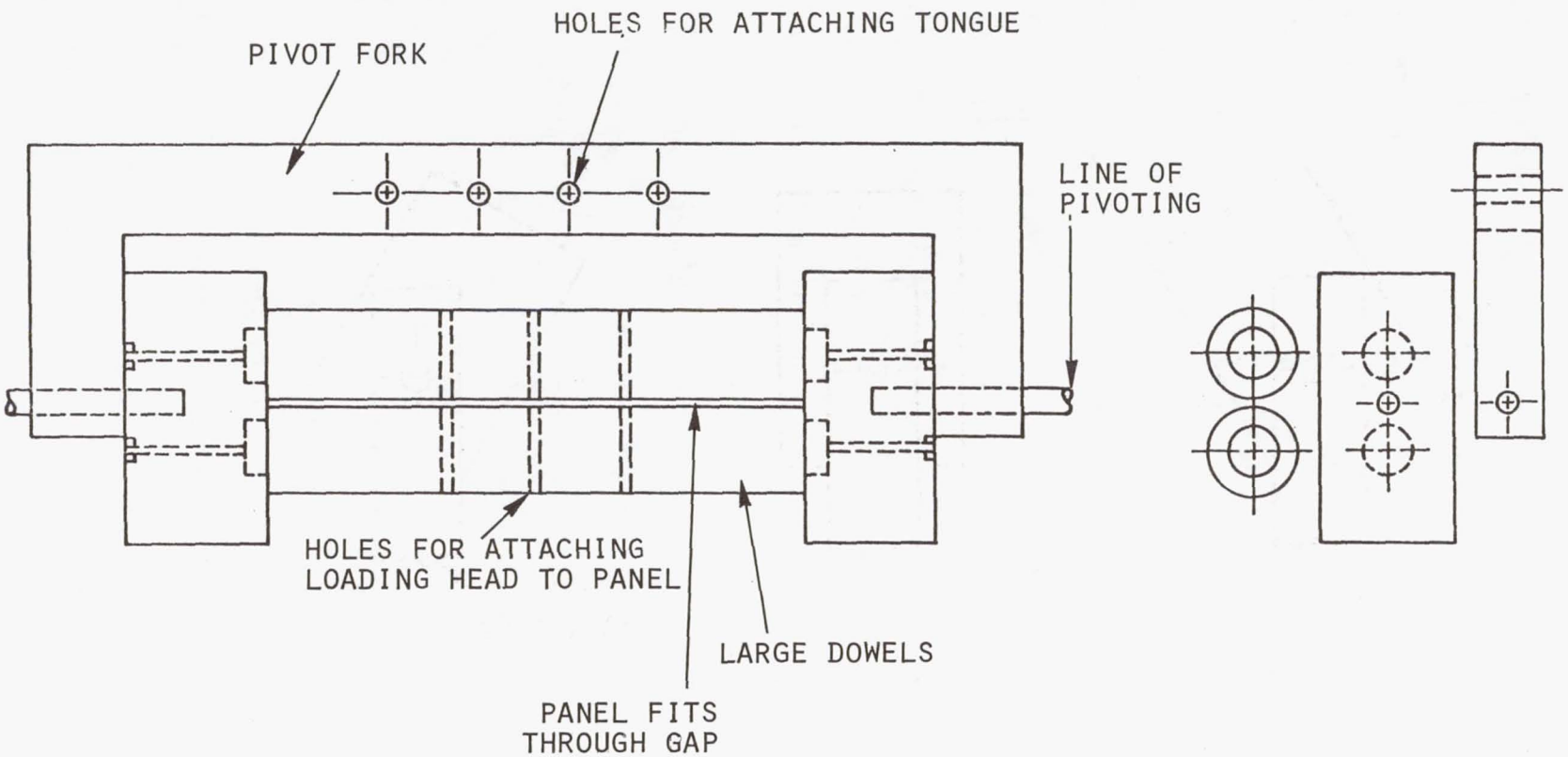

FIG. 31 SCHEMATIC OF LOADING HEAD AND PIVOT

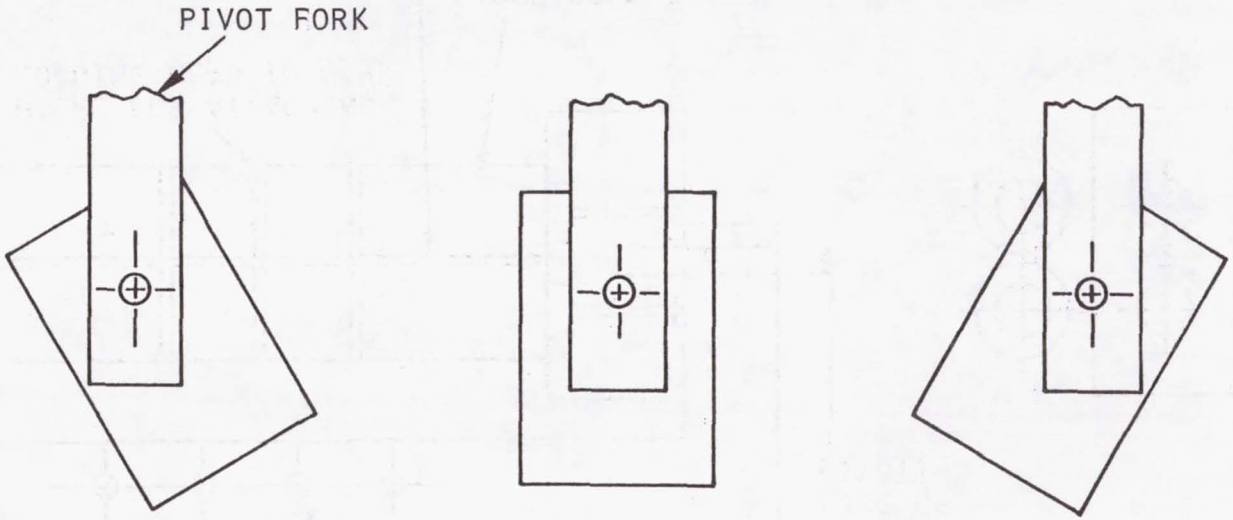

FIG. 32 ILLUSTRATION OF PIVOTING ACTION

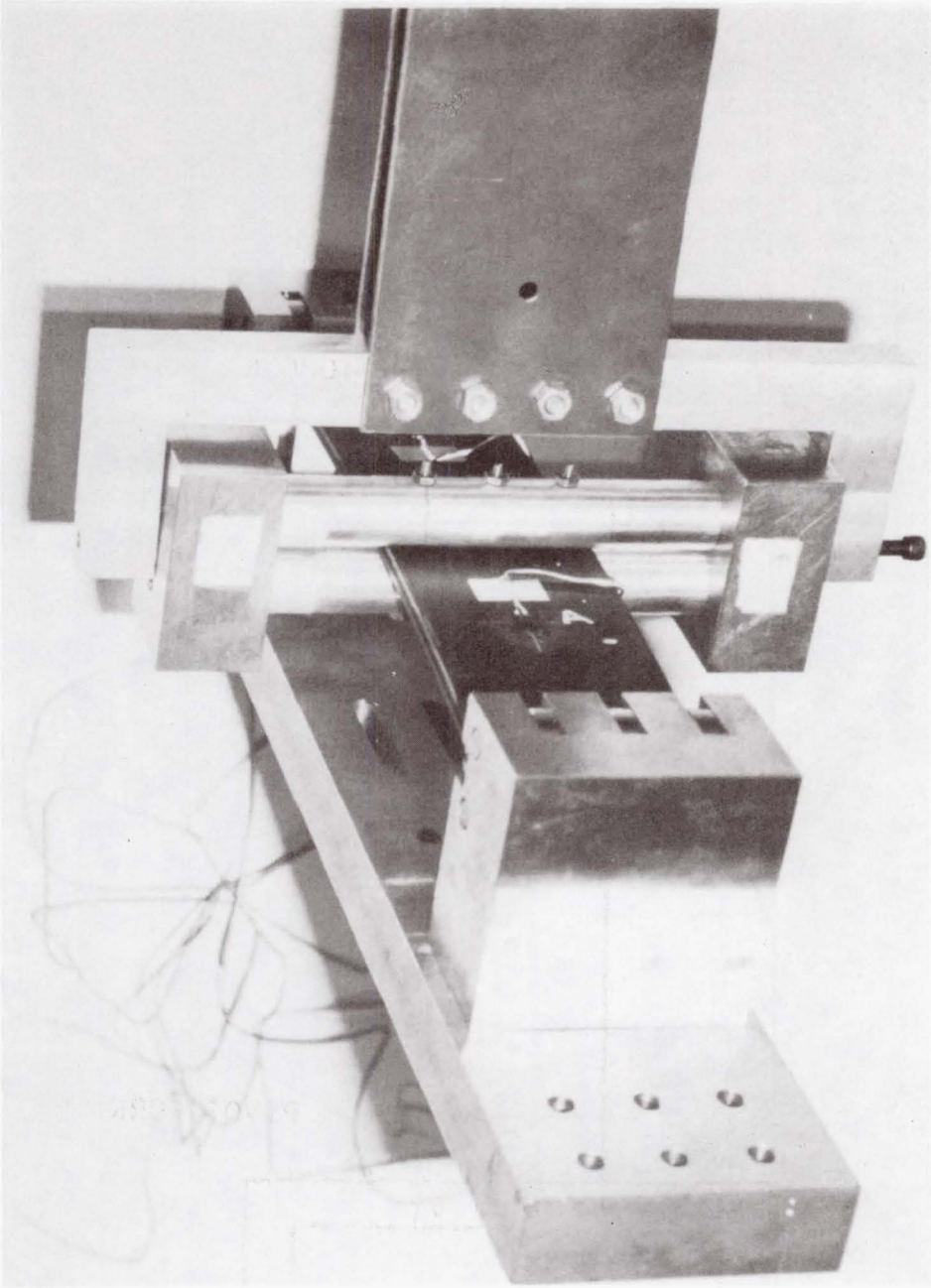

FIG. 33 PHOTOGRAPH OF LOADING HEAD AND PIVOT

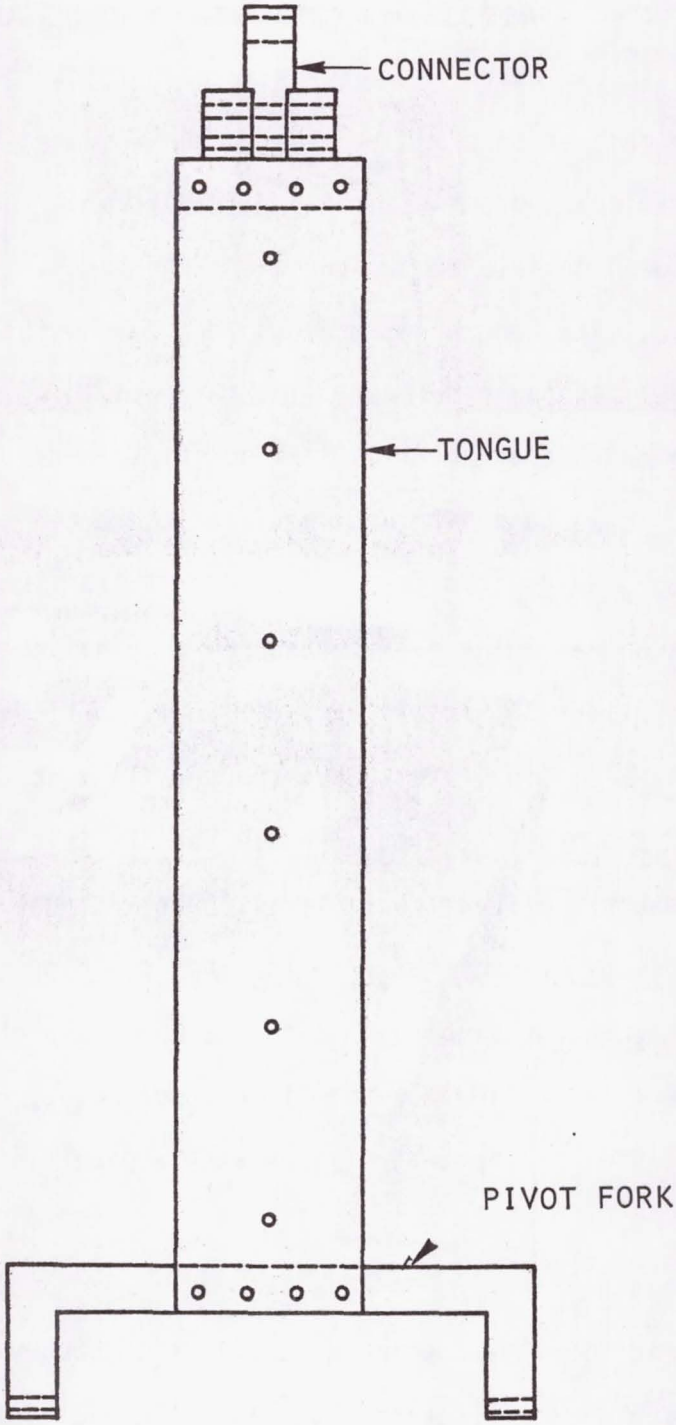

FIG. 34 SCHEMATIC OF TONGUE AND CONNECTOR

panel at the location of the line load was held to zero and the simply supported ends moved upward. Due to the assummed shallowness of the panels tested this was essentially the same as holding the radial displacement to zero at this point. The tongue was used to attach the panel to the stationary upper head of the load frame. The base plate rested on the lower movable head. To deform the panel, the lower head was moved upward. The tongue was made as long as possible for the following reason: As the panel deformed, tangential (u) displacements resulted. This meant that the line load position moved tangentially. In the analysis it was assumed that the line load acted strictly in a radial direction. To do this the line load must translate tangentially, the line of action remaining parallel to the original no-load direction. Experimentally it was very difficult to translate the line load tangentially. An infinitely long tongue, fixed at the top and attached to the panel at the bottom, would satisfy this requirement. Practically speaking, a long tongue is all that was possible. The maximum tongue length was dictated by the physical dimensions of the load frame. A connector simply attached the upper end of the tongue to a universal joint and ultimately the fixed upper head. Figure 35 shows another overall view of the test fixture with a panel in place.

Instrumentation

After fabrication the specimens were instrumented with 350 ohm strain gages with a gage length of 0.25 in. The excitation voltage for the strain gages was 2 volts. The strain gages were mounted back-to-

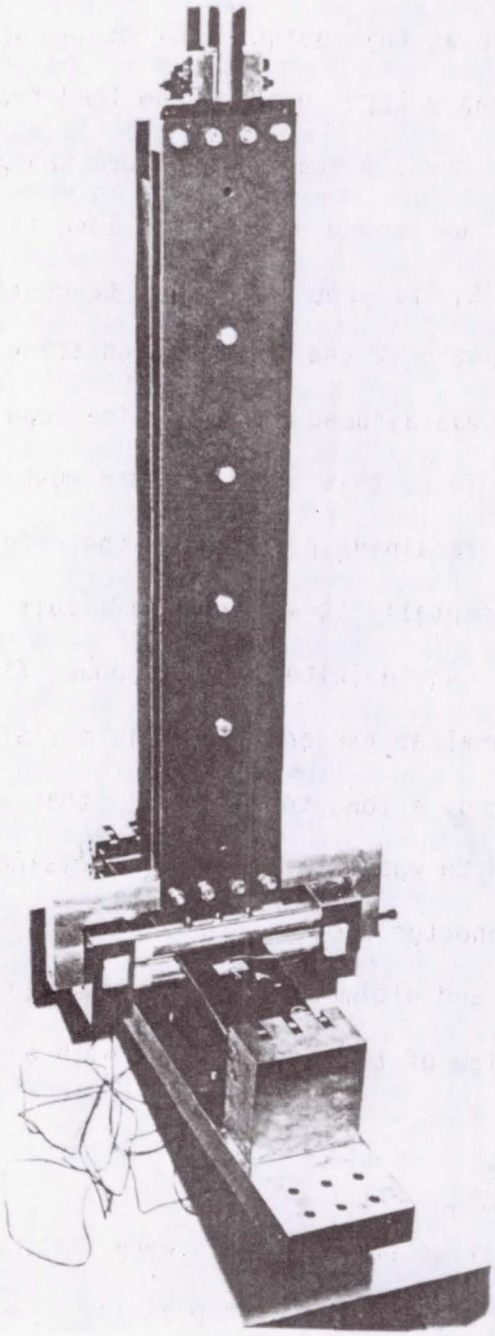

FIG. 35 PHOTOGRAPH OF TEST FIXTURE

back on the specimens so that the middle surface strain could be monitored. The location of the gages was determined by the amount of load offset for the specimen. For load offsets of 15% of the semi-opening angle and less, the gages were placed at the quarter points. When the load offset exceeded 15% the gages were placed at midspan and at the quarter point furthest from the load. To measure the radial displacement, dial gages mounted radially were employed. The dial gages were capable of measuring displacements of 0.001 in. and greater. Again the location of the dial gages depended on the degree of the load offset. For offsets of 15% and less, the dial gages were located at the quarter points and at the point of load application. For offsets greater than 15% the dial gages were placed at the point of load application, midspan, and at the quarter point farthest from the load. The tests were carried out in the Engineering Science and Mechanics department of Virginia Tech using a displacement-controlled Instron loading frame. The load was determined using a 1000 pound Instron load cell placed in series with the load fixture. The strain gage data was acquired using a system consisting of Vishay 2120 Wheatstone bridges and signal conditioner, an HP3495A scanner with an A/D converter, and a Tektronix 4051 computer. The dial gage readings were manually entered into the Tektronix computer while strain gage and load data were automatically recorded on digital tape. Figures 36 and 37 shows the experimental set-up with instrumentation in place.

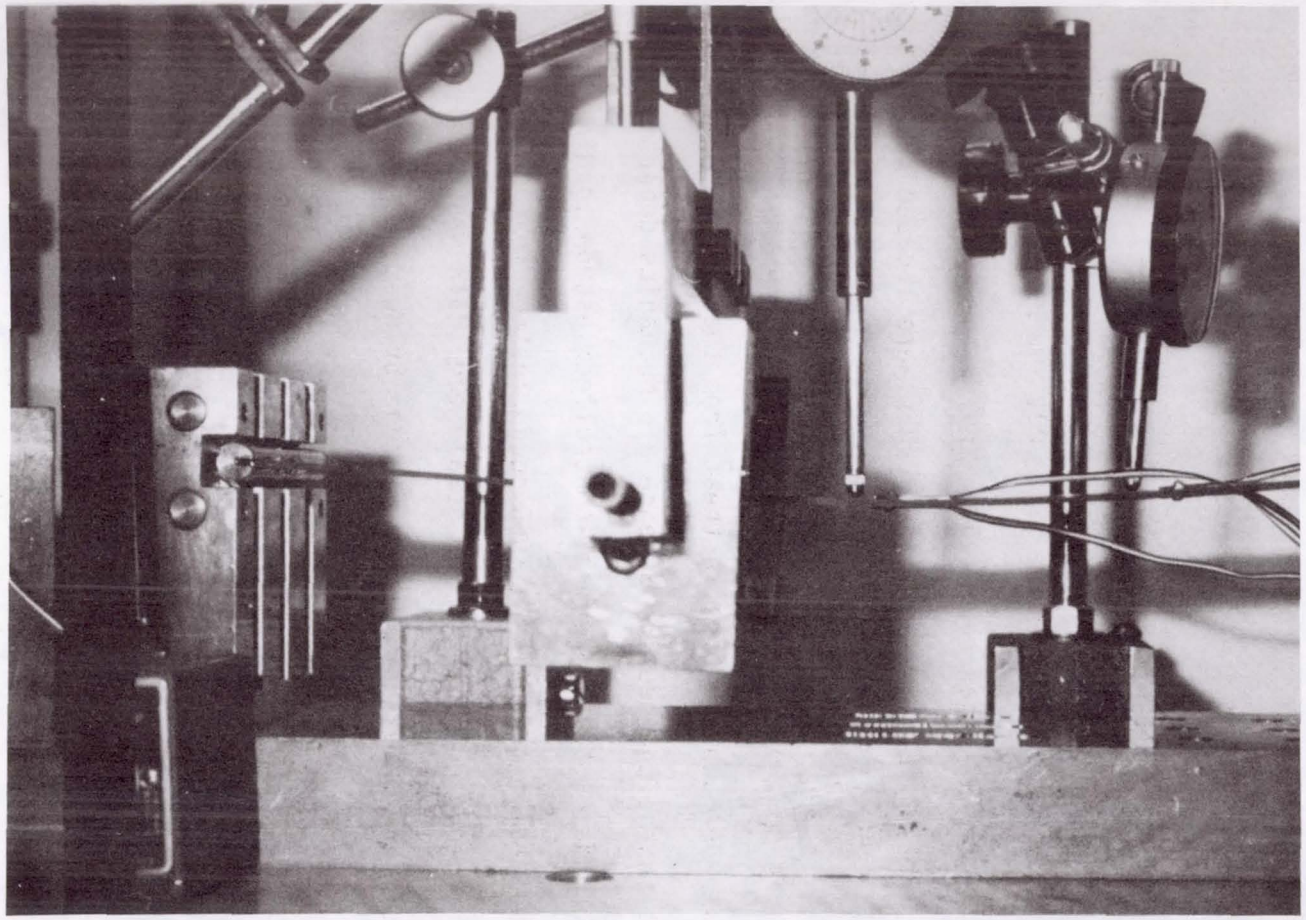

FIG. 36 PHOTOGRAPH OF EXPERIMENTAL SET-UP
SIDE VIEW

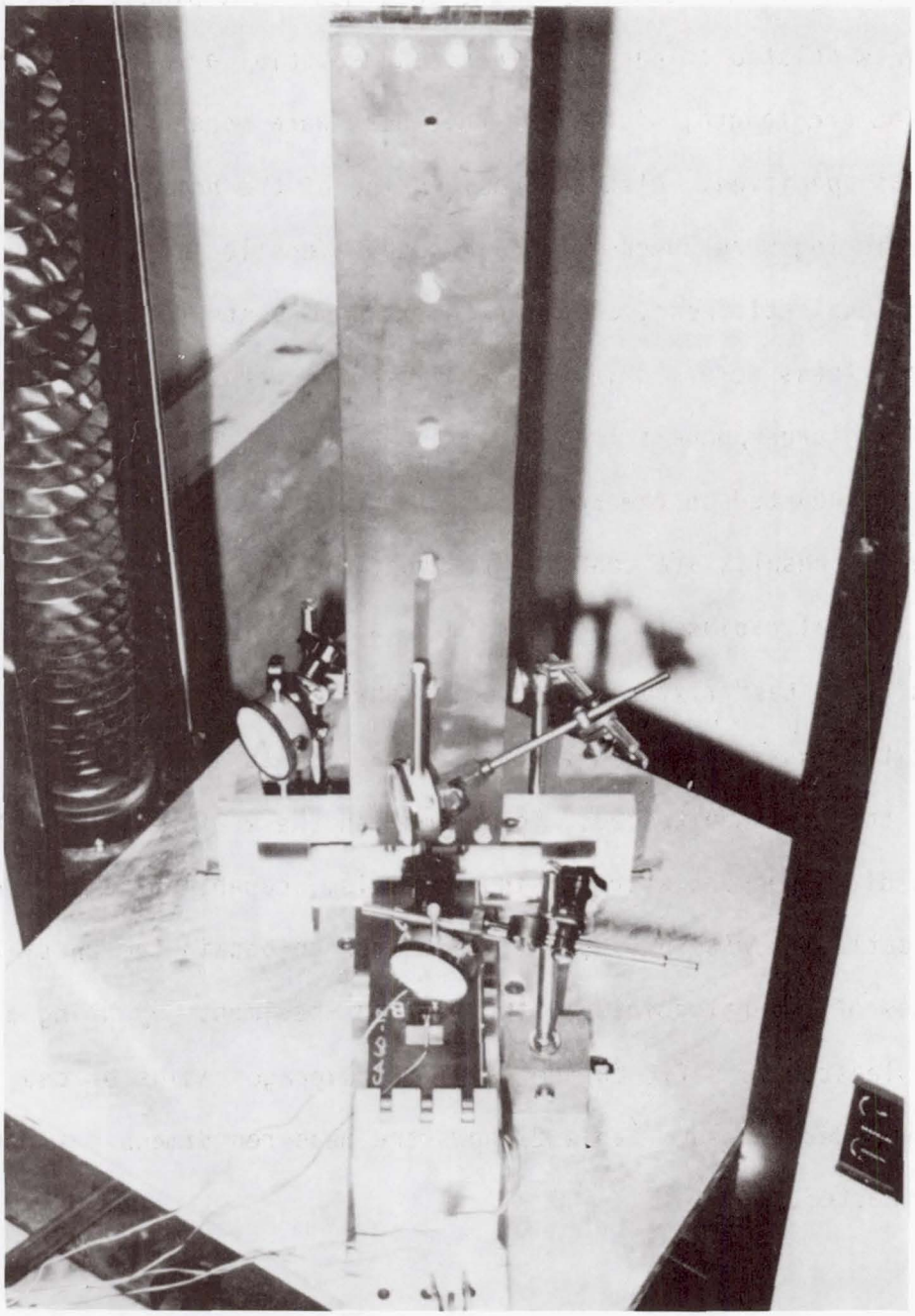

FIG. 37 PHOTOGRAPH OF EXPERIMENTAL SET-UP
END VIEW

Initial Measurements

Before the actual testing of the specimens took place, some initial measurements related to panel geometry and material properties were taken. The arc length, width, and thickness were measured to assure each was as specified. Also the positioning of the holes drilled for load positioning were checked for accuracy. Tensile tests to determine the extensional stiffness, and three point bend tests to determine the bending stiffness were made. The tensile tests were performed on strips cut from the larger panels from which the specimens were cut. The bend tests were conducted on the actual specimens. Details of the test procedure and results are contained in Appendix C.

The initial radius of each specimen was measured after it was fitted into the test fixture. Measuring the radius after the panel was in the fixture assured that the measured radius was indeed the initial radius of the specimen tested. To accomplish the measurement of the radius, a dial gage and a traversing mechanism, capable of measuring arc length location to within 0.05 in., were used to obtain the spatial coordinates of several points on the mounted specimen. By using a parabolic least-square fit to the data, the average radius of the specimen was determined. Table 2 shows the measured dimensions for the specimens tested.

Test Procedure

Having made the initial measurements on the specimen, excluding the radius measurement, it was placed loosely in the test fixture. In this

Table 2

Measured Test Specimen Geometry

Specimen Number	Radius (in.)	Thickness (in.)
1	56.34	.084
2	52.04	.082
3	54.72	.083
4	51.00	.082
5	55.42	.060
6	55.34	.062
7	50.35	.063
8	50.09	.063
9	52.56	.042
10	55.41	.043
11	57.33	.042
12	64.7	.082
13	62.4	.081
14	63.8	.081
15	50.41	.022
16	--	--
17	--	--
18	--	--

Note: Of specimens 15-18 only specimen 15 was actually tested, thus specimens 16-18 had no initial measurements made.

position the strain gages were connected and they were balanced and zeroed. The specimen was then tightened in the fixture by sliding the movable support block. To assure a tight fit the specimen was slightly compressed by the support blocks until a slight bending strain was registered. The loading head was then attached and the levelness of the fixture and the vertical orientation of the tongue were checked and corrected as needed. The initial radius of curvature measurements were then taken. After this, the load cell reading was zeroed. The displacement rate was set at 0.01 in./min. and readings of load, strain, and displacement were recorded at every 0.01 in. of midspan displacement. To record the dial gage readings, the loading head displacement was stopped. The readings were then entered into the Tektronix. During the first tests the support blocks were monitored with dial gages for any sign of elastic or rigid body displacement. Since the blocks showed no sign of bending or slipping relative to the base plate, this was discontinued for later tests.

Chapter 5

CORRELATION OF EXPERIMENTAL AND THEORETICAL RESULTS

In order to validate an analysis it is necessary to compare it with experimental results. Here the analytic results presented in Chapter 3 are compared to experimental results obtained using the apparatus and test fixture described in Chapter 4. So as to make the comparison with the experiment clearer, the analytic results shown represent only those configurations assumed to be stable. The initial measurements made on the test specimens concerning the geometry and material properties were used in generating the analytical curves presented with experimental results. Also, the small initial strain in the panels, due to fitting the specimens into the fixture, has been subtracted from the experimental data presented. In all tests performed this initial strain was less than $50\mu\varepsilon$ in magnitude, or less than 2.5% of the maximum strain. Both the experimental and analytic results are presented in nondimensional form, with the exception of the shape data, where the units are inches.

In general, the agreement between theoretical and experimental results was good. All the trends predicted by the analysis were observed in the experimental results. Although the agreement was seen to be good, there was still some deviation between theory and experiment. This deviation may be attributed to a number of factors. Perhaps the most significant was the fact that the specimens were found to have imperfect shapes, i.e., they were not exactly circular. The work done by Schreyer [4] shows that geometric imperfections have much the same

effect on panel response as do load eccentricities. This is the most likely reason for not seeing a distinct bifurcation of the equilibrium path when the load was exactly at midspan. Other possible factors for deviation of the experimental results from the predictions include the possibility of friction-generated moments at the supports, even though great care was taken to minimize this. The friction was manifested by small load jumps, characteristic of end support sticking, observed during the testing of the panels. Thickness variations observed in the test specimens during the initial measurements were also likely to cause differences between experiment and theory. This thickness variation could be responsible for the differences between the predicted and observed maximum surface strains seen for some of the test specimens.

In this section the experimental results from selected test cases are presented. These cases, along with their associated parameters, are given in Table 3. Since the trends observed for most of the panels tested were similar, the test cases shown here are representative. Results from the $[90/0]_s$ panels, which were quite thin, are not shown here. Problems with these specimens developed during the testing. It appeared that friction generated at the supports was, at times, sufficient to constrain free rotation of the specimen. The specimen would actually bend at the support ends and so the specimen behaved at times as if it had clamped ends instead of simply supported ends.

Figures 38-40 show the predicted and observed response for a $[(90/0)_4]_s$ composite specimen with a 12 in. arc length, a 56.34 in. radius, and no load offset, test case 1. The analytic predictions are

Table 3

Test Cases Presented

Test Case Number	Specimen Number	Lay-up	Radius (in.)	Arc Length (in.)	Offset Angle (%)
1	1	$[(90/0)_4]_s$	56.34	12	0
2	2	$[(90/0)_4]_s$	52.04	12	15
3	3	$[(90/0)_4]_s$	54.72	12	30
4	5	$[(90/0]_3]_s$	55.42	12	0
5	6	$[(90/0)_3]_s$	55.34	12	15
6	9	$[90/45/0/-45]_s$	52.56	12	15
7	12	$[(90/0)_4]_s$	64.7	6	0

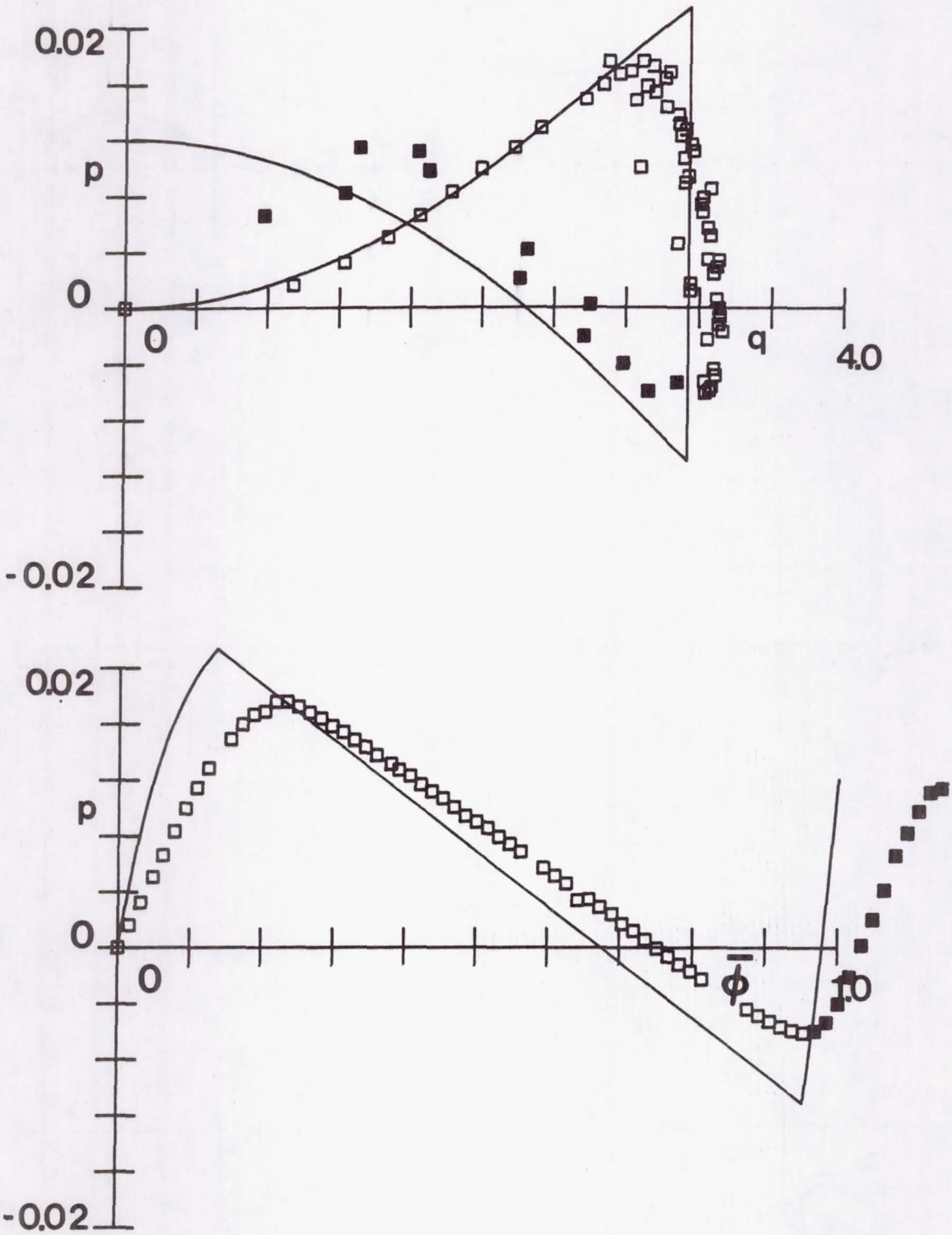

FIG. 38 COMPARISON OF THEORY AND EXPERIMENT: LOAD-THRUST AND LOAD-DISPLACEMENT RELATIONS; R=56.34, S=12.0, $\bar{\bar{\Gamma}}$=0.0, $[(90/0)_4]_S$

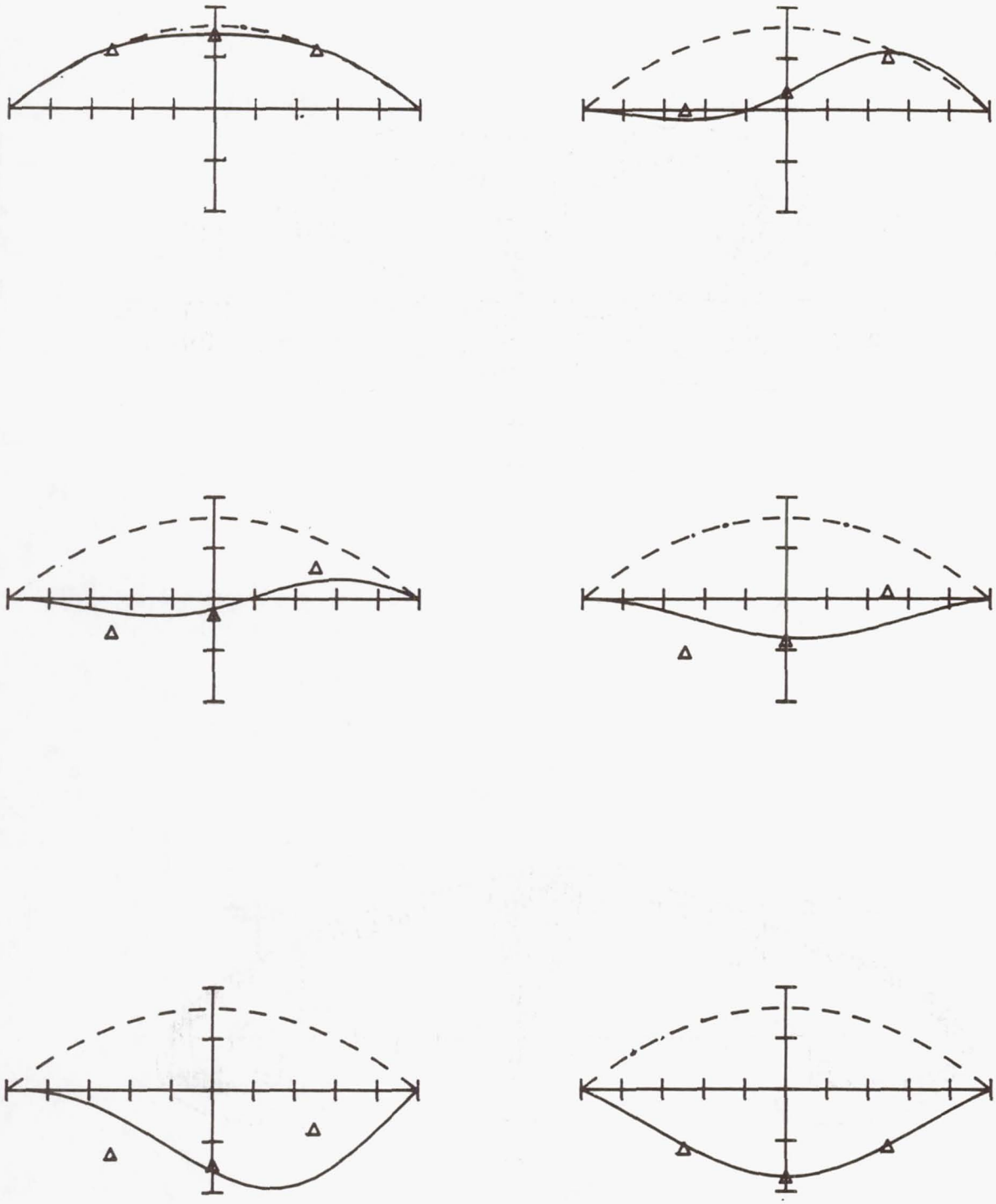

FIG. 39 COMPARISON OF THEORY AND EXPERIMENT: EQUILIBRIUM CONFIGURATIONS; R=56.34, S=12.0, $\overline{\Gamma}$ =0.0, $[(90/0)_4]_S$

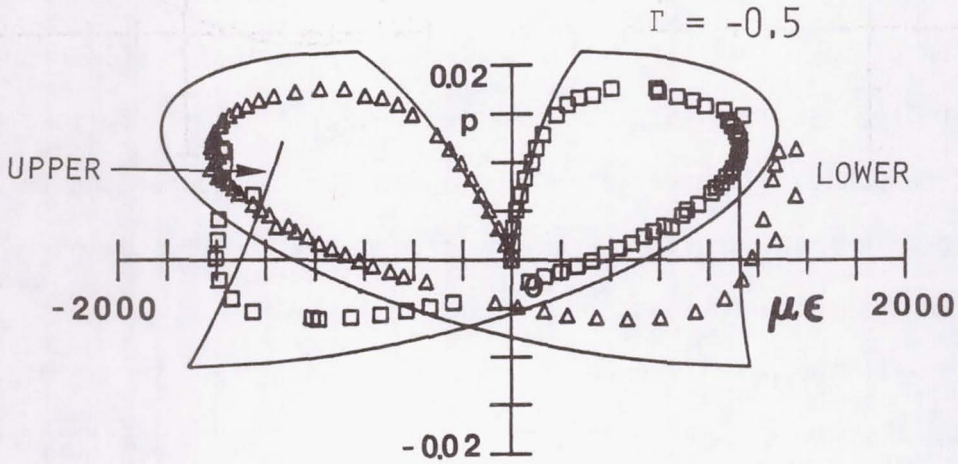

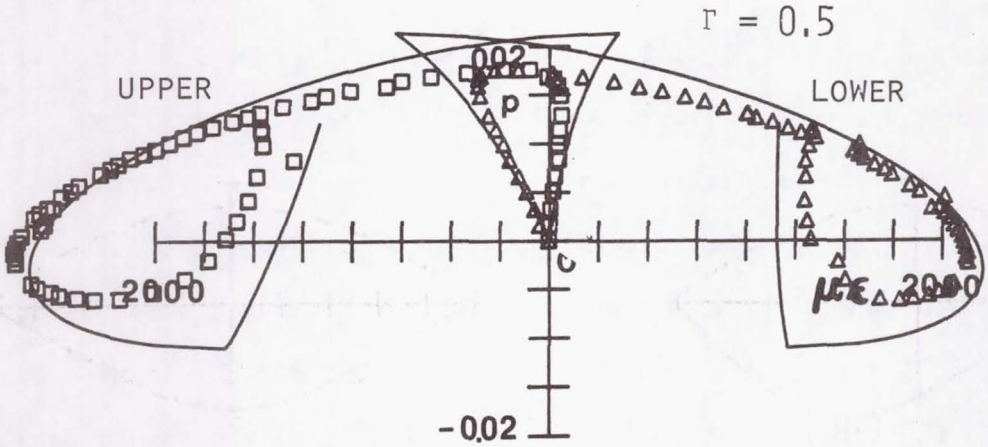

FIG. 40 COMPARISON OF THEORY AND EXPERIMENT: SURFACE STRAINS VS. APPLIED LOAD; R=56.34, S=12.0, $\bar{\Gamma}$=0.0, $[(90/0)_4]_S$

represented by the solid line while the open symbols represent the experimental data. The analysis predicts that such a panel will exhibit bifurcation of the primary equilibrium branch. The load-displacement diagram of fig. 38 shows that the observed behavior closely follows the predicted response. (The darkened symbols in fig. 38 correspond to decreasing values of thrust.) From the discussion of bifurcation behavior in Chapter 3 this suggests that the initial imperfections associated with the panel are relatively small. The load-thrust diagram of fig. 38 shows more clearly that the actual behavior is limit point behavior. Since it has been shown that geometric imperfections effect the panel response in much the same way as do load eccentricities, it would be beneficial to refer to the discussion in Chapter 3 of the effects of load eccentricities on panels exhibiting bifurcation behavior when they are loaded exactly at midspan. Appendix D investigates the effect of geometric imperfections on the panel behavior. It should be noted here that the inplane stress resultant, N_θ, is assumed to be constant (see eq. 80). Perhaps, this is not exactly true and the deviation of theory and experiment is due to a slight spatial variation of the thrust. To experimentally obtain the thrust parameter, q, the back-to-back strain gages at each spatial position are averaged to obtain the middle surface strain. The thrust parameter is then calculated, using eqs. 65, 105, and 123, at each point and is then averaged. Despite the symmetry to the set-up, for a given specimen and load, the thrust parameter at each strain gage location did not have the same numerical value. This suggests that q may not have been spatially constant.

Alternatively, a slight misalignment of the strain gages or other errors associated with strain gage measurements could have made a very accurate determination of q impossible. Also, it is seen from the load-displacement diagram that the initial panel stiffness, represented by the slope of the equilibrium path, observed experimentally differed from that which was predicted. This difference could be attributed to errors made in the material property and geometry measurements of the specimens. The parameter λ, which governs the panel response, is sensitive to these measurements. Appendix E explores the effect of the initial panel stiffness on the overall response. Fig. 39 shows the panels geometric configuration of various displacement levels. The panel configurations predicted by the analysis are purely symmetric up to the bifurcation point. After this the configurations become asymmetric. Though not shown in fig. 39, during the experiment it was observed that the configurations began to show asymmetry at much lower load levels than were predicted. This again led one to believe that geometric imperfections were present. Figure 40 shows a comparison between theoretical and measured strains. The maximum surface strains predicted by the theory are somewhat higher than the observed strains. This may have been due to local thickness variations, since only an average panel thickness was used in the analysis.

Figures 41-43 show the response for a $[(90/0)_4]_s$ 12 in. arc length composite specimen with a 52.04 in. radius and a 15% load offset, test case 2. With no load offset such a panel shows bifurcation response. Ideally, it would have been desirable to have a panel with a radius of

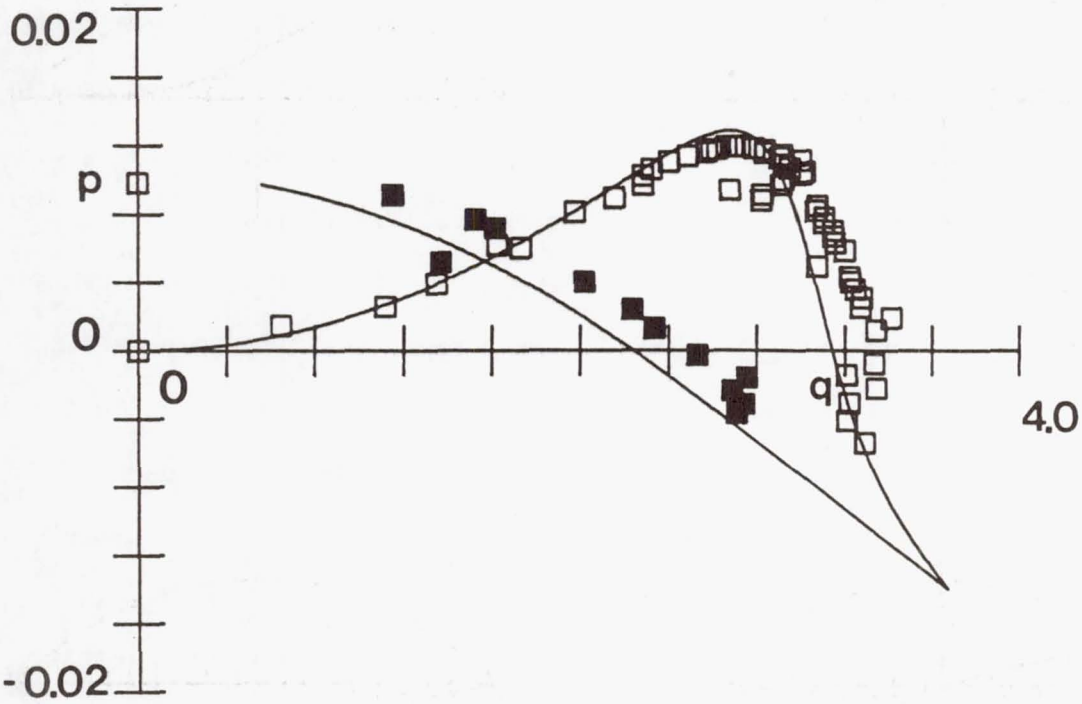

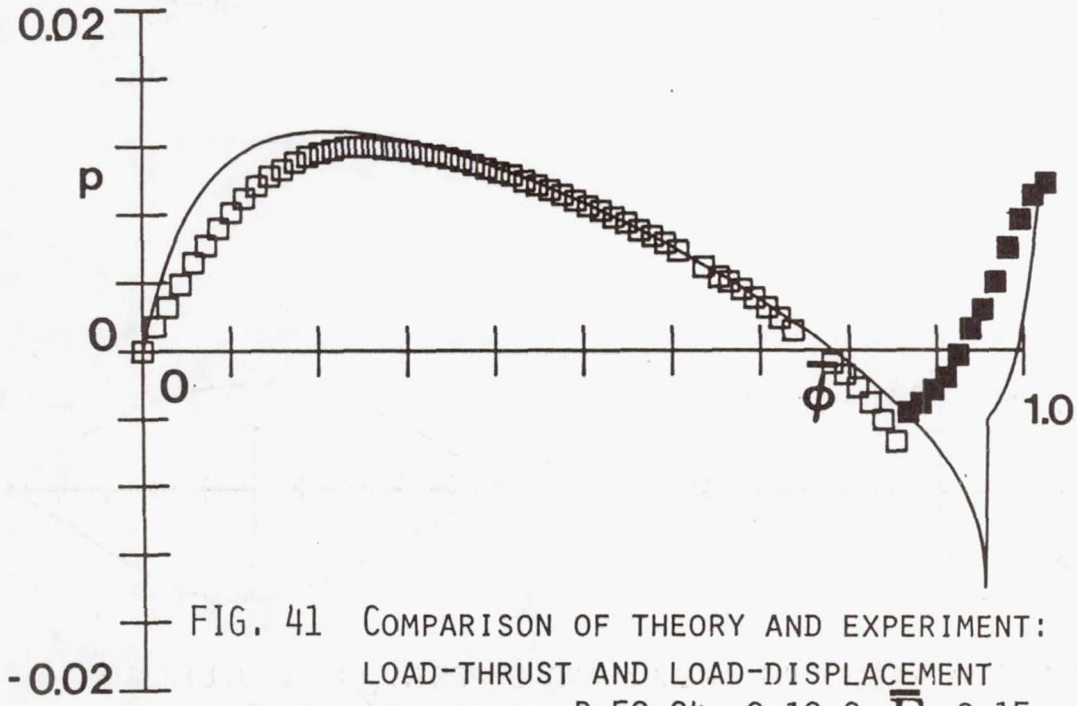

FIG. 41 COMPARISON OF THEORY AND EXPERIMENT: LOAD-THRUST AND LOAD-DISPLACEMENT RELATIONS; R=52.04, S=12.0, $\bar{\Gamma}$=0.15, $[(90/0)_4]_S$

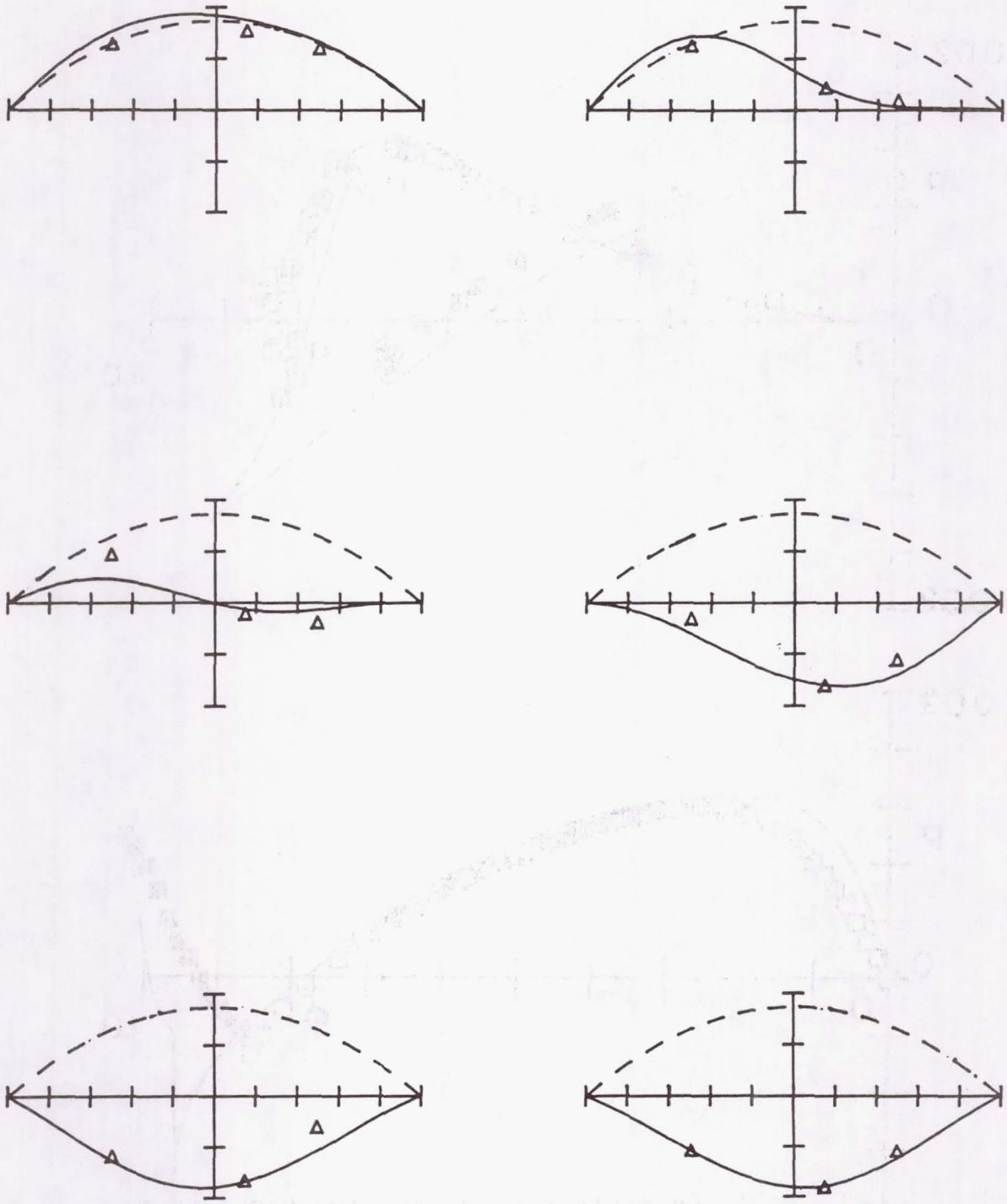

FIG. 42 COMPARISON OF THEORY AND EXPERIMENT: EQUILIBRIUM CONFIGURATIONS; R=52.04, S=12.0, $\bar{\Gamma}$ =0.15, $[(90/0)_4]_S$

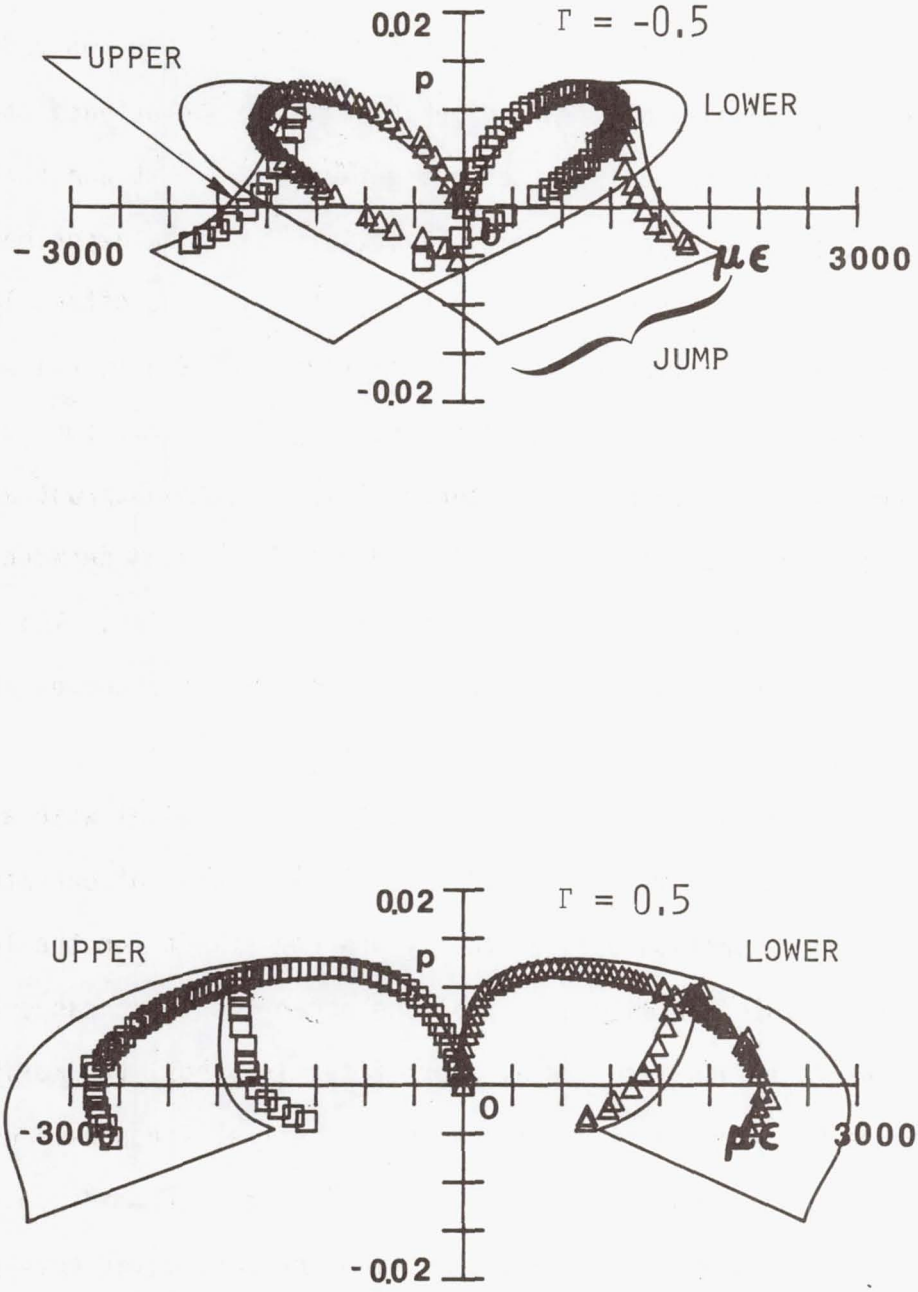

FIG. 43 COMPARISON OF THEORY AND EXPERIMENT: SURFACE STRAINS VS. APPLIED LOAD; R=52.04, S=12.0, $\overline{\Gamma}$=0.15, $[(90/0)_4]_S$

curvature equal to the first experimental case described. Since the initial radius of curvature was quite sensitive to the span between support blocks, it was difficult to obtain the same radius for a group of specimens. However, since radii of curvature for the first and second experimental cases were quite close, and since the two radii of curvature would produce bifurcation behavior in the no-offset case, it is fair to say that the only difference between the first and second experimental cases was the 15% load offset. This second experimental case performed, then, as expected. A comparison of this offset load case and the previous midspan load case shows a decrease in the experimentally determined limit loads, thus verifying the prediction that such a structure is sensitive to load eccentricity. The load-thrust and load-displacement diagrams of fig. 41 show good agreement between theory and experiment. The same is true of the shape predictions. The surface strain predictions, shown in fig. 43, deviate from the observed strains significantly.

Figures 44-46 show the results for a $[(90/0)_4]_s$ panel with a 30% offset. The panel arc length was 12 in. and the radius of curvature was 54.72 in. The comparison between theory and experiment for the load-thrust relation was not as good as for the other two first cases but still the basic trends were there. For offset loadings, the maximum thrust tends to increase with increasing load offset for panels which exhibit bifurcation behavior when the load is exactly at midspan. Thus the force on the supports increases. During the testing of this specimen it was observed that friction at the supports had more of an effect

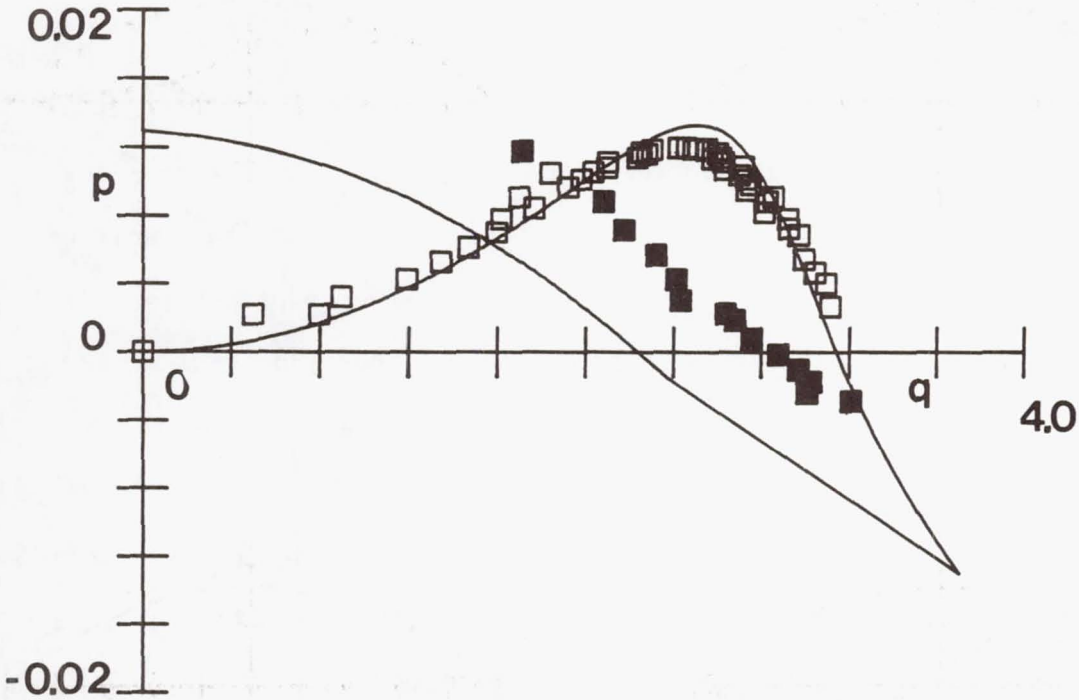

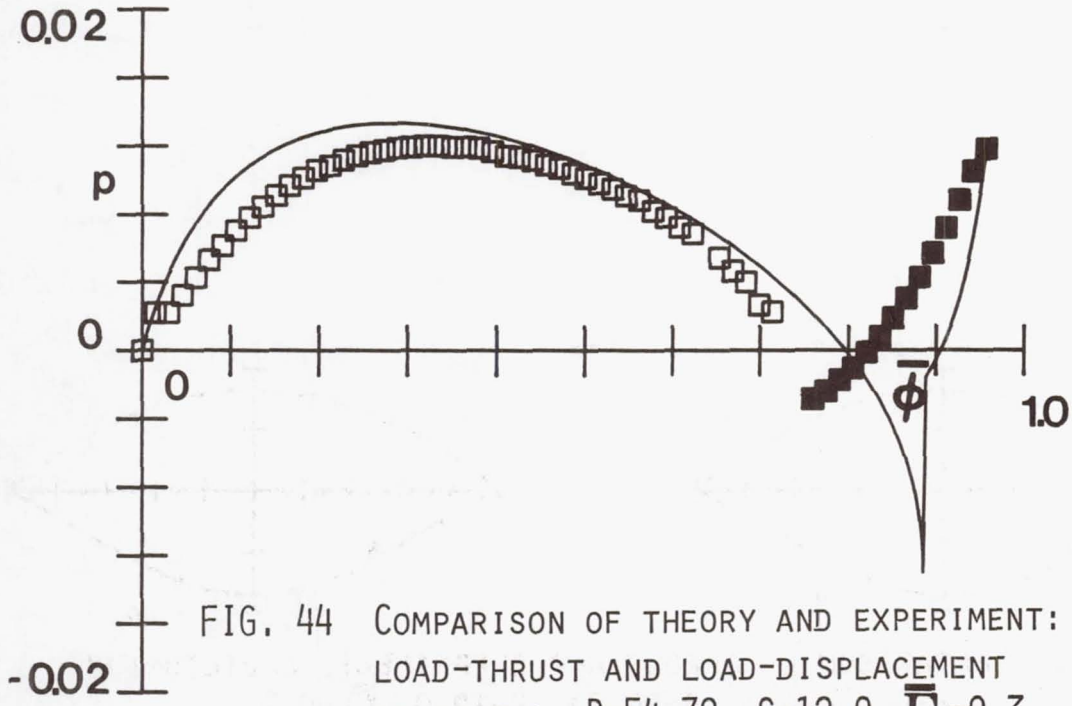

FIG. 44 COMPARISON OF THEORY AND EXPERIMENT: LOAD-THRUST AND LOAD-DISPLACEMENT RELATIONS; R=54.72, S=12.0, $\bar{\Gamma}$=0.3, $[(90/0)_4]_S$

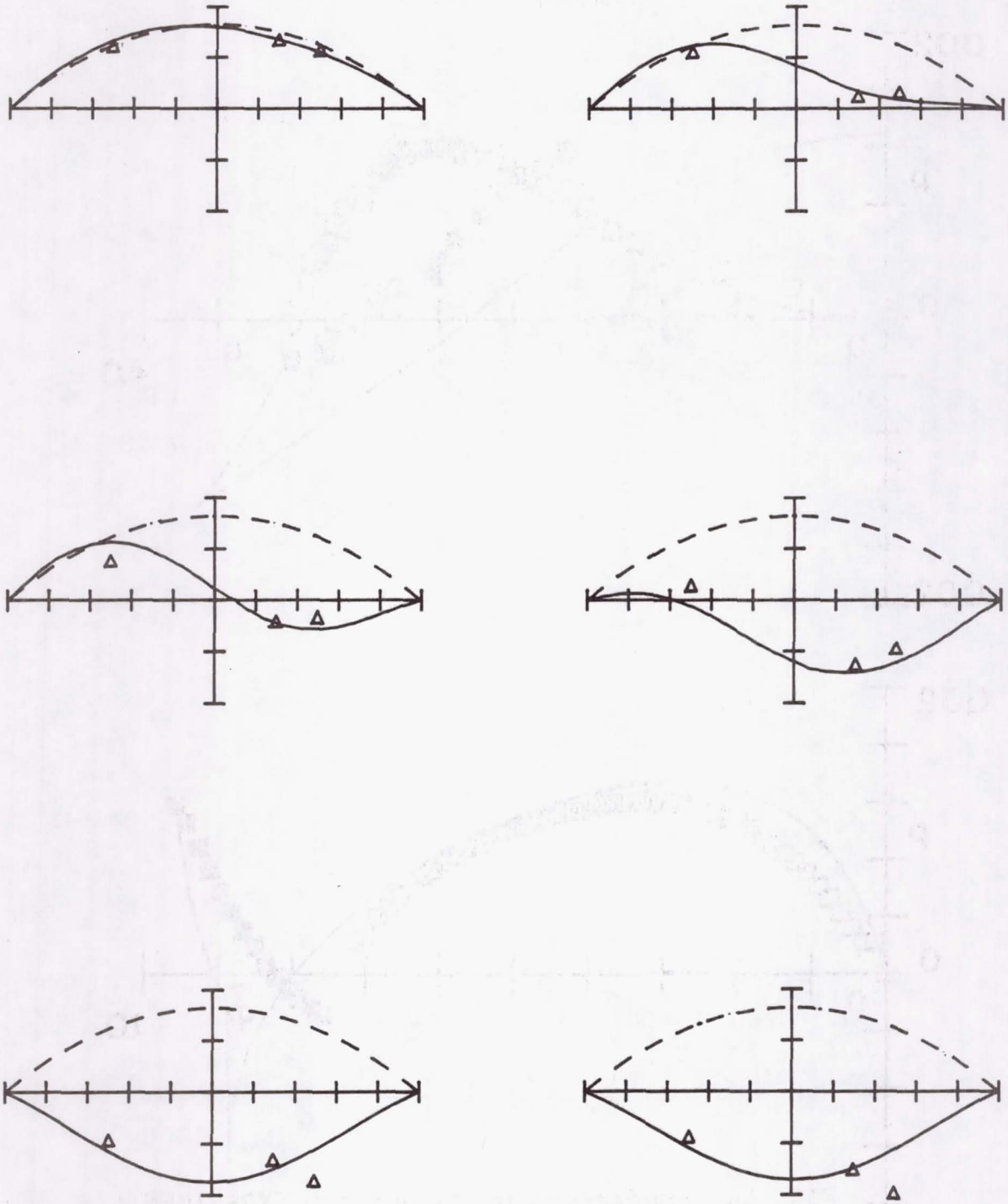

FIG. 45 COMPARISON OF THEORY AND EXPERIMENT: EQUILIBRIUM CONFIGURATIONS; R=54.72, S=12.0, $\overline{\Gamma}$=0.3, $[(90/0)_4]_S$

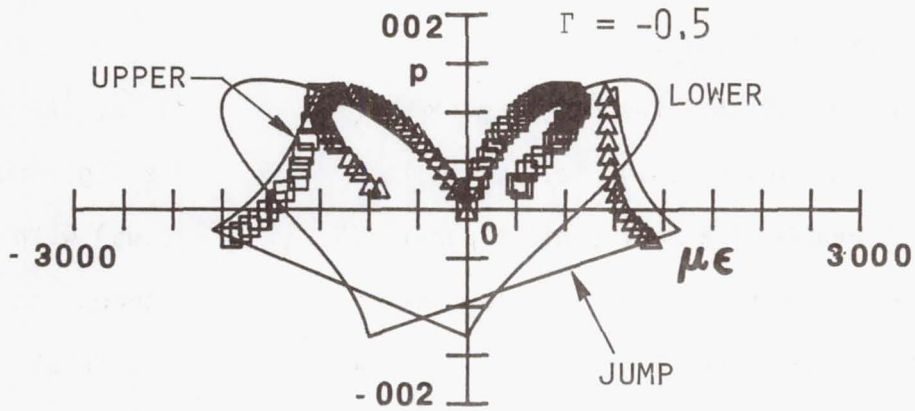

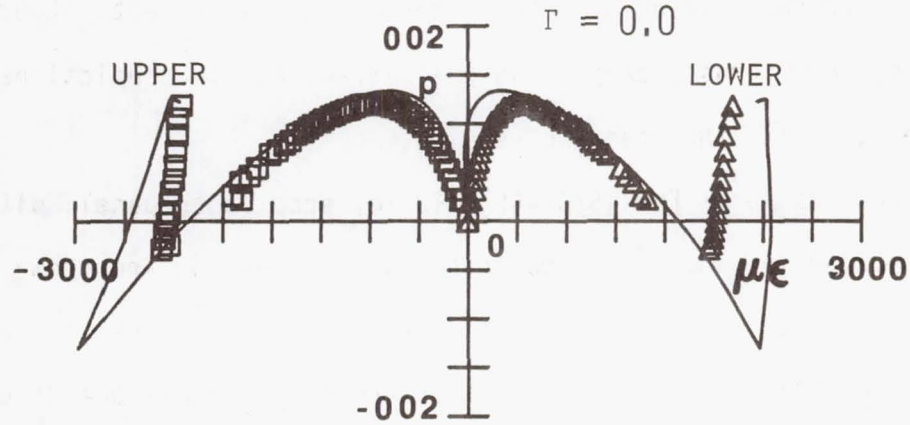

FIG. 46 COMPARISON OF THEORY AND EXPERIMENT: SURFACE STRAINS VS. APPLIED LOAD; R=54.72, S=12.0, $\bar{\Gamma}$ =0.3, $[(90/0)_4]_S$

than for the previous tests. The friction was detected from slight load jumps due to intermittent sticking of the supports, thus constraining rotation. The configurations predicted, fig. 45, show fair agreement with the shapes observed. The predicted and observed strains once again deviate from one another.

Figures 47-49 show the response for a $[(90/0)_3]_s$ 12 in. arc length panel with a radius of 55.42 in. and no load offset while figs. 50-52 show the response of a very similar panel (55.34 in. radius) with a 15% load offset. For the midspan loading the correlation between theory and experiment is good, particularly for the load-displacement relation and the strains. Again there appeared to be some geometric imperfections present since limit point behavior, rather than bifurcation behavior, was observed for the specimen with no load offset. This was also born out by the observation of the equilibrium configurations during testing. The shapes observed were asymmetric in nature at much lower load levels than were predicted. In general, however, shape correlation was acceptable, as can be seen in fig. 48. The offset loading case also shows extraordinary agreement between theory and experiment. Load-deflection, load-thrust, shape, and the surface strain predictions correlate well with the observed results.

The results for a $[90/45/0/-45]_s$ 12 in. arc length panel, with a radius of 52.56 in. and a 15% load offset, test case 6, are shown in fig. 53-55. In order to theoretically predict the response of a quasi-isotropic composite, it was assumed that the response was one-dimensional and that the only nonzero curvature change was in the θ direc-

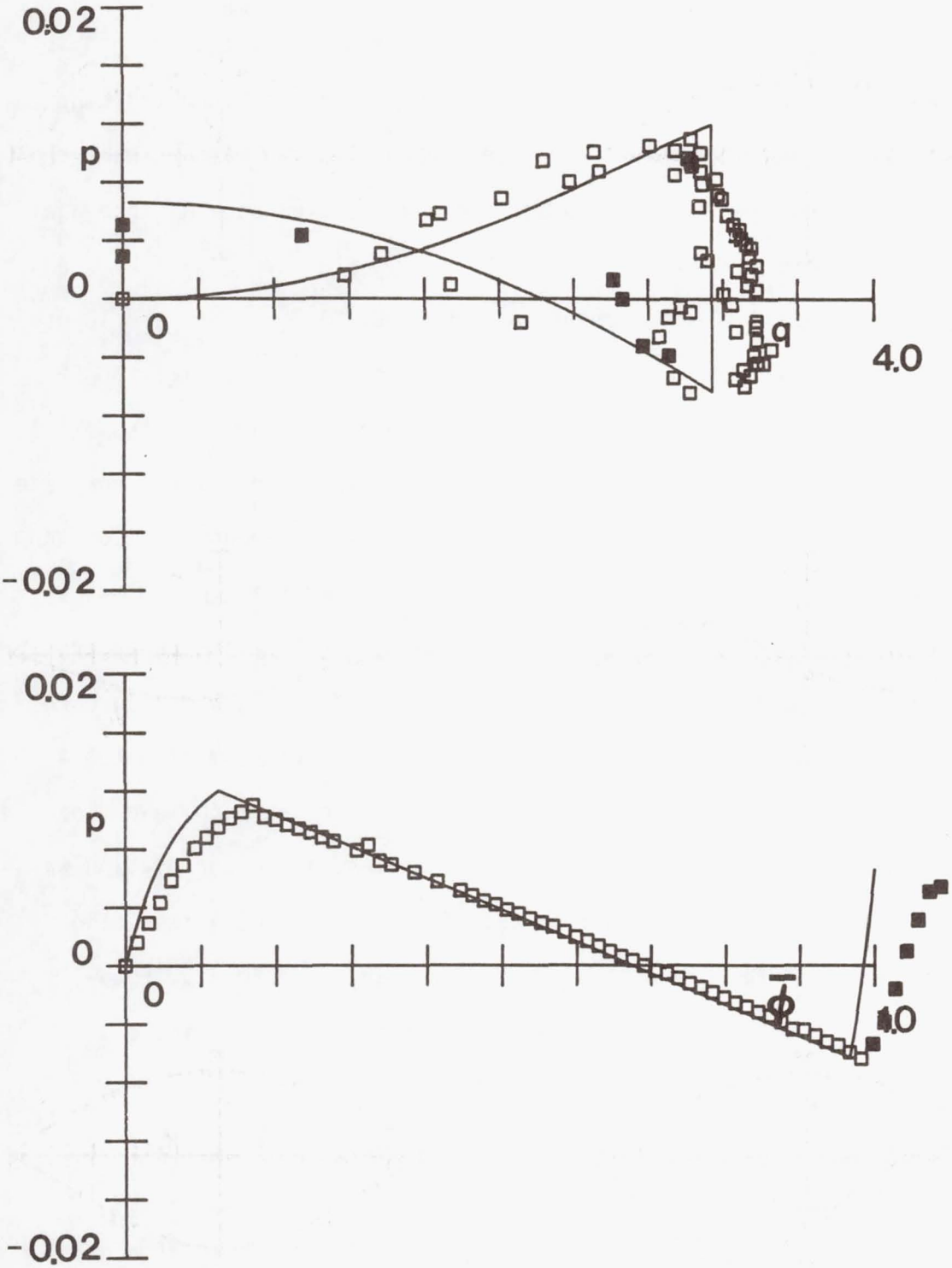

FIG. 47 COMPARISON OF THEORY AND EXPERIMENT: LOAD-THRUST AND LOAD-DISPLACEMENT RELATIONS; R=55.42, S=12.0, $\bar{\bar{\Gamma}}$=0.0, $[(90/0)_3]_S$

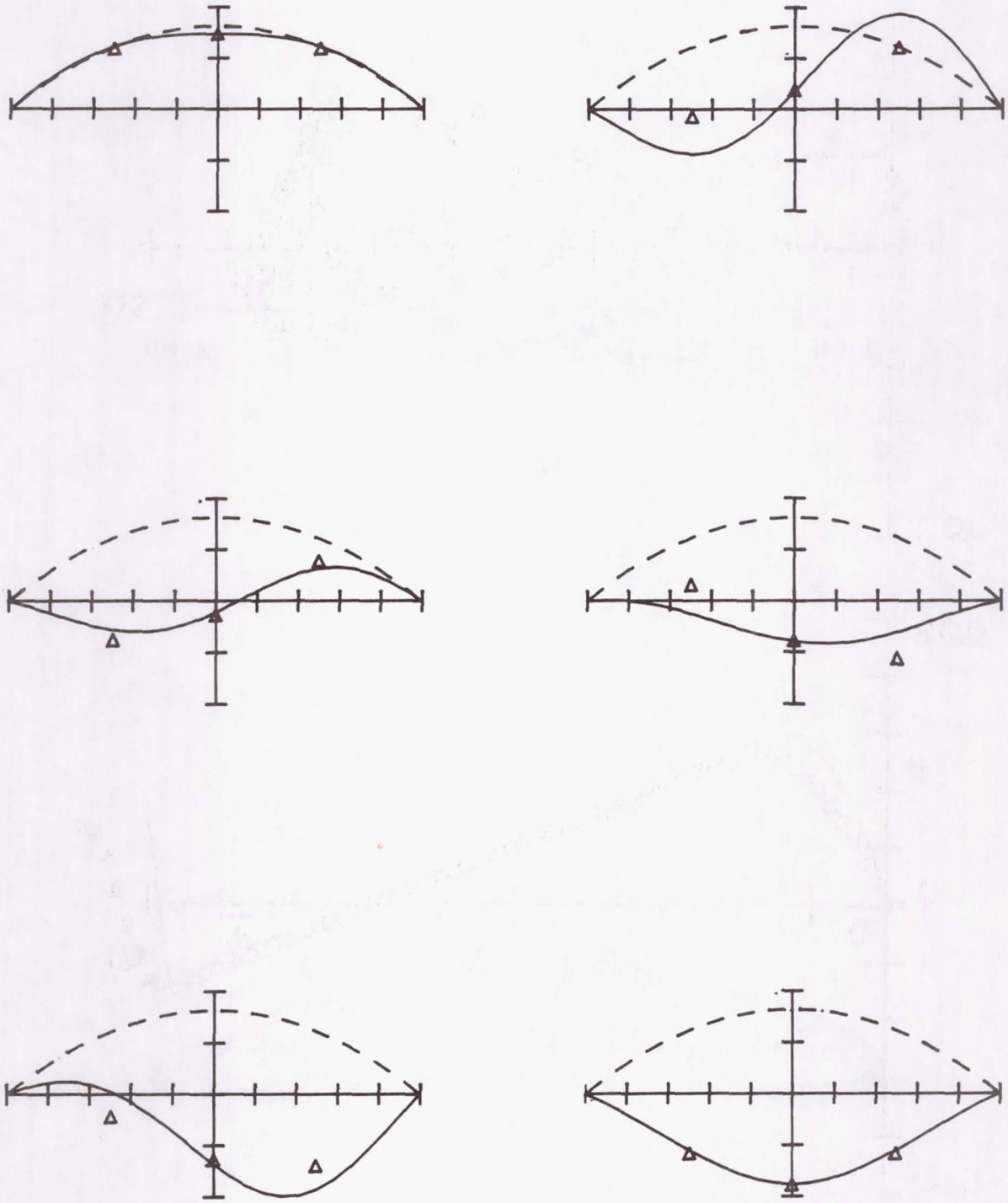

FIG. 48 COMPARISON OF THEORY AND EXPERIMENT: EQUILIBRIUM CONFIGURATIONS; R=55.42, S=12.0, $\overline{\Gamma}$=0.0, $[(90/0)_3]_S$

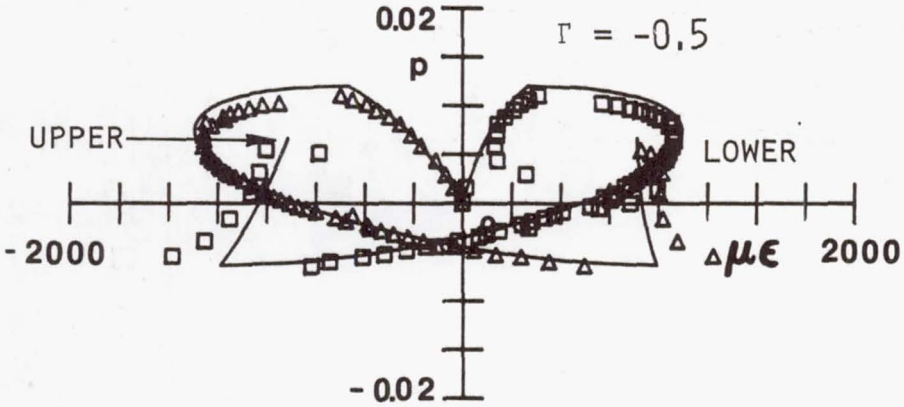

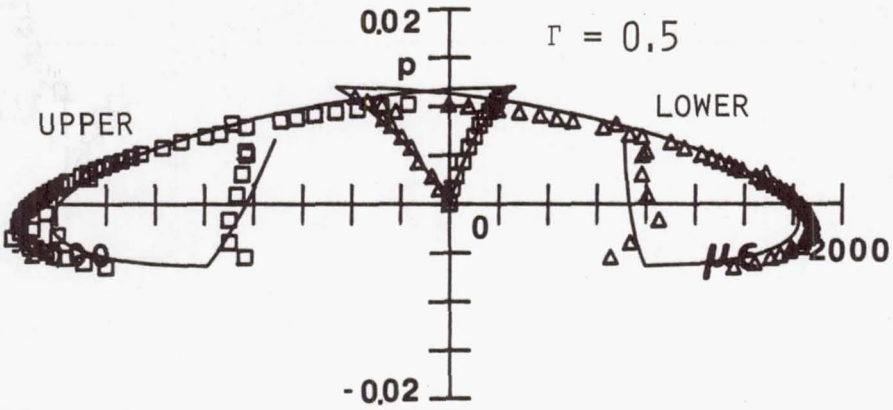

FIG. 49 COMPARISON OF THEORY AND EXPERIMENT: SURFACE STRAINS VS. APPLIED LOAD; R=55.42, S=12.0, $\bar{\Gamma}$=0.0, $[(90/0)_3]_S$

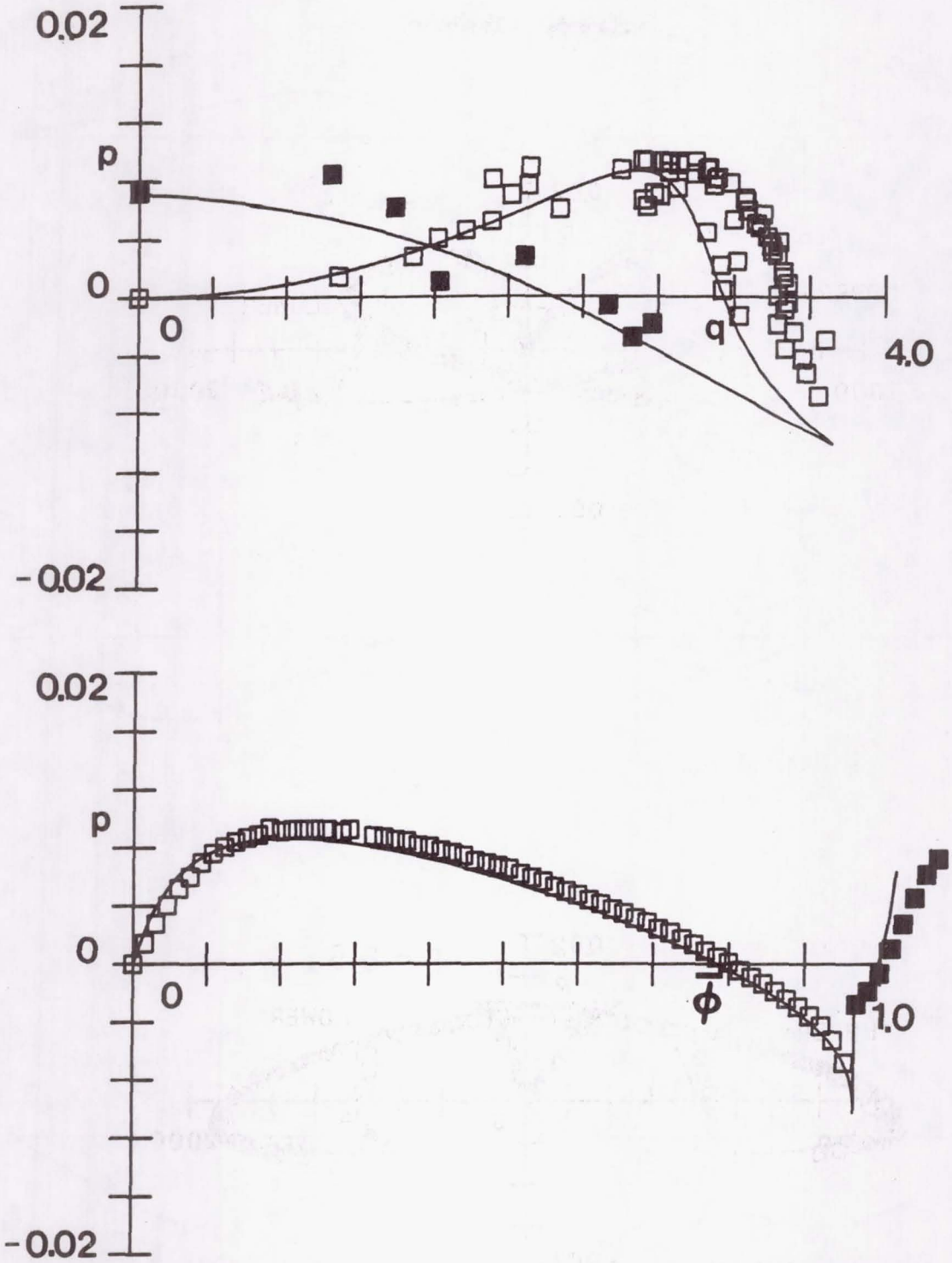

FIG. 50 COMPARISON OF THEORY AND EXPERIMENT: LOAD-THRUST AND LOAD-DISPLACEMENT RELATIONS; R=55.34, S=12.0, $\bar{\Gamma}$=0.15, $[(90/0)_3]_S$

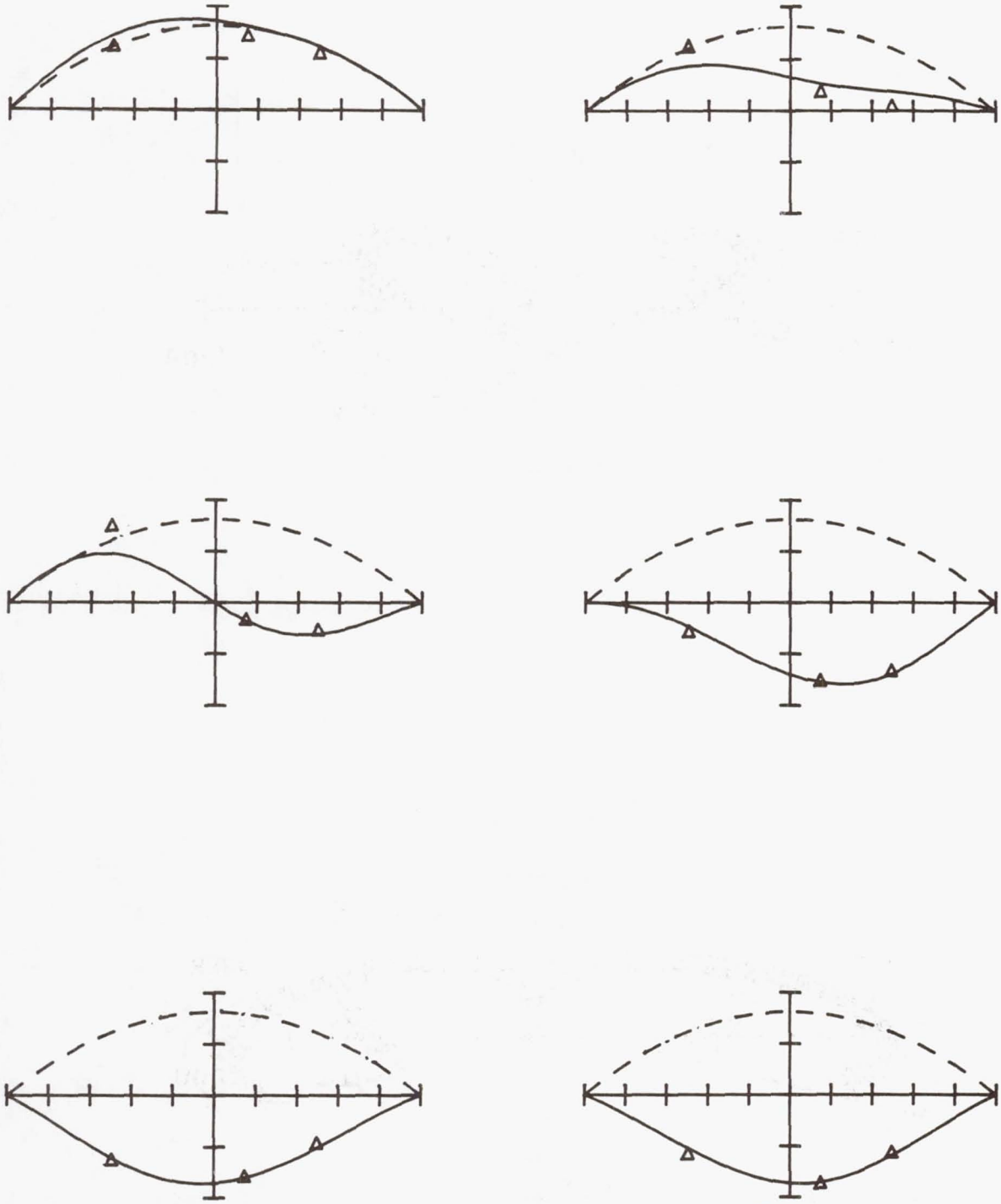

FIG. 51 COMPARISON OF THEORY AND EXPERIMENT: EQUILIBRIUM CONFIGURATIONS; R=55.34, S=12.0, $\overline{\Gamma}$=0.15, $[(90/0)_3]_S$

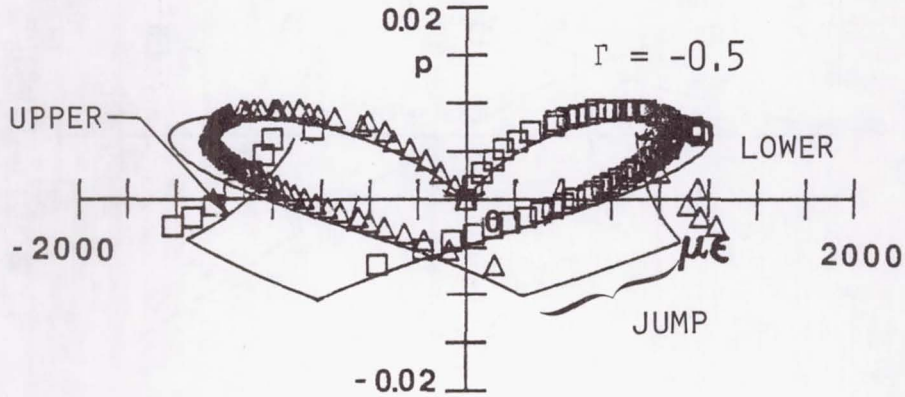

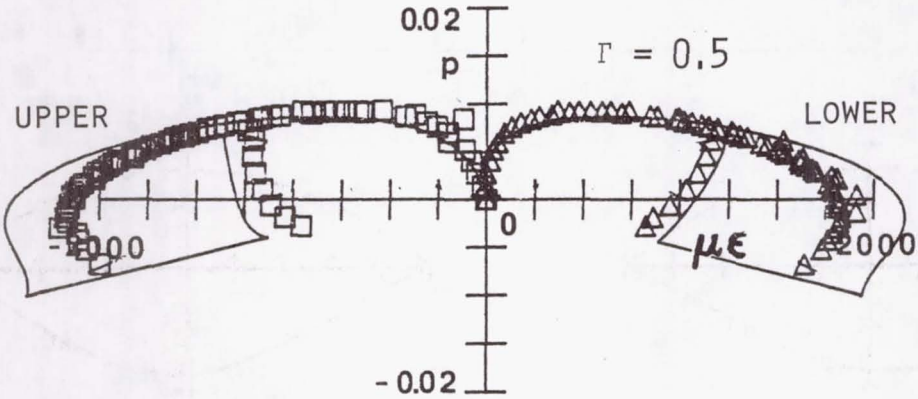

FIG. 52 COMPARISON OF THEORY AND EXPERIMENT: SURFACE STRAINS VS. APPLIED LOAD; R=55.34, S=12.0, $\bar{\Gamma}$=0.15, $[(90/0)_3]_S$

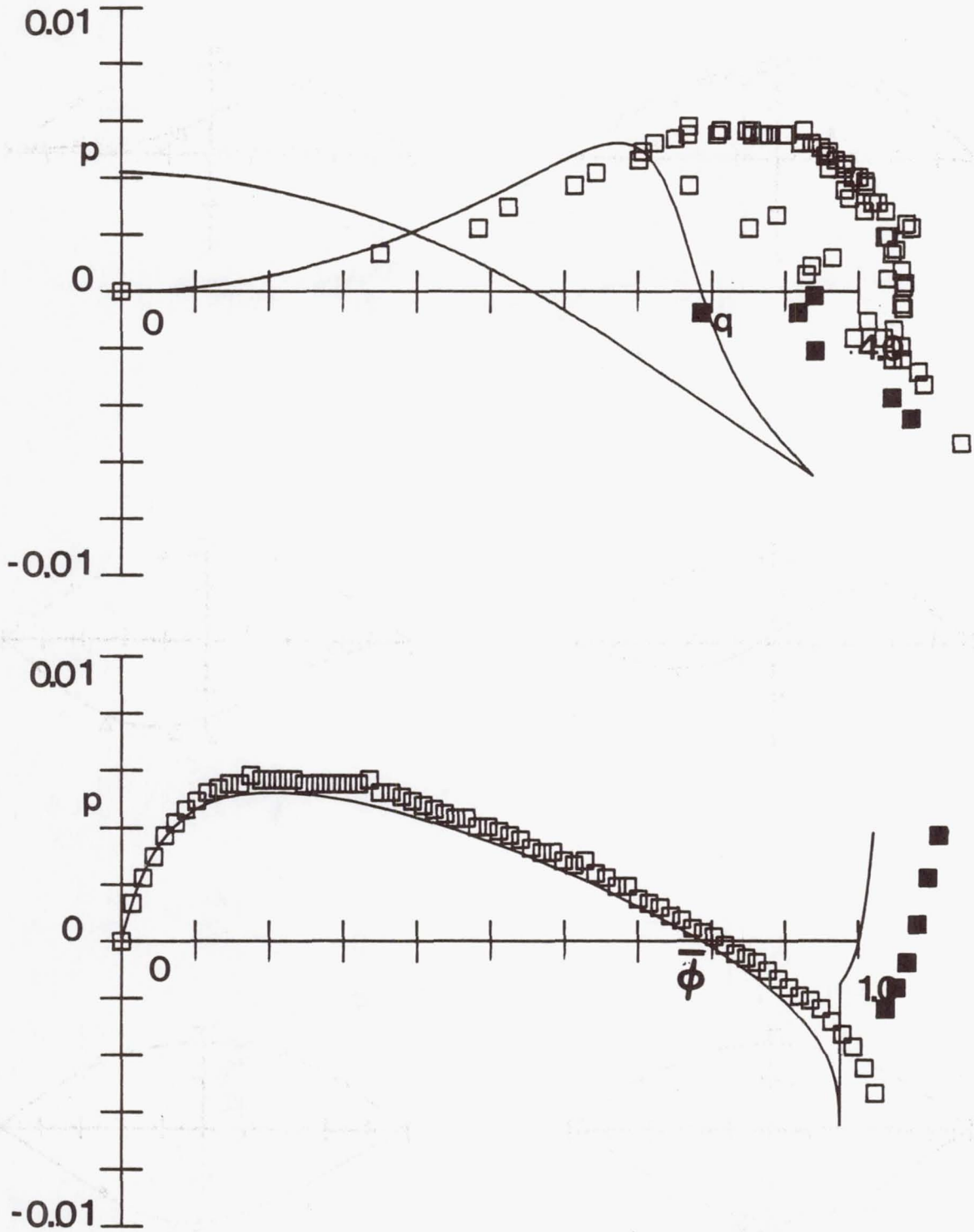

FIG. 53 COMPARISON OF THEORY AND EXPERIMENT: LOAD-THRUST AND LOAD-DISPLACEMENT RELATIONS; R=52.56, S=12.0, $\bar{\Gamma}$=0.15, $[90/45/0/-45]_s$

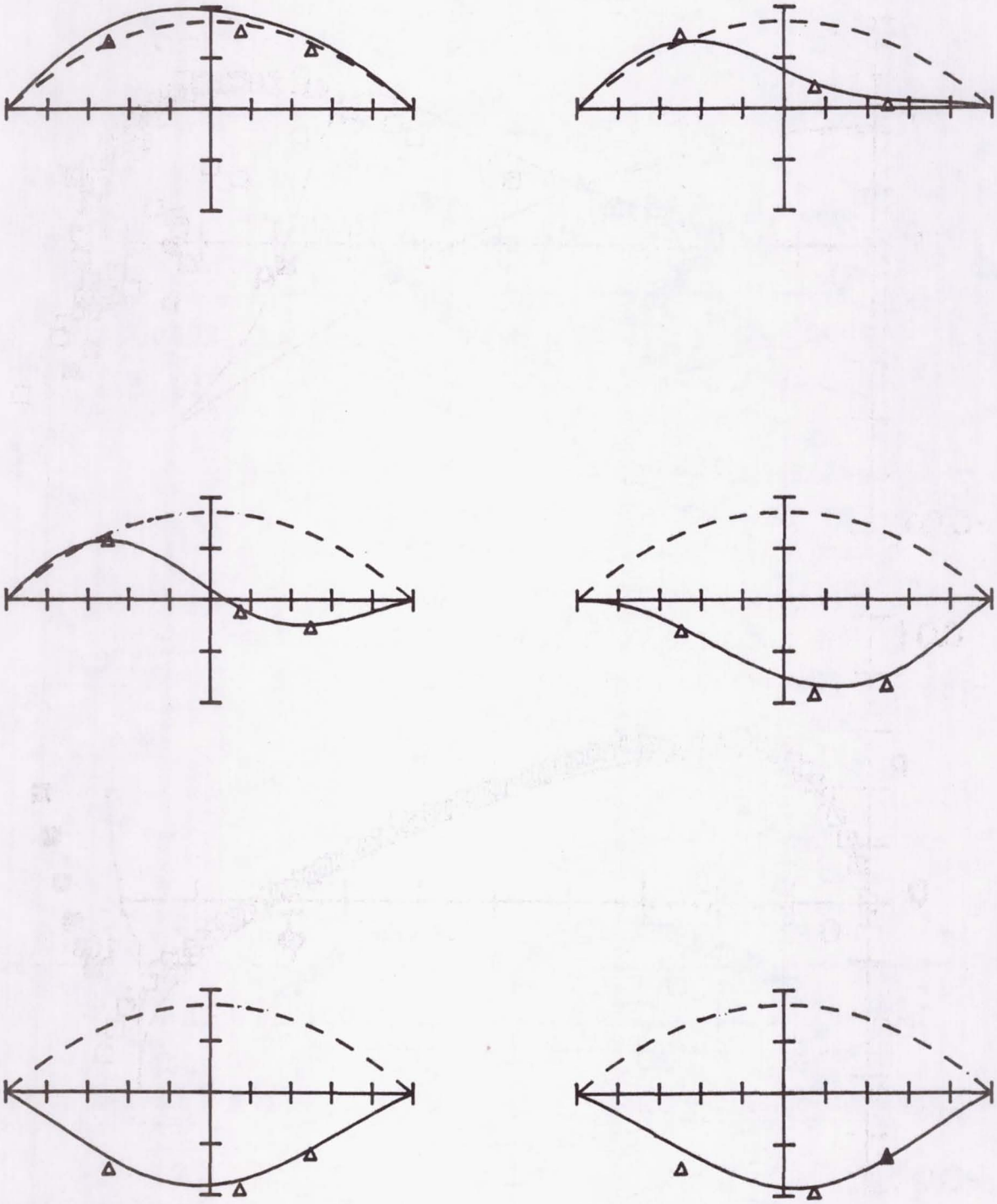

FIG. 54 COMPARISON OF THEORY AND EXPERIMENT: EQUILIBRIUM CONFIGURATIONS; R=52.56, S=12.0, $\overline{\Gamma}$=0.15, $[90/45/0/-45]_S$

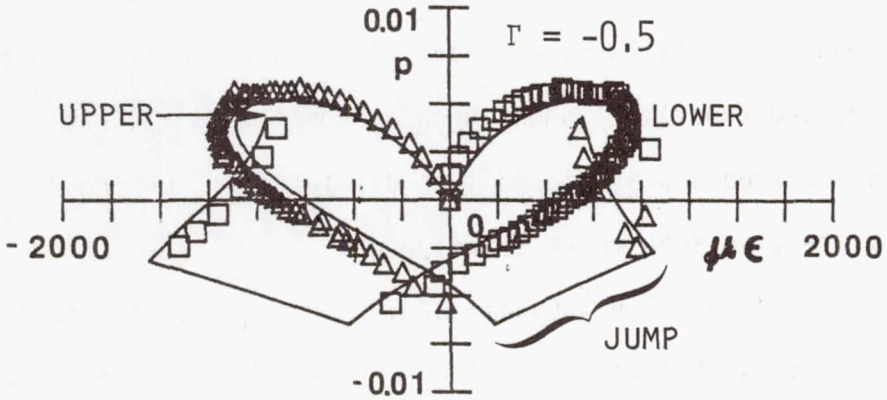

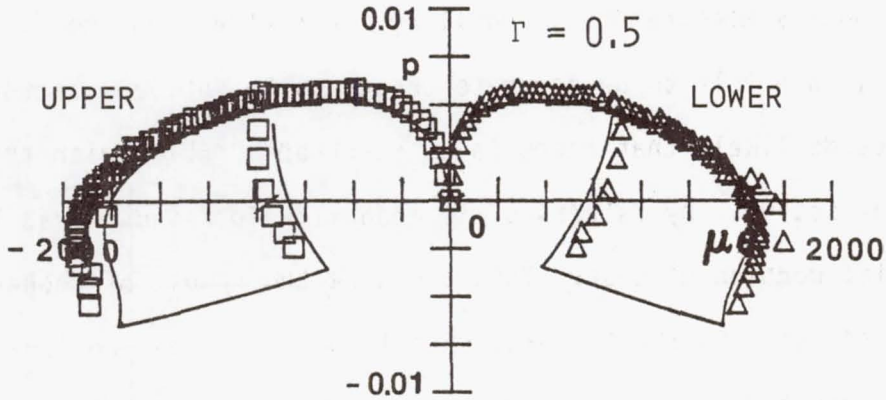

FIG. 55 COMPARISON OF THEORY AND EXPERIMENT: SURFACE STRAINS VS. APPLIED LOAD; R=52.56, S=12.0, $\bar{\Gamma}$=0.15, $[90/45/0/-45]_s$

tion. Thus a reduced bending stiffness was used. In reality, D_{16} and D_{26} being nonzero invalidate this assumption. Due to the constraint placed on the test specimen by the fixture it was thought that these one-dimensional assumptions were a good first approximation. A comparison of theory and experiment shows good agreement. The correlation between the observed and predicted load-displacement, deformed shapes, and strains are also seen to be quite good.

Figures 56-57 show the response of a $[(90/0)_4]_s$ 6 in. arc length panel with a radius of 64.7 and no load offset. This is case 7 and is the last case discussed here. The predicted response is limit point behavior but the observed response is that of monotonic behavior. The reason for this discrepancy between theory and experiment is not immediately obvious. Flexibility of the supports is not an issue here since the forces exerted on the support blocks are less than in previous cases. Error in the initial radius measurement has also been ruled out since it was double-checked and found to be correct. Also, the initial material property measurements, recalling their effect on the parameter λ, are felt to be accurate enough as to not be a factor here. It seems likely that there is a "start-up" problem with the experimental set-up. By "start-up" is meant low load and thrust levels, i.e., initial portion of test. This could be the result of mechanical slack or dead zones in the fixture. Recall that for the previous test cases there was a discrepancy between the predicted and observed initial stiffnesses. Appendix E ruled out the possibility of error in initial measurements as the cause of this discrepancy. Since the initial mid-

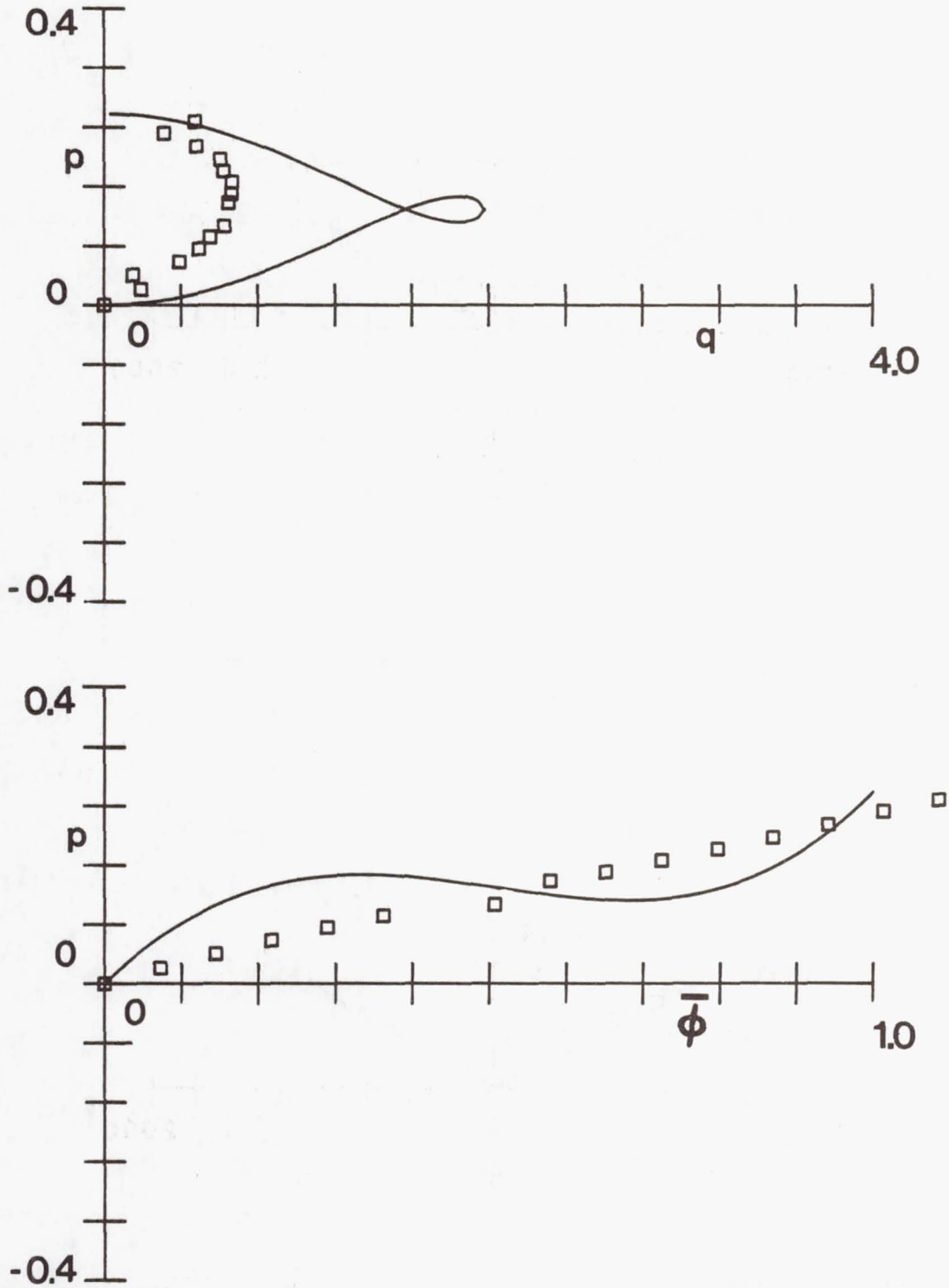

FIG. 56 COMPARISON OF THEORY AND EXPERIMENT: LOAD-THRUST AND LOAD-DISPLACEMENT RELATIONS; R=64.7, S=6.0, $\bar{\Gamma}$=0.0, $[(90/0)_4]_S$

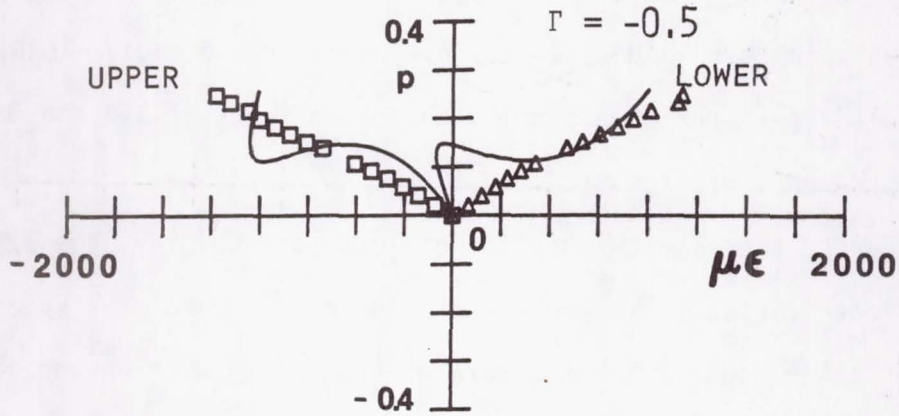

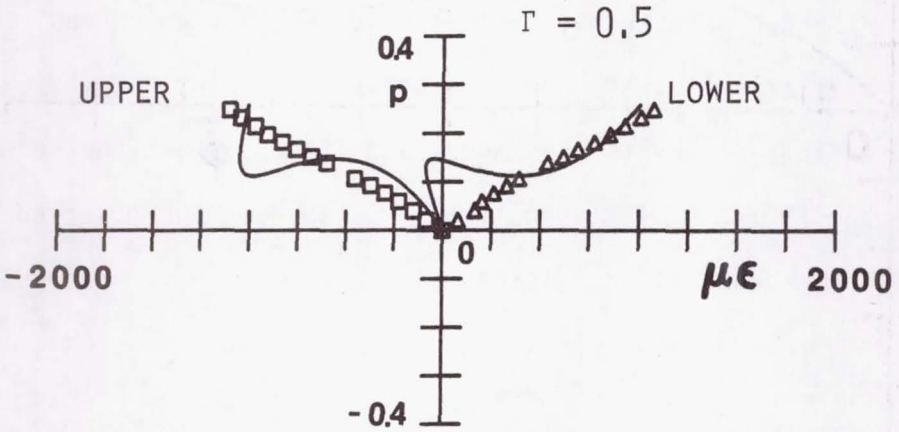

FIG. 57 COMPARISON OF THEORY AND EXPERIMENT: SURFACE STRAINS VS. APPLIED LOAD; R=64.7, S=6.0, $\bar{\Gamma}$ =0.0, $[(90/0)_4]_S$

span rise of the panel of test case 7 is significantly smaller than for the other test cases, it is possible that the start up problem effects a much greater portion of panel response, thus creating the poor correlation between prediction and observation. Whatever the cause, it was observed in tests of the same panel with load offsets of 15% and 30%. Thus the phenomenon was repeatable.

In order to address the question of load eccentricity, the limit point loads for the various load offsets for a given group of specimens, i.e., same lay-up and arc length, were plotted along with an upper and lower bound on the theoretical predictions. Here the upper bound corresponds to the curve for the panel with the smallest value of λ, while the lower bound corresponds to the curve for the panel with the largest value of λ. Since the radius of each panel within the group changes, it is necessary to plot the upper and lower bound. Figure 58 shows the plot of limit load vs. percent load offset for the $[(90/0)_4]_s$ 12 in. arc length specimens. From this figure it seems that the sensitivity to load eccentricities predicted is indeed close to that which was observed. Similarly fig. 59 shows the sensitivity plot for the $[(90/0)_3]_s$ 12 in. arc length specimens, and fig. 60 shows the sensitivity for the $[90/45/0/-45]_s$ specimens. It appears the observed sensitivity has been accurately predicted.

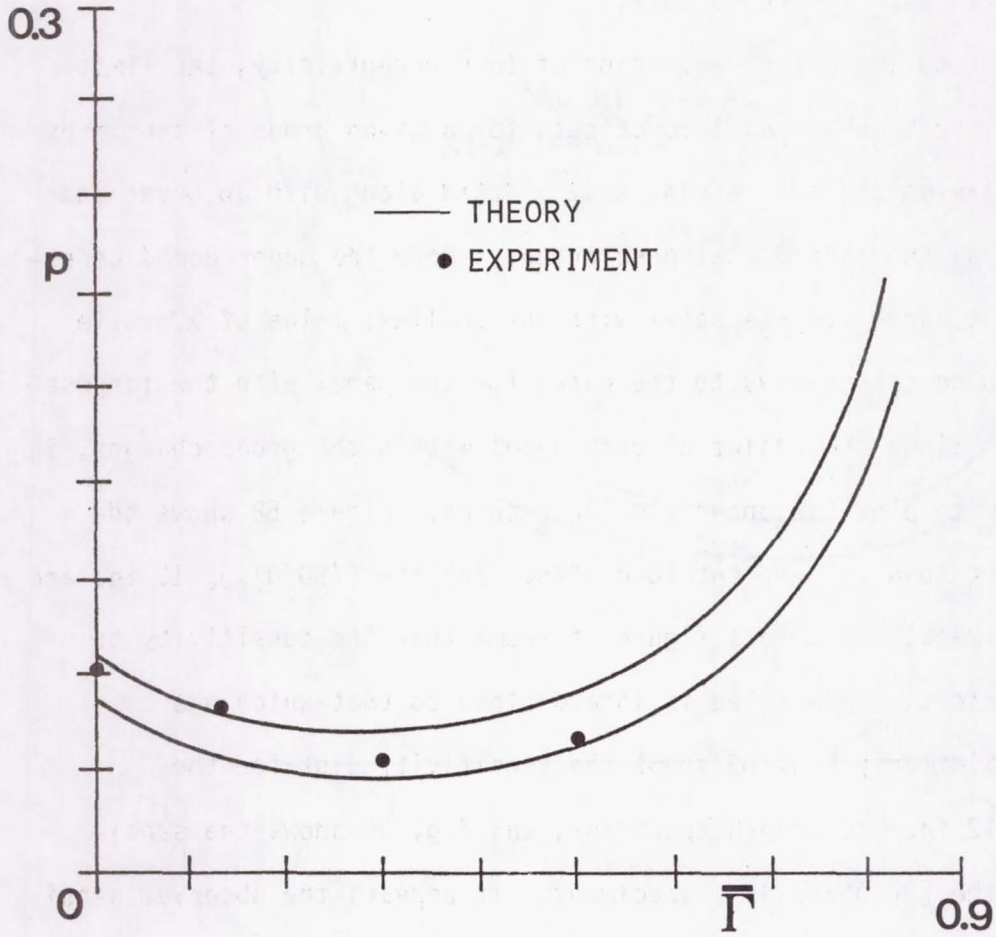

FIG. 58 COMPARISON OF THEORY AND EXPERIMENT: SENSITIVITY OF BUCKLING LOAD TO LOAD ECCENTRICITY, $[(90/0)_4]_S$ SPECIMEN GROUP

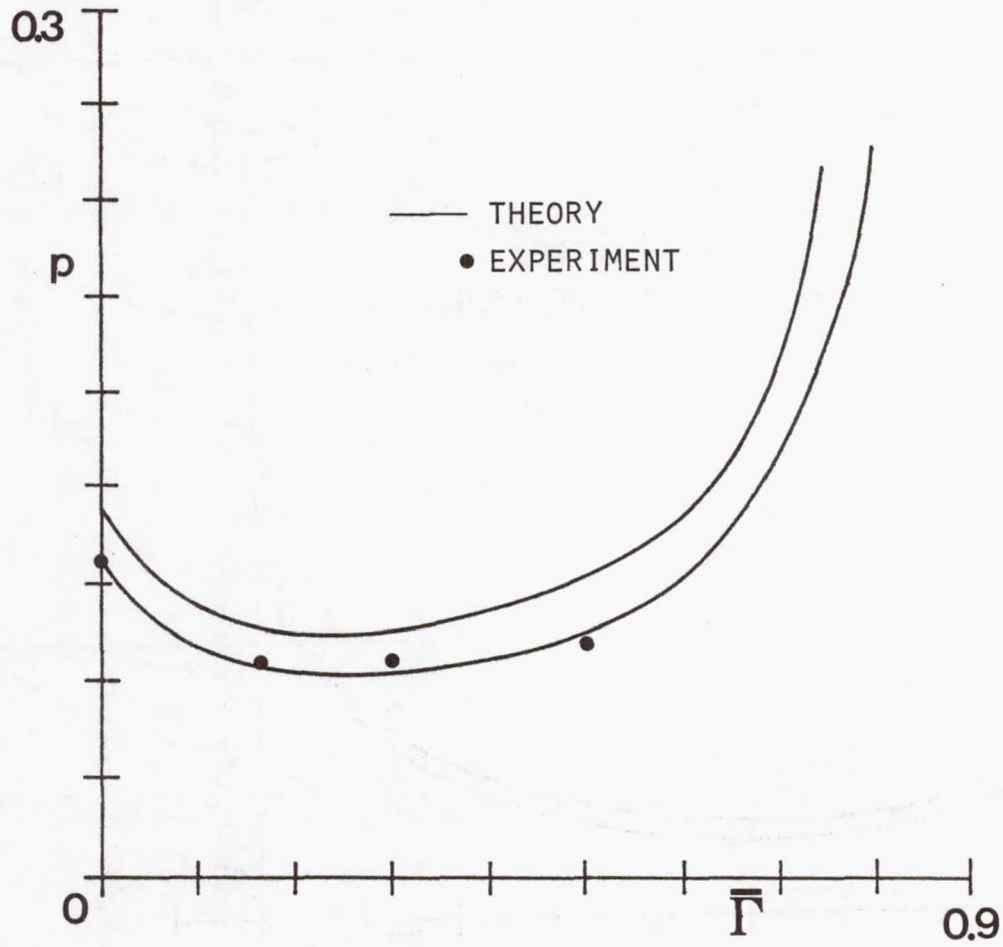

FIG. 59 COMPARISON OF THEORY AND EXPERIMENT: SENSITIVITY OF BUCKLING LOAD TO LOAD ECCENTRICITY, $[(90/0)_3]_S$ SPECIMEN GROUP

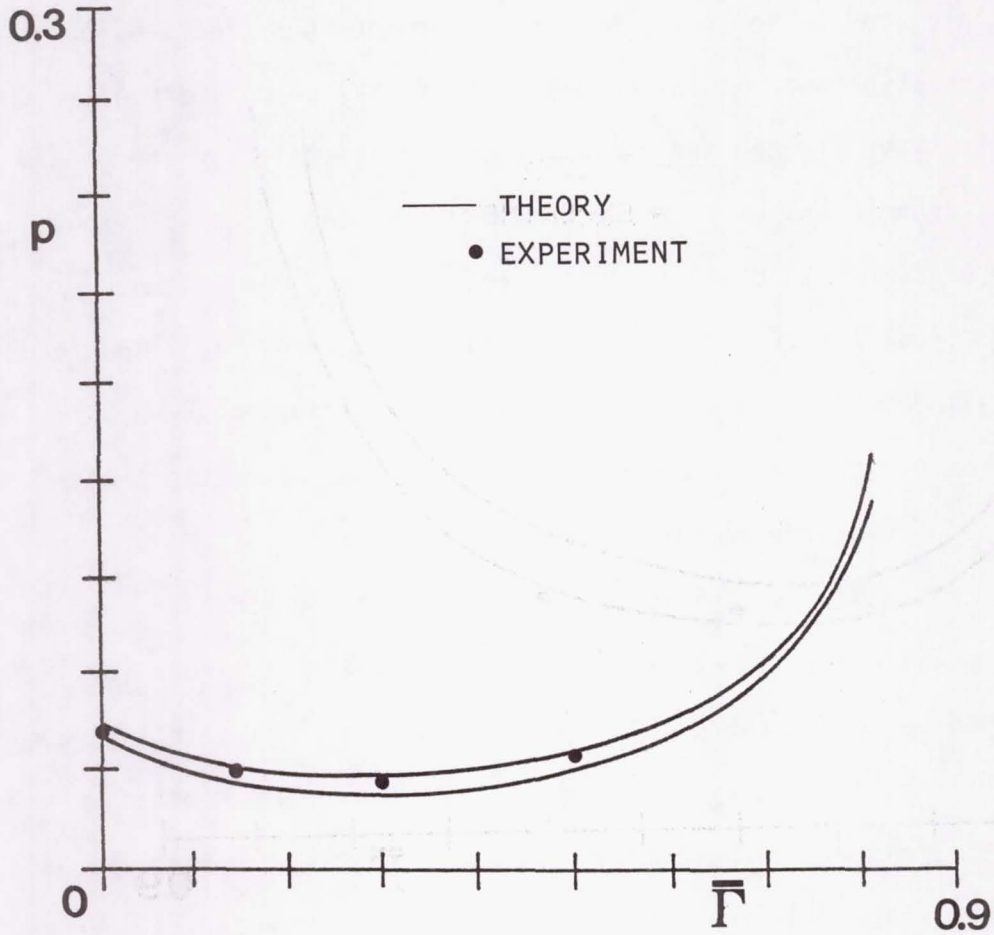

FIG. 60 COMPARISON OF THEORY AND EXPERIMENT: SENSITIVITY OF BUCKLING LOAD TO LOAD ECCENTRICITY, $[90/45/0/-45]_S$ SPECIMEN GROUP

Chapter 6

CONCLUSIONS AND RECOMMENDATIONS

The study presented in this thesis was intended to extend the knowledge of the static behavior of shallow orthotropic curved panels. The principle aims of the study were to determine the effects of orthotropic material properties on the behavior of shallow curved panels, to experimentally verify the analysis, and thus ultimately lay the ground work for a dynamic analysis of the same problem. An exact solution, taking into account load eccentricity, was developed for a simply supported circularly cylindrical curved panel subjected to a line load along a cylinder generator. Also, an experimental apparatus was designed to load the curved panels. The analytical predictions were compared with experimental measurements.

From this study the following conclusions may be made:

1. Analytically, three types of panel behavior were seen for panels loaded exactly at midspan; monotonic, limit point, and bifurcation. Only two types of behavior were exhibited when the load was offset; monotonic and limit point. The type of behavior predicted depends solely on one parameter, λ. Geometry, material properties, and stacking sequence influence λ for an orthotropic panel. For an isotropic panel λ is affected by geometry only.
2. Those panels which exhibit bifurcation behavior when loaded exactly at midspan were seen to be imperfection-sensitive. This was demonstrated both analytically and experimentally.

3. Initial geometric imperfections were detected and quantified while making initial radius measurements. Due to the imperfections present, inherent of any real structure, bifurcation behavior was not seen. However the observed response did closely approximate bifurcation behavior.
4. The overall correlation between theory and experiment was good. This implies that the solution method used is reasonably accurate. Predictions of the limit loads were quite accurate.
5. The predictions of strain in the panels were fair for the most part. However, a spanwise spatial variation in the middle surface strain was observed during testing. This is counter to the assumption that the strain was constant along the span.
6. Due to the small bending stiffness inherent to thin laminates, it was impossible to obtain accurate results for these laminates with the current experimental set-up. The friction-related moments generated at the ends of the simply supported panels at times caused these panels to behave as if they were clamped.
7. In analyzing the test results there seems to have been "start-up" or initial load and deformation problems with the experimental set-up. This is borne out by the lack of correlation between prediction and observation for the low thrust regimes. This would explain the discrepancies in initial stiffnesses as well as the total lack of correlation for test case 7 in which the maximum thrust was expected to be relatively small.

As a result of this work, a number of topics can be singled out for further investigations. Of these topics, a number are relatively minor extensions of the previous work. These are:

1. Modify the analysis to include different boundary conditions; e.g., frictional effects.
2. Include the effects of geometric imperfections in the analysis.
3. Conduct further static tests with various material properties and geometries. By varying the material properties the effects of orthotropicity described in this text may be experimentally verified.
4. Investigate the "start-up" problem encountered during testing.

In addition to the above, recommendations requiring significant extensions of this work are:

1. Extend the analysis to include the effects of shear deformation and to take into account angle ply laminates. This would allow a far greater number of laminates to be investigated and would perhaps be an intermediate step to the dynamic analysis.
2. Extend the analysis into the dynamic regime. Ultimately it is hoped that an understanding of the behavior of a composite fuselage, upon impacting a flat, rigid surface, may be obtained. By doing so the crashworthiness of a composite fuselage may be assessed.

References

1. Biezeno, C. B. and Grammel R., Engineering Dynamics, vol. 2, Blackie and Sons, London, 1956, pg. 397.

2. Fung, Y. C. and Kaplan, A., "Buckling of Low Arches or Curved Beams of Small Curvature," NACA, TN-2840, 1952.

3. Schreyer, H. L. and Masur, E. F., "Buckling of Shallow Arches," J. Engr. Mech. Div., ASCE, vol. 92, 1966, pg. 1.

4. Schreyer, H. L., "The Effect of Initial Imperfections on the Buckling Load of Shallow Circular Arches," J. Appl. Mech, vol. 39, 1972, pg. 445.

5. Plaut, R. H., "Influence of Load Position on the Stability of Shallow Arches," Z.A.M.P., vol. 30, 1979, pg. 548.

6. Cheung, M. C. and Babcock, C. D., "An Energy Approach to the Dynamic Stability of Arches," J. Appl. Mech., vol. 37, 1970, pg. 1012.

7. Nash, W. A. and Hsu, M. Y. H., "Stresses and Deflections in a Composite Material Arch," Proceedings of the 5th International Conference on Experimental Stress Analysis, ed. Prof. G. Bartolozzi; Udine, Italy, May 27-31, 1974, pg. 2.63.

8. Marshall, I. H., Rhodes, J., and Banks, W. M., "Experimental Snap-Buckling Behaviour of Thin GRP Curved Panels Under Lateral Loading," Composites, Vol. 8, No. 2, April 1977, pp 81-86.

9. Jones, R. M., Mechanics of Composite Materials, McGraw-Hill Book Co., New York, NY, 1975.

10. Boyce, W. E. and DiPrima, R. C., Elementary Differential Equations and Boundary Value Problems, J. Wiley, New York, NY, 1965.

11. Carper, D. M., Johnson, E. R., and Hyer, M. W., "The Response of Cylindrical Panels Fabricated from Symmetrically and Unsymmetrically Laminated Composite Materials," Virginia Polytechnic Institute and State University, VPI-E-83-14, April 1983.

Appendix A

COEFFICIENTS OF LOAD-THRUST RELATIONSHIPS

The solution technique applied to the governing differential equations discussed in Chapter 3 requires the solution of a quadratic equation. This equation relates either the applied load or a constant of the general solution of $\phi(\Gamma)$ to the thrust. Here the functional forms of the coefficients to the quadratic equation are presented. For each case the coefficients, found to be transcendental functions of the thrust, are found by substituting the functional form of the radial displacement into the integrated strain-displacement relationship, expressed nondimensionally by eq. 125.

<u>Midspan Loading: $q \neq 0$ and $q \neq \frac{n\pi}{2}$, $n = 1, 3, 5, \ldots$</u>

The load-thrust relationship is of the form,

$$A\xi^2 + B\xi + C = 0 \ , \tag{A1}$$

when $q \neq n\pi$, $n = 1, 2, 3, \ldots$. Here A, B, and C are,

$$A = \frac{3}{16q^4} + \frac{\tan^2(q)}{16q^4} - \frac{3\tan(q)}{16q^5} \tag{A2}$$

$$B = \frac{1}{2q^4}\left(\frac{1-\cos(q)}{\cos(q)}\right) - \frac{\tan(q)}{4q^3\cos(q)} \tag{A3}$$

$$C = \frac{q^2}{\lambda^4} - \frac{1}{6} + \frac{1}{4q^2\cos^2(q)} - \frac{\sin(2q)}{8q^3\cos^2(q)} \tag{A4}$$

When $q = n\pi$, $n = 1, 2, 3, \ldots$ the integrated strain-displacement relationship yields,

$$A\xi^2 + B\xi + C = Db^2. \tag{A5}$$

This relationship relates the applied load to the magnitude of the asymmetric displacement. The coefficients are,

$$A = -\frac{3}{16q^4} \tag{A6}$$

$$B = \frac{1}{2q^4}\left[1 - (-1)^n\right] \tag{A7}$$

$$C = \frac{1}{6} - \frac{q^2}{\lambda^4} - \frac{1}{4q^2} \tag{A8}$$

$$D = \frac{q^2}{4}. \tag{A9}$$

<u>Midspan Loading: $q = \frac{n\pi}{2}$, $n = 1, 3, 5, \ldots$</u>

The integrated strain-displacement relationship yields,

$$A(A_n^*)^2 + BA_n^* + C = 0, \tag{A10}$$

to determine a constant, A_n^*, from the general solution of $\phi_n(\Gamma)$ given by eq. 134. Here the coefficients are,

$$A = \frac{1}{4q^2} \tag{A11}$$

$$B = \frac{1}{q}(-1)^n \tag{A12}$$

$$C = \frac{q^2}{\lambda^4} - \frac{1}{6} + \frac{3}{4q^2} + \frac{1}{q^3}(-1)^n. \tag{A13}$$

<u>Eccentric Loading: $q \neq 0$ and $q \neq \frac{n\pi}{2}$, $n = 1, 2, 3, \ldots$</u>

The load-thrust relationship, when load eccentricity is present is,

$$A\xi^2 + B\xi + C = 0 . \tag{A14}$$

For the offset load case the coefficients of the quadratic equation are functions of the load offset as well as the thrust. The coefficients are:

$$\begin{aligned} A = {} & \frac{3}{16q^4} - \frac{(\overline{\Gamma})^2}{8q^4} - \frac{\overline{\Gamma}\sin(2q\overline{\Gamma})}{16q^4\sin(2q)} - \frac{\sin^2(2q\overline{\Gamma})}{16q^5\tan(2q)} \\ & + \frac{\cos^2(q\overline{\Gamma})\sin(2q)}{16q^5} + \frac{\sin^2(q\overline{\Gamma})}{4q^4\tan(2q)\sin(2q)} \\ & - \frac{3\cos^2(q\overline{\Gamma})\tan(q)}{16q^5} - \frac{\sin^2(2q\overline{\Gamma})\tan(q)}{16q^5} - \frac{\sin^4(q\overline{\Gamma})}{8q^5\tan(q)} \\ & + \frac{5\sin^2(q\overline{\Gamma})}{16q^5\tan(q)} \end{aligned} \tag{A15}$$

$$B = \frac{\Gamma^*\sin(q\Gamma)}{4q^3\cos(q)} - \frac{\tan q\cos(q\Gamma)}{4q^3\cos(q)} + \frac{\cos(q\Gamma)}{2q^4\cos(q)} - \frac{1}{2q^4} \tag{A16}$$

$$C = \frac{q^2}{\lambda^4} - \frac{1}{6} - \frac{\sin(2q)}{8q^3\cos^2(q)} + \frac{1}{4q^2\cos^2(q)} . \tag{A17}$$

Eccentric Loading: $q = \frac{n\pi}{2}$, $n = 1, 2, 3, \ldots$

For both odd and even values of n, the integrated strain-displacement relationship yields,

$$A(A_n^*)^2 + BA_n^* + C = 0. \tag{A18}$$

For odd values of n the coefficients are:

$$A = -\frac{q^2}{4} \tag{A19}$$

$$B = \frac{\cos^2(q\bar{\Gamma})}{q}(-1)^n(\bar{\Gamma} - 1) - \frac{\sin^2(q\bar{\Gamma})}{q}(-1)^n$$

$$+ \frac{1}{4q}(-1)^n[\cos(2q\bar{\Gamma}) - \cos(2q)] \tag{A20}$$

$$C = \frac{1}{6} - \frac{q^2}{\lambda^4} - \frac{1}{q} + \frac{3}{4q^2} + [(\bar{\Gamma})^2 + 1]\left[\frac{(-1)^n}{2q\cos(q\bar{\Gamma})}\right.$$

$$\left. - \frac{1}{2q^2} - \frac{\sin^2(q\bar{\Gamma})}{2q^2}\right] + [(\bar{\Gamma})^2 - 1](-1)^n$$

$$[\cos(q\bar{\Gamma}) + 1] + \frac{(\bar{\Gamma})^2\sin^4(q\bar{\Gamma})}{2q^2\cos^2(q\bar{\Gamma})}(-1)^n \tag{A21}$$

$$- \frac{\sin^4(q\bar{\Gamma})}{2q^2\cos^2(q\bar{\Gamma})} - \frac{\cos(q\bar{\Gamma})}{q^3}(-1)^n$$

$$- \frac{\bar{\Gamma}\sin(q\bar{\Gamma})}{q^2}(-1)^n - \frac{\sin^2(q\bar{\Gamma})}{q^3\cos(q\bar{\Gamma})}(-1)^n.$$

For even values of n the coefficients are:

$$A = -\frac{q^2}{4} \tag{A22}$$

$$B = 0 \tag{A23}$$

$$C = \frac{1}{6} - \frac{q^2}{\lambda^4} + \frac{3}{4q^2} \, . \tag{A24}$$

Appendix B

EFFECT OF ORTHOTROPY ON PANEL BEHAVIOR

The parameter λ is defined as,

$$\lambda^4 = \frac{A_{22}R^2\beta^4}{D_{22}}, \tag{B1}$$

where A_{22}, the extensional stiffness, and D_{22}, the bending stiffness, are given by,

$$A_{22} = \sum_{k=1}^{n} (\overline{Q}_{22})_k (z_k - z_{k-1}) \tag{B2}$$

$$D_{22} = \frac{1}{3} \sum_{k=1}^{n} (\overline{Q}_{22})_k (z_k^3 - z_{k-1}^3) . \tag{B3}$$

Concentrating on cross-ply laminates, where each lamina is composed of the same material, the reduced transformed stiffness is,

$$\overline{Q}_{22} = \begin{cases} Q_{22}, \text{ for } 0° \text{ laminae} \\ Q_{11}, \text{ for } 90° \text{ laminae.} \end{cases} \tag{B4}$$

The Q's are the reduced stiffness and are defined as,

$$Q_{22} = \frac{E_{22}}{1-\nu_{12}\nu_{21}} \tag{B5}$$

$$Q_{11} = \frac{E_{11}}{1-\nu_{12}\nu_{21}}, \tag{B6}$$

where E_{11} is the Young's modulus in the fiber direction and E_{22} is the Young's modulus perpendicular to the fiber direction. By definition it is assumed that $E_{11} > E_{22}$.

Using the above definitions for the stiffnesses, a general expression for the extensional stiffness and the bending stiffness can be developed in terms of the number of laminae, the stacking sequences, and the elastic moduli of the laminae. For convenience these expressions are shown only for the $[(90/0)_n]_s$ family of laminates. For these laminates, the extensional and bending stiffnesses are,

$$A_{22} = \frac{\frac{Nt}{2}(E_{11} + E_{22})}{1-\nu_{12}\nu_{21}} \tag{B7}$$

$$D_{22} = \frac{\frac{N^2t^3}{24}\left[(N+3)E_{11} + (N-3)E_{22}\right]}{1 - \nu_{12}\nu_{21}}, \tag{B8}$$

where N is the number of laminae (N=4n) and t is the thickness of each lamina. Substituting eqs. B7 and B8 into eq. B1 yields,

$$\lambda^4 = \frac{3\left(1 + \frac{E_{11}}{E_{22}}\right) S^4}{4N^2t^2\left[\left(1 + \frac{3}{N}\right)\frac{E_{11}}{E_{22}} + \left(1 - \frac{3}{N}\right)\right] R^2}, \tag{B9}$$

where use is made of the fact $S = 2R\beta$.

To emphasize the importance of taking the orthotropy of the material into account, three shallow circularly cylindrical panels are com-

pared as to the behavior exhibited. Each panel is assumed to have the same geometry, only the material used in the fabrication of the panels is varied. For the comparison aluminum, glass-epoxy, and graphite-epoxy panels are used. Table B1 summarizes the geometry, material properties, and calculated values of λ for each of the panels. The value of λ for the aluminum panel is such that bifurcation on the primary equilibrium path would occur when the panel is loaded exactly at midspan. However, when glass-epoxy or graphite-epoxy is used, limit point behavior would be expected. Thus by increasing the degree of orthotropy, the panel behavior changes from bifurcation, where a asymetric response would be expected when in displacement control, to limit point behavior, where a jump in load and thrust would occur.

For a composite material, the number of laminae, as well as the degree of orthotropy, effect the value of λ. Figure B1 shows the effect of the number of laminae, as well as the degree of orthotropy present, on the calculated value of λ. With an increasing number of laminae, the effect of orthotropy becomes less pronounced.

Stacking arrangement, though not explored specifically here, could be important in determining λ and thus panel response. Though they would have the same weight, two panels each with 16 laminae could be made to behave quite differently, depending on how the laminae are arranged.

Table B1

Panel Geometries and Material Properties

	Panel		
	Aluminum	Glass-Epoxy	Graphite-Epoxy
Arc Length (in.)	6	6	6
Radius (in.)	45	45	45
Thickness (in.)	0.08	0.08	0.08
Lay up	---	$[90_4/0_4]_s$	$[90_4/0_4]_s$
E_{11} (psi)	10×10^6	7.8×10^6	25×10^6
E_{22} (psi)	10×10^6	2.6×10^6	1×10^6
E_{11}/E_{22}	1.0	3.0	25.0
λ	2.94	2.72	2.58

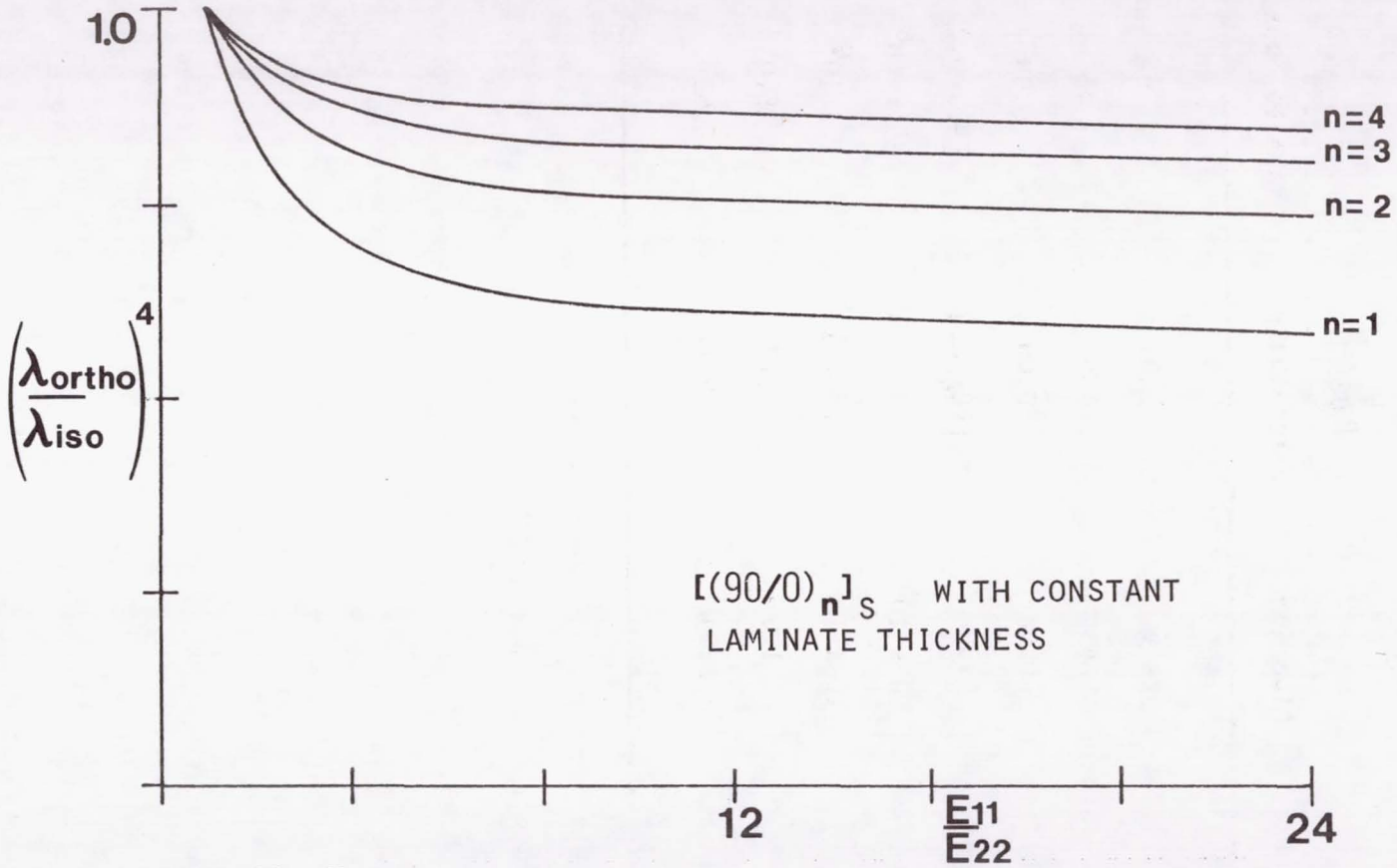

FIG. B1 EFFECT OF ORTHOTROPY AND LAY-UP ON PANEL RESPONSE

Appendix C

DETERMINATION OF EXTENSIONAL STIFFNESS AND BENDING STIFFNESS

As mentioned in Chapter 4, the initial measurements made on the test specimens included the determination of the extensional and bending stiffnesses. To accurately compare the results of the analysis and the experiment it is necessary to have correct material properties to input into the analysis. Here the test set-ups and procedures used for the measurement of both the extensional stiffness and bending stiffness are described.

Extensional Stiffness

The extensional stiffnesses for each layup were obtained from tensile test data. A tensile test specimen was machined from each of the large panels, as were the curved panel test specimens. The tensile coupon, 0.5 x 12 in., was cut from the panel such that the stiffness in the x direction was actually measured. Since the specimens were cross-ply laminates, the stiffnesses in the x direction and θ direction should have been equal. The specimens were tested in the Instron Tensile Machine using an Instron load cell to measure applied load. Back-to-back strain gages were mounted at the center of the gage section. The strain gages used were 120 ohm gages with approximately 4 feet of lead wire. The excitation voltage for the strain gages was 2 volts. The strain gage and load data were acquired by using a digital data acquisition system. For each test performed the slope of the load vs. strain curve was calculated using a least squares curve fit. This slope,

proportional to the laminate Young's modulus in the x direction, was then divided by the width of the tensile specimen to obtain the extensional stiffness. Each test was performed twice in order to obtain results as accurately as possible. The results for the layups investigated are summarized in Table C1.

Bending Stiffness

The bending stiffnesses for each of the curved panel specimens tested were obtained by performing three-point bend tests on the specimens themselves. The specimens were placed on the fixture so that the panel was simply supported, restricting end displacement in the vertical direction while allowing freedom to displace horizontally. The load was applied through a hanger located at midspan to which calibrated dead weights were attached. A schematic of the test fixture used for the three-point bend tests is shown in fig. C1. A dial gage capable of resolving displacements to 0.001 in. was used to measure the vertical displacement at midspan. Load vs. displacement data was recorded and the slope determined using a least-squares fit to the data. Assuming a linear straight beam theory was suitable for describing the behavior of the bend specimen, the bending stiffness was obtained from the expression,

$$D_{22} = \frac{pL^3}{48w} \tag{C1}$$

Table C1

Measured Panel Stiffnesses

Test No.	Lay-up	A_{22} (lb/in)	D_{22} (lb-in)
1	$[(90/0)_4]_s$	7.8194×10^5	616.2
2	$[(90/0)_4]_s$	7.8194×10^5	606.3
3	$[(90/0)_4]_s$	7.8194×10^5	617.2
4	$[(90/0)_4]_s$	7.8194×10^5	612.7
5	$[(90/0)_3]_s$	5.85×10^5	263.5
6	$[(90/0)_3]_s$	5.85×10^5	265.4
7	$[(90/0)_3]_s$	5.85×10^5	268.2
8	$[(90/0)_3]_s$	5.85×10^5	260.1
9	$[90/45/0/-45]_s$	3.175×10^5	90.9
10	$[90/45/0/-45]_s$	3.175×10^5	90.5
11	$[90/45/0/-45]_s$	3.175×10^5	93.3
12	$[(90/0)_4]_s$	7.8194×10^5	613.5
13	$[(90/0)_4]_s$	7.8194×10^5	609.8
14	$[(90/0)_4]_s$	7.8194×10^5	614.2
15	$[90/0]_s$	2.21×10^5	12.36
16	$[90/0]_s$	2.21×10^5	12.70
17	$[90/0]_s$	2.21×10^5	12.30
18	$[90/0]_s$	2.21×10^5	12.51

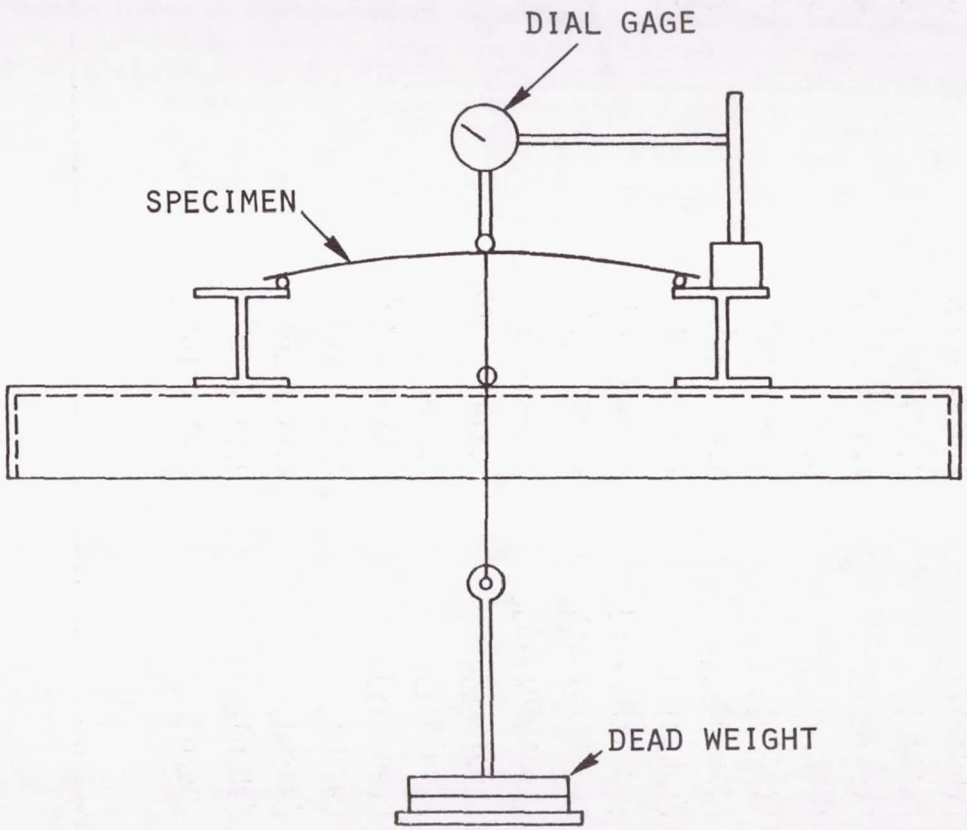

FIG. C1 THREE-POINT BEND TEST FIXTURE

where p is the load intensity, w is the midspan displacement and L is the span between supports. The results of the three-point bend tests are summarized in Table C1.

Appendix D

EFFECT OF GEOMETRIC IMPERFECTIONS ON PANEL BEHAVIOR

As was mentioned earlier, Schreyer [4] found the effects of geometric imperfections on the behavior of isotropic curved panels to be qualitatively the same as the effects of load offsets. The geometric imperfections investigated in Schreyer's study were of the same form as the asymmetric deformation mode of the curved panels. In the present study it was thought that similar geometric imperfections were partially responsible for some of the deviation between theoretical and experimental results given in Chapter 5. Since the location of the holes drilled into the panel for locating the loading head were measured and felt to be accurately centered, load eccentricity was not felt to be a problem.

Figures 38-40 show the predicted and observed response for a $[(90/0)_4]_s$ composite specimen with no load offset. The behavior expected of this panel was bifurcation behavior. While the load-displacement diagram of fig. 38 appears to show bifurcation behavior, the load-thrust diagram leads one to believe that some imperfection may be present. For this test case a number of measurements were made along the entire span of the specimen for determining the average radius. (For subsequent tests these measurements were made only over half the span.) From these measurements it was possible to determine the deviation of the initial configuration from the assumed perfect cylindrical configuration.

Figure D1 shows the measured deviation of the initial configuration from a perfect cylindrical geometry. The perfect configuration, $y_0(x)$,

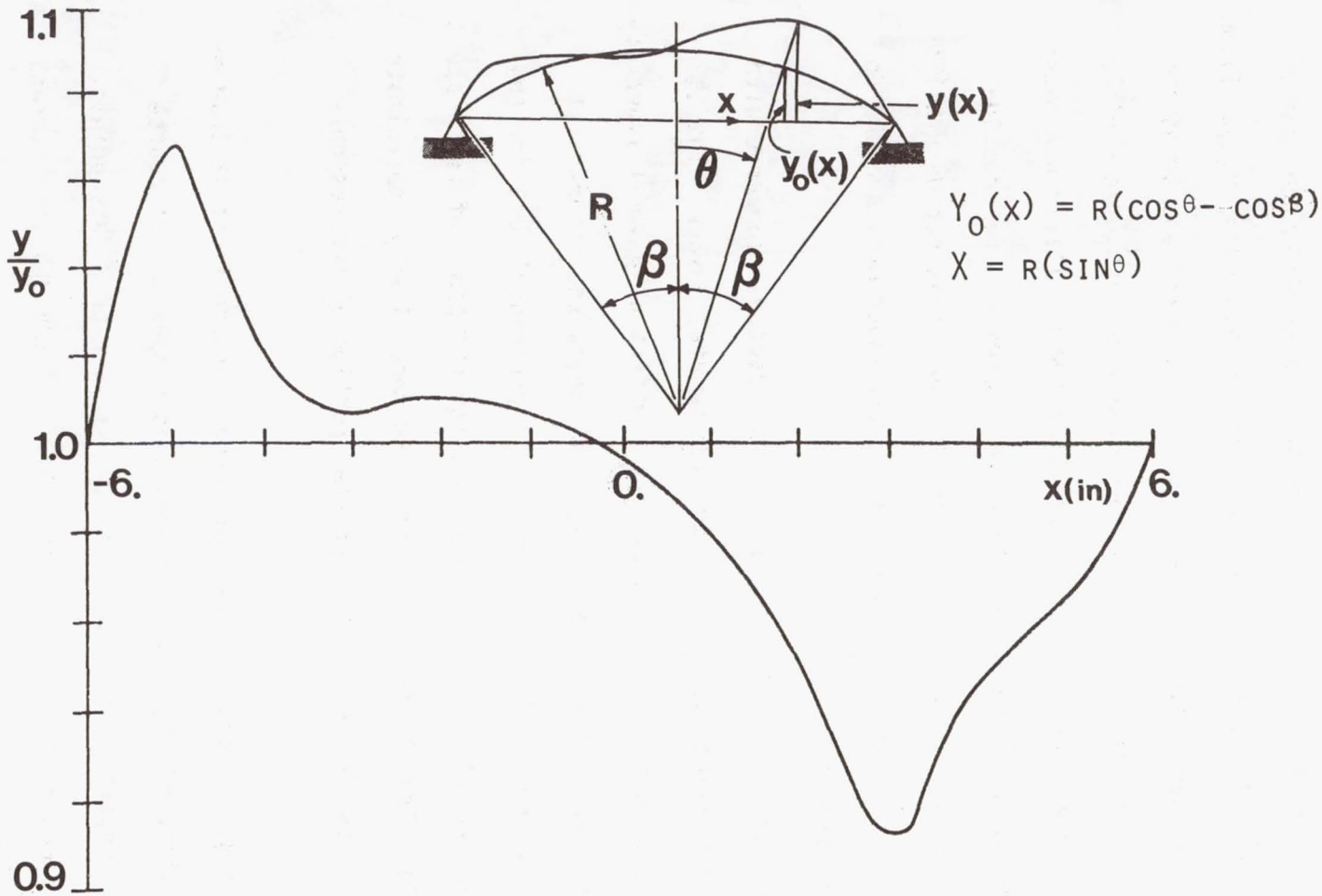

FIG. D1 MEASURED INITIAL GEOMETRIC IMPERFECTION

is assumed to be a cylinder with a radius of curvature, $\frac{1}{R}$, which is determined by a least-squares fit of the data taken along the span of the curved panel. The measured configuration is denoted by $y(x)$. From this figure it is seen that the deviation, or imperfection, tends to take on the form of the asymmetric deformation mode discussed earlier. Since geometric imperfections were found from the initial measurements and were found to be of the same form as the asymmetric deformation mode, as was the case in Schreyer's work, it was a distinct possibility that some of the differences between theory and experiment are due to these imperfections.

To explore this point further a 5% load offset was compared with the theoretical midspan loading and the experimental points. The 5% load offset was used to show the qualitative effect of a small imperfection in the initial configuration. Figure D2 shows the theoretical curves, both a 0% and a 5% load offset, and experimental data for the load-thrust and load-displacement relations for the panel of test case 1 (see Chapter 5). The 5% offset case tends to more closely approximate the data taken from the test over a greater portion of the response curves.

Finally, fig. D3 shows the spatial shapes for the first 18 load or displacement points of fig. D2. The predicted shapes are of course symmetric with respect to midspan. For the first 6 or 7 data points, the measured shapes are also symmetric. However, the 8th point shows that the actual shape has lost symmetry, the left side deflecting more than the right side. At points 13 and 14 the asymmetry has shifted, the

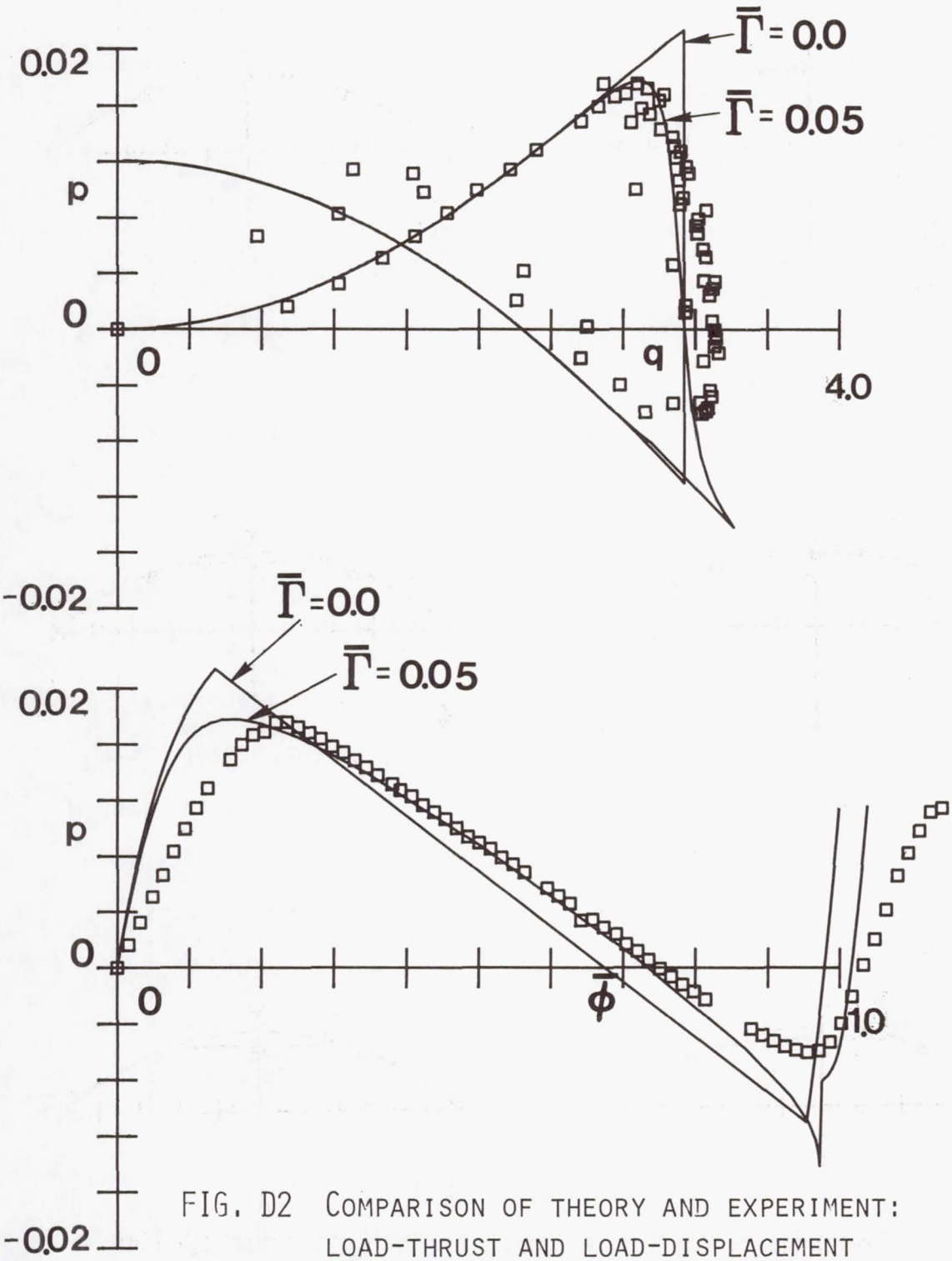

FIG. D2 COMPARISON OF THEORY AND EXPERIMENT: LOAD-THRUST AND LOAD-DISPLACEMENT RELATIONS; R=56.34, S=12.0, $\bar{\Gamma}$=0.0 AND $\bar{\Gamma}$=0.05, $[(90/0)_4]_S$

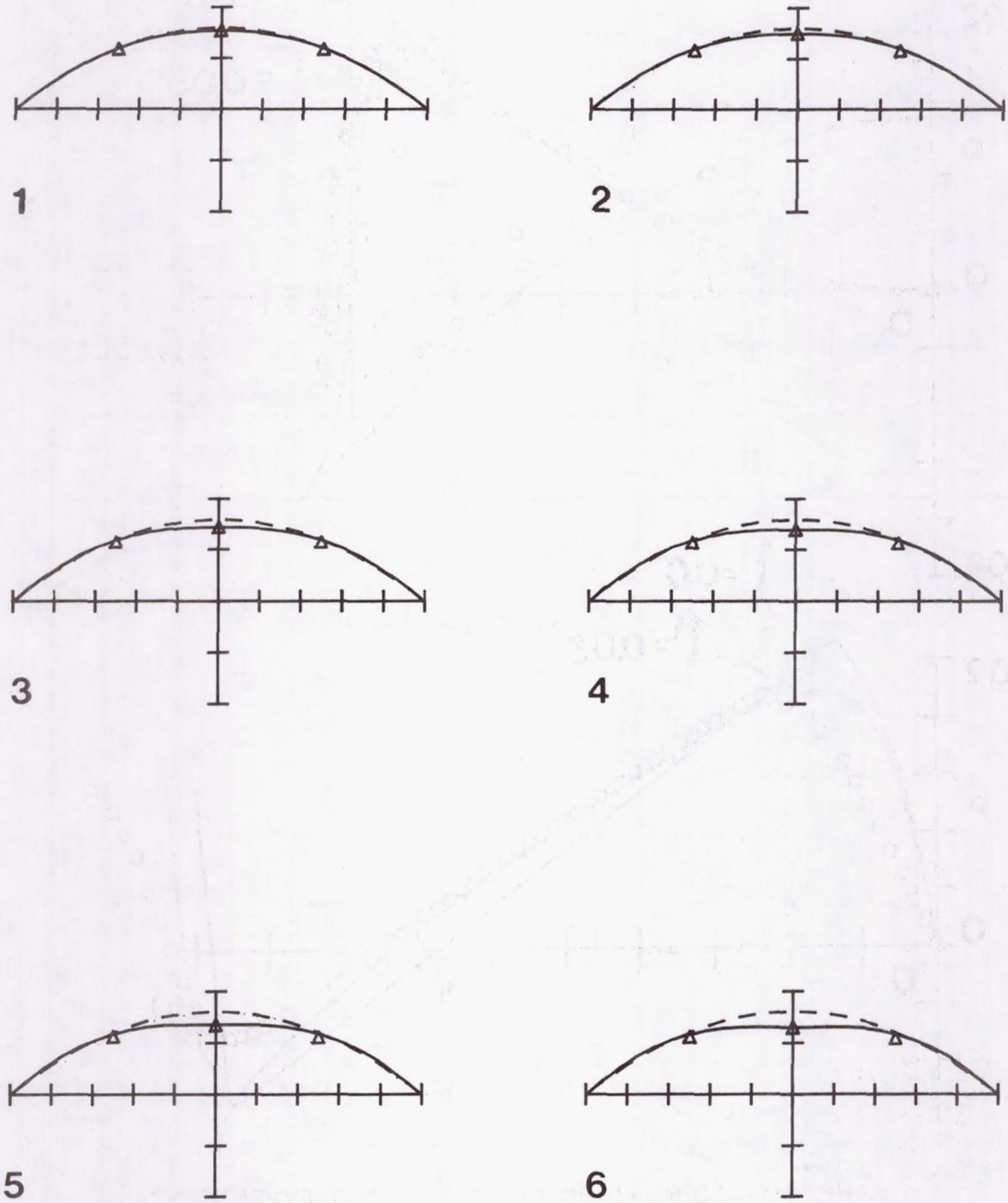

FIG. D3 COMPARISON OF THEORY AND EXPERIMENT: EQUILIBRIUM CONFIGURATIONS; R=56.34, S=12.0, $\bar{\Gamma}$ =0.0, $[(90,0)_4]_S$

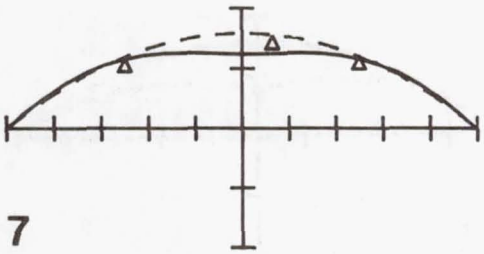

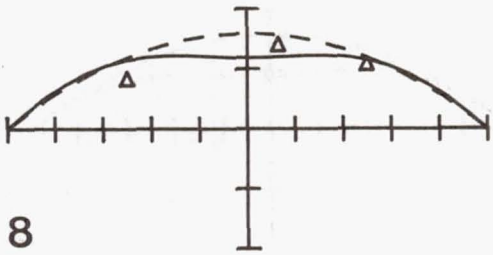

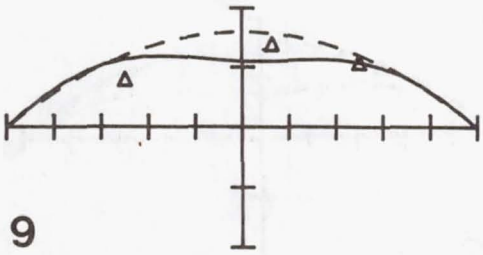

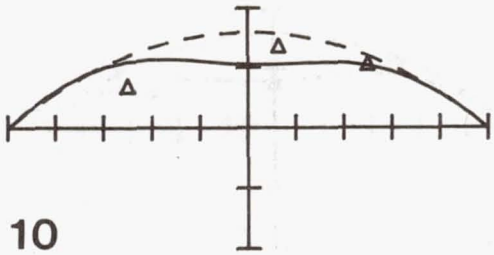

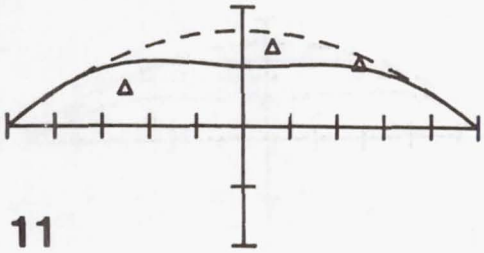

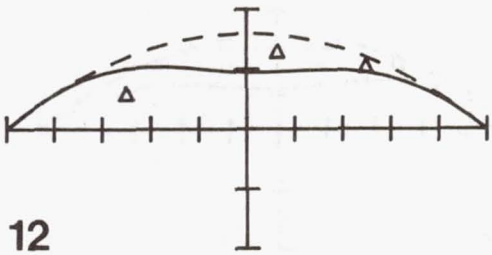

FIG. D3 (CONT.)

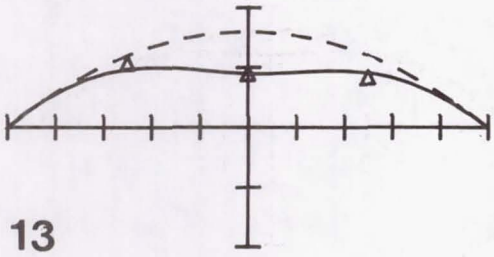

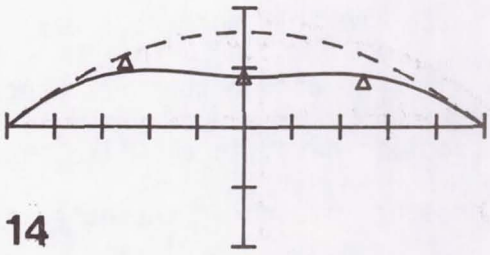

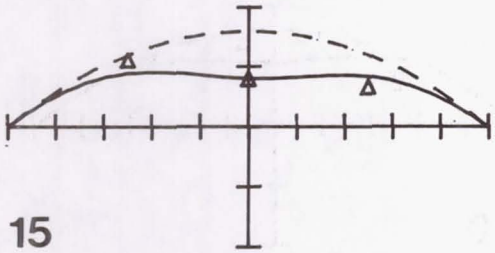

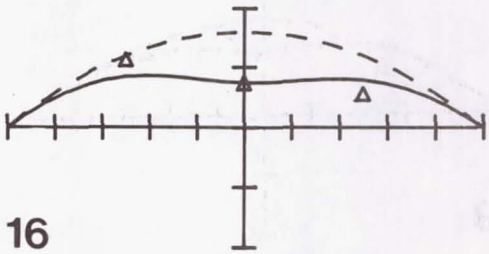

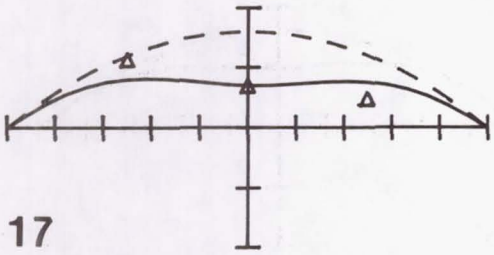

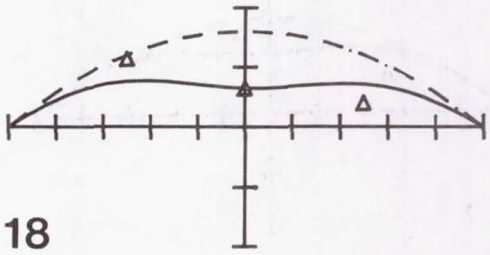

FIG. D3 (CONT.)

right side deflecting more. These deviations in symmetry of the spatial shape are felt to be due directly to initial imperfection of fig. D1.

Even though the work presented in this appendix is only for one specific case, in all likelihood some form of geometric imperfection is present in each of the other test cases as well. The results shown here show that the geometric imperfection found was of the appropriate form to cause an imperfect response and that by taking the initial imperfect configuration into account, the predicted response more closely models the panel behavior.

Appendix E

EFFECT OF INITIAL STIFFNESS ON PANEL BEHAVIOR

In Chapter 5 it was noted that the initial stiffness, i.e., the initial slope of the load-displacement relation, predicted by the theory and the observed initial stiffness did not correlate well. Perhaps some of the discrepancy between the theory and experiment was due to this initial slope difference. Here the effect of the initial stiffness on the overall response is explored with the expectation that, by correctly modeling the linear behavior, the nonlinear behavior can be closely modeled. The initial panel stiffness may be determined by examining the linear response of the panel. In order to determine this stiffness, the theorems of Castigliano are used for the no-load offset case. A full investigation of this is found in [11].

The complimentary strain energy for the panel is,

$$V = \frac{L_x}{2} \int_{-\beta}^{\beta} \left[\frac{M_\theta^2}{D_{22}} + \frac{N_\theta^2}{A_{22}}\right] R \, d\theta. \tag{E1}$$

For a shallow panel the statically admissible forces, found from a free body diagram, are

$$N_\theta = -T \tag{E2}$$

$$M_\theta = R\left(\frac{\theta^2}{2} - \frac{\beta^2}{2}\right)T + R\left(\frac{\beta}{2} - \mathrm{sgn}(\theta)\,\frac{\theta}{2}\right)P \ , \tag{E3}$$

where T is the horizontal support reaction. Substituting these forces into eq. E1 yields

$$V = \frac{R\beta}{P_{22}} [C_T T^2 - C_{TP} TP + C_P P^2] \tag{E4}$$

in which

$$C_T = \frac{D_{22}}{A_{22}} + \frac{2R^2\beta^4}{15} \tag{E5}$$

$$C_{TP} = \frac{5R^2\beta^3}{24} \tag{E6}$$

$$C_P = \frac{R^2\beta^2}{12} . \tag{E7}$$

Applying Castigliano's second theorem to the complimentary strain energy determines the horizontal reaction in terms of the applied load. Then, by applying Castigliano's first theorem to the complimentary strain energy an expression for the initial stiffness is obtained. The initial stiffness is,

$$K = \frac{D_{22}}{R\beta} \frac{2C_T}{4C_T C_P - C_{TP}^2} . \tag{E8}$$

Substituting for the constants C_T, C_{TP}, and C_P the stiffness is rewritten as,

$$K = \frac{\left(\frac{16D_{22}}{S^3}\right)}{\frac{1}{3} - \frac{375}{576}\left(\frac{\lambda^4}{15+2\lambda^4}\right)} , \tag{E9}$$

where use was made of the relationships,

$$S = 2R\beta \tag{E10}$$

$$\lambda^4 = \frac{A_{22}R^2\beta^4}{D_{22}} . \tag{E11}$$

From eq. E9 it is seen that the geometric and material properties of the panel govern the initial response. In order to model the nonlinear response accurately it seems that the predicted linear response should match the observed response. This may be accomplished by 'juggling' the panel parameters in the theoretical formulation until the predicted response matches that of the observed. Table E1 shows the effect of changing the panel parameters on the initial stiffness of the panel. Each column shows the effect of a percentage decrease of the parameters. The initial parameters used are those of test case 1 from Chapter 5.

Upon examining the predicted and observed initial stiffnesses it is seen that the parameters must be changed substantially to match the stiffness. By changing the panel parameters so dramatically, the predicted character of the nonlinear response is changed considerably. This is shown in fig. E1. In this figure, the initial stiffness in the analysis is adjusted, through λ, to match the observed initial stiffness. It is seen that although the initial portions of the load-displacement and load-thrust agree, the overall comparison is very poor. Thus it seems inaccuracies in initial stiffness could not be responsible for the differences between experiment and theory observed in this study. Also, since small inaccuracies, say 5%, in the panels geometric and material properties have such a small impact on the

Table E1

Effect of Panel Parameters on Initial Stiffness

	K/K_o		
	1%	5%	10%
R	1.008	1.037	1.076
D_{22}	.994	.968	.935
A_{22}	.997	.981	.961
S	1.015	1.077	1.152

$K_o = K(R_o, D_{22_o}, A_{22_o}, S_o)$

$R_o = 56.34$ in.

$D_{22_o} = 616.2$ lb-in.

$A_{22_o} = 7.8194 \times 10^5$ lb/in.

$S_o = 12.0$ in.

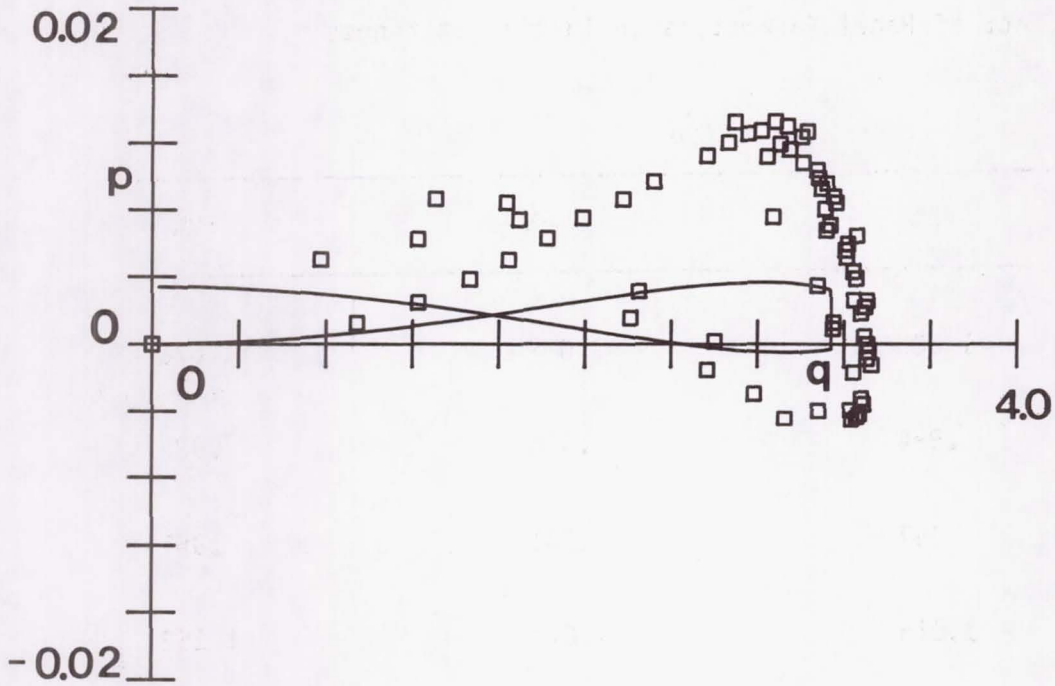

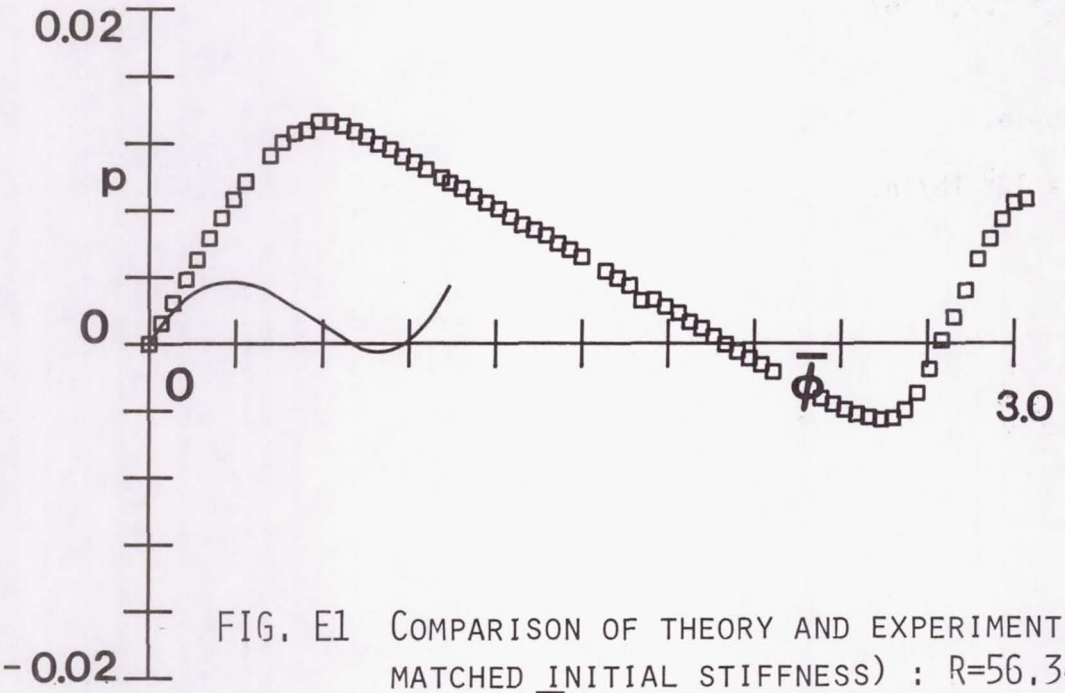

FIG. E1 COMPARISON OF THEORY AND EXPERIMENT (WITH MATCHED INITIAL STIFFNESS) : R=56.34, S=12.0, $\bar{\Gamma}$ =0.0, $[(90/0)_4]_S$

initial stiffness, it seems unlikely that poor measurements of the panel's geometric and material properties would be responsible for differences between observed and predicted panel response.

☆U.S. GOVERNMENT PRINTING OFFICE:1991 -527-064/26018

NASA
National Aeronautics and Space Administration

Report Documentation Page

1. Report No.	2. Government Accession No.	3. Recipient's Catalog No.
NASA CR-4355		

4. Title and Subtitle	5. Report Date
Large Deformation Behavior of Long Shallow Cylindrical Composite Panels	April 1991
	6. Performing Organization Code
7. Author(s)	8. Performing Organization Report No.
Douglas M. Carper, Michael W. Hyer, and Eric R. Johnson	VPI-E-83-37
	10. Work Unit No.
	505-63-50-09
9. Performing Organization Name and Address	11. Contract or Grant No.
Virginia Polytechnic Institute & State Univ. Engineering Science and Mechanics Dept. Blacksburg, VA 24061-4899	NCC1-15
	13. Type of Report and Period Covered
12. Sponsoring Agency Name and Address	Contractor Report 9/1/82 - 8/31/83
NASA Langley Research Center Hampton, VA 23665-5225	14. Sponsoring Agency Code

15. Supplementary Notes

Langley Technical Monitor: Huey D. Carden

Interim Report 36

16. Abstract

An exact solution is presented for the large deformation response of a simply supported orthotropic cylindrical panel subjected to a uniform line load along a cylinder generator. The cross section of the cylinder is circular and deformations up to the fully snapped through position are investigated. The orthotropic axes are parallel to the generator and circumferential directions. The governing equations are derived using laminated plate theory, nonlinear strain-displacement relations, and applying variational principles. The response is investigated for the case of a panel loaded exactly at midspan and for a panel with the load offset from midspan. The mathematical formulation is one-dimensional in the circumferential coordinate. Solutions are obtained in closed-form. An experimental apparatus was designed to load the panels. Experimental results of displacement controlled tests performed on graphite-epoxy curved panels are compared with analytic predictions.

17. Key Words (Suggested by Author(s))	18. Distribution Statement
fiber-reinforced composite laminates composite panels structural stability curved laminates cylindrical composite shells	Unclassified - unlimited Subject category: 39

19. Security Classif. (of this report)	20. Security Classif. (of this page)	21. No. of pages	22. Price
Unclassified	Unclassified	172	A08

NASA FORM 1626 OCT 86

For sale by the National Technical Information Service, Springfield, Virginia 22161-2171